SRI INTERNATIONAL MENLO PARK CA
IN SITU CONSTITUTIVE RELATIONS OF SOILS AND ROCKS. SPHERICAL FI-ETC(U)
APR 77 J T ROSENBERG, P S DE CARLI
DNA001-76-C-0113
NL AD-A063 565 UNCLASSIFIED O63565 111 C



IN SITU CONSTITUTIVE RELATIONS
OF SOILS AND ROCKS

Spherical Field Tests and LASS Results for Pre-Dice
Throw II Materials, LASS Error Propagation Analyses

SRI International

333 Ravenswood Avenue Menlo Park, California 94025

**April 1977** 

Final Repo

Final Report for Period 8 October 1975—31 December 1976

CONTRACT No. DNA 001-76-C-0113

APPROVED FOR PUBLIC RELEASE; DISTRIBUTION UNLIMITED.



THIS WORK SPONSORED BY THE DEFENSE NUCLEAR AGENCY UNDER RDT&E RMSS CODE B344076464 Y99QAXSB04794 H2590D.

Prepared for

Director

DEFENSE NUCLEAR AGENCY

Washington, D. C. 20305

78 11 24 082

Destroy this report when it is no longer needed. Do not return to sender.

PLEASE NOTIFY THE DEFENSE NUCLEAR AGENCY, ATTN: TISI, WASHINGTON, D.C. 20305, IF YOUR ADDRESS IS INCORRECT, IF YOU WISH TO BE DELETED FROM THE DISTRIBUTION LIST, OR IF THE ADDRESSEE IS NO LONGER EMPLOYED BY YOUR ORGANIZATION.

SECURITY CLASSIFICATION OF THIS PAGE (When Data Entered)

	REPORT DOCUMENTATION PAGE	READ INSTRUCTIONS BEFORE COMPLETING FORM
	DNA 4379F	3. RECIPIENT'S CATALOG NUMBER
6	IN SITU CONSTITUTIVE RELATIONS OF SOILS AND ROCKS Sperical Field Tests and LASS Results for Pre-	8 Oct 75—31 Dec 76
	Dice Throw II Materials, LASS Error Propagation Analyses	SRI Project PYU-4663  B. CONTRACT OR GRANT NUMBER(s)
10	J. T. Rosenberg (Project Leader) P. S. De Carli D. D. Keough (Supervisor) D. G. Falconer	DNA 001-76-C-0113
	9. PERFORMING ORGANIZATION NAME AND ADDRESS SRI International 333 Ravenswood Avenue Menlo Park, California 94025	10. PROGRAM ELEMENT, PROJECT, TASK NWED Subtask (7) B047 Y99QAXSB047-94
	11. CONTROLLING OFFICE NAME AND ADDRESS Director Defense Nuclear Agency	April 1977
	Washington, D.C. 20305  14. MONITORING AGENCY NAME & ADDRESS(If different from Controlling Office)	178 15. SECURITY CLASS (of this report)
	(12)178p.	UNCLASSIFIED
	7.13	15a. DECLASSIFICATION DOWNGRADING SCHEDULE
	Approved for public release; distribution unlimit  (8) DNA, SBIE (9) 4379F.  17. DISTRIBUTION STATEMENT (of the abstract entered in Block 20, if different from	, AD-E300 100
	This work sponsored by the Defense Nuclear Agency B344076464 Y99QAXSB04794 H2590D.	
	19. KEY WORDS (Continue on reverse side il nacessary and identify by block number) Material Properties Ground Motion Measurements In Situ Tests Ytterbium Stress Gage Mutual Inductance Particle  20. ABSTRACT (Continue on reverse side if necessary and identify by block number)	Spherical Flow Pre-Dice Throw II Site Error Propagation Analysis Digital Data Smoothing
	For several years, SRI has conducted a progra Defense Nuclear Agency (DNA) to measure the dynam situ geologic materials near and above the elasti in this program has been development of the LASS for Stresses and Strains), in which a mathematica analysis is used to calculate dynamic stress-stra measurements of explosive-induced ground motion.	ic mechanical response of in c limit. A major achievement technique (Lagrange Analysis lly complete Lagrange flow
	DD FORM 1473 EDITION OF 1 NOV 65 IS OBSOLETE	

UNCLASSIFIED

SECURITY CLASSIFICATION OF THIS PAGE (When Data Entered)

#### SECURITY CLASSIFICATION OF THIS PAGE(When Data Entered)

#### 20. ABSTRACT (Continued) -

In the present work three tasks were completed: (1) two fields shots were fired to provide data for proof testing the LASS technique; (2) the field test data were reduced using LASS; and (3) LASS was extended and its accuracy and sensitivity to typical errors in field measurements were evaluated.

The two field tests were 116-kg spherical shots fired in a wet clay layer about 3.6 m below the surface at the Pre-Dice Throw II site. Excellent stress and particle velocity records were obtained with peak stress between 0.2 and 1.7 GPa. Previously developed instrumentation methods were improved in the course of these tests.

Plausible stress-strain trajectories were calculated from the field records using LASS. These indicate nearly reversible radial stress-volume strain behavior until release to low stresses, possible bulking at low stresses on release, and about one-third the compressibility observed in laboratory uniaxial strain tests. The calculated principal stress difference amplitude was small, less than the experimental error associated with the calculation. This result was expected because of the high stress level of the tests and the low strength of the site material.

LASS analysis capabilities were extended by the addition of variable window-width, adjustable low-pass digital smoothing procedures for the field records, the derivation of statistical error propagation equations for the stress and strain calculations, and the formulation and reduction to code of a new and more flexible form of LASS called the global Lagrange analysis. Analysis validation calculations performed on constructed problems for which analytic or numerical solutions are available showed that, with a realistic number of gage stations (five) at which perfect stress and particle velocity records are obtained: (1) stress difference calculations are accurate to within 10%, if the peak stresses at the measurement stations are comparable to the stress difference and (2) strain calculations are accurate to within 5%. Sensitivity studies showed that piecewise linear and global forms of LASS remain stable when small amounts of random amplitude or position noise are added to the gage records.

Recommendations for four possible future research activities related to the present results are offered: (1) experiments to improve the reliability of in situ stress measurements in soils at low stresses where soil strength effects presumably preclude the use of the techniques employed in the present effort, (2) the addition of LASS capabilities to CIST, the Air Force Weapons Laboratory standardized cylindrical in situ test, (3) sensitivity studies and error analyses using LASS to support and optimize the design of proposed buried in situ shots to determine material properties, and (4) theoretical studies to evaluate the sensitivity of LASS to deviations from the assumed flow symmetry.

#### SUMMARY

#### BACKGROUND

The overall objectives of this multiyear program have been to develop the LASS\* method for determining in situ mechanical response of geologic materials and to apply it to field data generated at sites of interest to DNA. Previous accomplishments in the program (see Appendix B) include development of the ytterbium stress gage and the mutual inductance particle velocity gage for rock and soil measurements at high amplitudes and loading rates, application of these gages for close-in measurements on events of concern to DNA, and development of LASS. The objectives of the present work were to modify experimental techniques and the Lagrange analysis (LASS) for increased accuracy and to proof test LASS by applying it to data generated in field tests at a site selected jointly by DNA and SRI.

The LASS method consists of applying a mathematical Lagrange flow analysis to in situ measurements of radial stress and radial particle velocity made during explosive-induced spherical or cylindrical site deformation. Results are the stress and strain trajectories defining in situ response to the applied large-amplitude dynamic deformation. A key point is that for flows satisfying the spherical or cylindrical symmetry condition, the analysis in conjunction with the field measurements is mathematically complete. Therefore (1) the LASS results are unique in the sense that no assumptions concerning the constitutive relations of the test material are used in the analysis, and (2) all independent stresses and strains are calculable for particles within the instrumented region of the flow.

Axial stress is not obtained for cylindrical flow because it does not appear in the conservation of radial momentum law for that geometry.



BOES SPECIAL

<sup>\*</sup>Lagrange Analysis for Stress and Strains.

An in situ dynamic loading test known as CIST has been developed by the Air Force Weapons Laboratory. Because it employs a cylindrical loading source, CIST can simultaneously test several strata within a layered site and hence is cost-effective for such a site. However, because CIST data are analyzed by an iterative procedure in which a model is assumed and the free parameters adjusted until satisfactory agreement with displacement-related field measurements is obtained, the resulting material properties are not unique and may be incomplete because of inadequacies in the assumed model. For site regions in which the CIST source generates cylindrical flow, we suggest combining the LASS analysis with CIST field techniques, augmented by stress measurements, to obtain a site characterization method of high accuracy and cost-effectiveness.

#### PROGRESS

Progress in the LASS program during the past year is summarized below under the following three headings:

- Field tests
- LASS analyses of the field tests
- Analysis extensions and validation.

#### Field tests

The field tests consisted of two replicate spherical shots performed in the Queen 15 Area of the White Sands Missile Range (WSMR). The shot sites were within about 200 m of both Pre-Dice Throw II events and CIST 15 (see Figure 1 in text). The test layer was a relatively uniform wet clay stratum between the water table at a depth of about 2.1 m and a more sandy

Cylindrical In Situ Test.

clay layer at about 5.2 m. The HE sources were 116-kg cast TNT spheres. Instrumentation layout and dimensions are shown in Figures 2 through 4.

Two significant instrumentation improvements were incorporated in these tests. First, the mutual inductance particle velocity gage power supplies were modified to permit remote operation. By locating the power supplies near the shot, we significantly reduced noise generation and pickup problems, power losses in the current cable, and cabling costs. Second, electrical cross talk between gages was reduced by modifying locations and orientations of gages and cables and by avoiding ground loops.

The shots yielded a 100% data return consisting of exceptionally high quality stress and particle velocity records. Peak stresses were between 0.25 and 1.7 GPa, and peak particle velocities were between 50 and 175 ms<sup>-1</sup>. The reduced records are shown in Figures 8 through 15.

### LASS Analysis of Field Tests

Stress and strain trajectories for the test layer were calculated from the field data using LASS. The calculated trajectories, shown in Figures 27 through 29 and 37 through 39, are estimated to be accurate to about 20% of their peak values. The agreement between the two tests, as shown in Figure 41, is about 20% based on the average compressibility calculated at 1.05 m, the middle of the measurement range. This is well within both experimental error and the range of variation expected for this geological site. The material response characteristics indicated by the calculated dynamic stress-strain trajectories, including no hysteresis in the load-release cycle and no irreversible crushing, are quite reasonable for wet clay with virtually no unfilled voids. Because of the high stress level of the field tests compared with the stress difference  $\Phi$  supportable by the test layer, the errors accruing in the

 $\Phi$  calculation are greater than  $\Phi$  everywhere but during loading. Therefore, to the precision of these tests,  $\Phi$  may be taken to be zero. Comparison of dynamic loading states measured in the proof tests with laboratory uniaxial strain test data obtained by the U.S. Army Waterways Experiment Station for similar material from the Pre-Dice Throw II site indicates qualitatively similar behavior but about two-thirds less compressibility in the LASS tests (Figure 41). Thus the wet clay layer appears to be sensitive to the differences between laboratory and in situ test conditions.

The proof tests are judged to have been very successful in that they validated the LASS technique and also provided material properties for the Pre-Dice Throw II site. We conclude that LASS is ready for application at appropriate sites of interest to DNA.

## Analysis Extensions and Validation

We made three major extensions to LASS capabilities in the present work. First, digital data smoothing techniques based on modified low-pass filtering concepts were added to maximize uniformity and reproducibility in data reduction. Second, an alternative Lagrange analysis, termed the global form, was formulated. This form makes more nearly optimal use of the field data, is more convenient for error propagation analyses, provides built-in data smoothing, and permits enforcement of physical constraints, if desired. Third, we derived expressions for the propagated errors in calculated stresses and strains for each form of the analysis. We used standard statistical methods with first-order mathematical approximations and, when applicable, simplifying assumptions. For the global Lagrange analysis, the derived expressions were reduced to code form.

To validate the analysis we performed calculations with either the piecewise linear or global forms of LASS on an elastic test problem for which we have analytic solutions, on an inelastic test problem that we created last year, and on LASS 1 data. As a result we made two technique mcdifications to the piecewise linear analysis, resulting in significant improvements in the accuracy of calculated strains and stress difference. For the elastic problem with five gage stations, we achieved 10% or better accuracies for all quantities including  $\Phi$  in the center of the measurement interval (Figure 44a). For the more complex inelastic problem, comparable accuracies were obtained for the strains (Figure 45), but the calculated  $\Phi$  histories were noisy, primarily because  $\Phi$  is small compared with the radial stresses in this flow region.

The global analysis was applied to the elastic problem and demonstrated to work properly. It was also applied to the same problem after random noise and gage location errors were added. The solutions were not significantly degraded and were consistent with the error propagation analysis predictions. We also demonstrated that reducing the number of gage stations from five to three approximately doubles the analysis errors. (These results are shown in Figure 46 cases 3 and 4, last two plots.) A crude global analysis of the first proof test provided approximate stress-strain paths and more importantly an estimate of the associated errors resulting from measurement uncertainties (see Figure 47).

We conclude from the validation studies that both forms of the Lagrange analysis are working properly, that we can estimate propagated errors using the global analysis, that strains can be accurately calculated from a realistic number of high quality gage records, and that the stress difference can be accurately calculated for flows in which it is comparable in amplitude to the measured stresses.

### FUTURE WORK

For future work we recommend (1) an experimental program to improve in situ dynamic stress measurement capabilities in the important range

between 10<sup>-3</sup> and 10<sup>-1</sup> GPa where properties are needed and are currently not well understood, (2) the application of LASS analysis techniques to appropriate CISTs, if reliable stress measurements can be made, (3) pretest LASS analysis and error propagation calculations to support the design of in situ tests intended to provide material property results of a specified accuracy, and (4) sensitivity studies to evaluate the magnitude of errors caused by applying LASS methods to data from slightly nonuniform or anisotropic site layers.

#### PREFACE

This work was sponsored by the Defense Nuclear Agency (DNA) under Contract DNA001-76-C-0113 of Program Element NWED62704H, Project Y99QAXS, Task Area B047, Work Unit 94. Captain Jerry R. Stockton served as Contracting Officer's Representative. We thank him for his assistance throughout the program.

We are indebted to personnel from many other agencies who assisted in the LASS field tests. We particularly would like to acknowledge and thank, from DNA Field Command, LCDR J. D. Strode for coordinating the efforts of the many agencies involved, Captain Thomas Edwards for much helpful advice and assistance relating to operations at the Pre-Dice Throw II site, Mr. Noel Gantick for coordinating the electronic arrangements, and LCDR E. William Edgerton, Jr. for general support; from the Air Force Weapons Laboratory, Mr. Laurence S. Melzer for much helpful advice and for coordinating the AFWL and LASS field activities throughout the program; from the Civil Engineering Research Facility of the University of New Mexico (CERF), Mr. Kenneth Bell for coordinating the grouting and HE efforts and Mr. Ralph Venegas for emplacing and firing the HE; from the U.S. Army Waterways Experiment Station (WES), many including Mr. Frank Steward for directing the drilling, Mssrs. A. Edward Jackson and John Ehrgott for advice in site selection for the LASS shots, Mr. Ralph Bendenelli for recommendations on grout formulations, and Mr. Joseph Zelasko and Dr. John G. Jackson, Jr. for helpful discussions of the proof test results; and from the White Sands Missile Range, the personnel including cable layers, crane operators, fuel service, equipment repair, and others who performed their jobs well and with due regard for the safety of all.

Finally, we gratefully acknowledge and thank the members of the SRI staff who provided extensive assistance throughout the course of the program. We especially thank Mr. Lee Hall for handling the electronics instrumentation including construction of the new particle velocity gage power supplies, Mrs. Bonita Lew for data reduction, Mr. James Yost for gage element etching, Mr. Albert Bartlett for gage construction, Dr. Michael Cowperthwaite for assistance in evaluating and improving the precision of the linear Lagrange analysis, Drs. Donald Curran and Lynn Seaman for many helpful discussions throughout the work, Mss. Irene Malaspina, Delia Phillips, Joyce Berry, and Kitta Reeds for preparation of the manuscript, and the many others who contributed to this work.

# CONTENTS

SUM	MARY	1
PREI	FACE	7
LIST	OF ILLUSTRATIONS	11
LIST	r of tables	14
1.	INTRODUCTION	15
	Problem	15
	Approach	17
	Previous Results	21
	Report Organization	22
2.	FIELD TESTS	23
	General Requirements for LASS Field Tests	23
	Field Test Description	24
	Site Description	24
	Experimental Configuration	25
	Determination of Lagrange Gage Position	31
	Instrumentation	34
	Instrumentation Improvements for LASS Experiments	38
	Field Test Data and Discussion	42
3.	LASS ANALYSIS OF FIELD TESTS	55
	Smoothing	55
	LASS 1 Analysis and Results	55
	LASS 2 Analysis and Results	74
	Discussion	79
	Deformation	79
	Material Response	88
	Errors	91
	Conclusions	94

4.	ANAL	YSIS DEVELOPMENT	97
	Exte	nsions	97
		Digital Smoothing of Field Data	97
			98
			02
	Vali		02
			.03
		Piecewise Linear LASS, Inelastic Test Problem 1	08
		Global LASS, Elastic Test Problem	.08
			13
			14
	Conc		17
5.	CONC	LUSIONS AND RECOMMENDATIONS	18
REF	ERENC	ES	21
APP	END I X	ES	
	A	LAGRANGE ANALYSIS FOR SPHERICAL FLOWS	-1
	В	BACKGROUND	-1
	C	DIGITAL SMOOTHING OF FIELD DATA	-1
	D	STRESS-STRAIN ERROR ASSIGNMENTS FOR FINITE-DIFFERENCE	
		LAGRANGE ANALYSIS	-1
	E	STRESS-STRAIN ERROR ASSIGNMENTS FOR GLOBAL LAGRANGE	
		ANALYSIS E	-1
	F	STRESS-STRAIN ERROR ASSIGNMENTS FOR PIECEWISE-LINEAR	
		LAGRANGE ANALYSIS	-1

## ILLUSTRATIONS

Figure		Page
1	Map of Test Area	26
2	Elevation View of Experimental Layout, LASS 1 and 2 (not to scale)	27
3	Plan View of Gage Layout for LASS 1	30
4	Plan View of Gage Layout for LASS 2	32
5	LASS Gages	36
6	LASS 1 Stress Gage 1 Record	39
7	LASS 1 Particle Velocity Gage Record	41
8	Radial Stress Histories, LASS 1	43
9	Particle Velocity Histories, LASS 1	44
10	Radial Stress Histories, LASS 2	45
11	Particle Velocity Histories, LASS 2	46
12	Individual Stress Gage Records, LASS 1	47-48
13	Individual Particle Velocity Gage Records, LASS 1	49-50
14	Individual Stress Gage Records, LASS 2	51-52
15	Individual Particle Velocity Gage Records, LASS 2	53-54
16	Smoothed Radial Stress Histories, LASS 1	56
17	Smoothed Particle Velocity Histories, LASS 1	57
18	Smoothed Radial Stress Histories, LASS 2	58
19	Smoothed Particle Velocity Histories, LASS 2	59
20	Features Used to Characterize LASS 1 Stress Records for Piecewise Linear Lagrange Analysis	61
21	Time Link Lines for LASS 1 Stress Gage Flow Surface .	63
22	Amplitude Link Lines for LASS 1 Stress Gage Flow Surface	64

Figure		Page
23	Features Used to Characterize LASS 1 Particle Velocity Records for Piecewise Linear Lagrange Analysis	66
24	Amplitude Link Lines for LASS 1 Particle Velocity Gage Flow Surface	68
25	Piecewise Linear Gage Flow Surface Representations of LASS 1 Stress Histories at Lagrange Coordinates 0.6, 0.8, 1.05, 1.3, and 1.6 m	69
26	Piecewise Linear Gage Flow Surface Representation of LASS 1 Particle Velocity Histories at Lagrange Coordinates 0.6, 0.8, 1.05, 1.3, and 1.6 m	70
27	Radial Stress Versus Volume Strain, LASS 1, at Lagrange Coordinates 0.6, 0.8, 1.05, 1.3, and 1.6 m .	71
28	Radial Strain Versus Tangential Strain, Volume Strain Versus Principal Strain Difference, and Radial Stress Versus Radial Strain, LASS 1, at Lagrange Coordinates 0.6, 0.8, 1.05, 1.3, and 1.6 m	72
29	Radial Strain, Tangential Strain, Volume Strain, and Stress Difference Versus Relative Time at Lagrange Coordinate h=1.05 m, LASS 1	73
30	Features Used to Characterize LASS 2 Stress Records for Piecewise Linear Lagrange Analysis	75
31	Time Link Lines for LASS 2 Stress Gage Flow Surface .	77
32	Amplitude Link Lines for LASS 2 Stress Gage Flow Surface	78
33	Features Used to Characterize LASS 2 Particle Velocity Records for Piecewise Linear Lagrange Analysis	80
34	Amplitude Link Lines for LASS 2 Particle Velocity Gage Flow Surface	82
35	Piecewise Linear Gage Flow Surface Representations of LASS 2 Stress Histories at Lagrange Coordinates 0.8, 0.9, 1.05, 1.2, and 1.3 m	83
36	Piecewise Linear Gage Flow Surface Representation of LASS 2 Particle Velocity Histories at Lagrange Coordinates 0.8, 0.9, 1.05, 1.2, and 1.3 m	84
37	Radial Stress Versus Volume Strain, LASS 2, at	85

Figure		Page
38	Radial Strain Versus Tangential Strain, Volume Strain Versus Principal Strain Difference, and Radial Stress Versus Radial Strain, LASS 2, at Lagrange Coordinates 0.8, 0.9, 1.05, 1.2, and 1.3 m	86
39	Radial Strain, Tangential Strain, Volume Strain, and Stress Difference Versus Relative Time at Lagrange Coordinate h = 1.05 m, LASS 2	87
40	Radial Stress Versus Volume Strain, LASS 1, From Figure 27 with Equilibrium Compression Curve Added	89
41	Stress Versus Volume Strain for Pre-Dice Throw II Wet Clay From Three Different Tests: LASS, CIST, and UX.	95
42	Analytic Stress and Particle Velocity Profiles, Elastic Test Problem	104
43	Finite Difference LASS Calculations (Solid Curves) Compared with the Analytic Profiles (Dashed Curves) at Lagrange Coordinate h = 6, Elastic Test Problem	105
44	Piecewise Linear LASS Calculations (Solid Curves) Compared with Analytic Solutions (Dashed Curves) at Lagrange coordinate h = 6, Elastic Test Problem	107
45	Piecewise Linear LASS Results for Complex Flow Problem Generated by PUFF Code	109
46	Global LASS Calculations (Solid Curves) Compared with Analytic Solutions (Dashed Curves) at Lagrange Coordinate h = 6, Elastic Test Problem	0-111
47	Preliminary Global Analysis and Error Estimates Based on LASS 1 Field Test Data	115
48	Finite Difference LASS Calculations of Elastic Test Problem with Noise and of LASS 1 Field Data for Comparison with Piecewise Linear and Global Calculations	116
A-1	Gage Flow Surface	A-5
A-2	Piecewise Linear Representation of Gage Record	A-5
A-3	Amplitude-h Link Line for Peak Stress '	A-7
A-4	Gage Flow Surface Representation	A-8
D-1	Constant-Feature Path	D-4

# TABLES

Table		Page
1	Range Corrections for LASS 1 and LASS 2	35
2	LASS 1 Stress Gage Flow Surface Link Lines	62
3	LASS 1 Particle Velocity Gage Flow Surface Link Lines .	67
4	LASS 2 Stress Gage Flow Surface Link Lines	76
5	LASS 2 Particle Velocity Gage Flow Surface Link Lines .	81

#### 1. INTRODUCTION

For several years the Defense Nuclear Agency (DNA) has conducted a program at SRI to determine dynamic in situ constitutive properties of soils and rocks at sites of interest. The program has had three major emphases:

- Development of ground motion instrumentation in the stress range from 0.1 to 3.0 GPa.
- Development of a one-dimensional divergent flow Lagrange analysis.
- Field testing.

The program has produced a new site characterization method that draws on results from each of the above areas. In this technique a Lagrange analysis is applied to field measurements of site material motion induced by explosive loading to obtain dynamic stress-strain trajectories for the in situ material. We refer to the reduction of appropriate field data by Lagrange analysis as the LASS technique (Lagrange analysis for stresses and strains). This report describes new material properties results obtained with LASS and recent developments of LASS capabilities.

### PROBLEM

Determination of the vulnerability of structures to near surface detonations involves calculating the airblast, ground shock, cratering, and soil-structure interactions induced by the event. However, for partially contained detonations and for complicated site geologies and materials, code predictions of these phenomena often do not agree with field measurements. The discrepancies are usually attributed to

inadequacies in the material models or the material properties used to represent the site material in the calculations. Properties of the yield surface are particularly uncertain.

For HE events the dynamic mechanical response for in situ material, along a variety of loading paths in stress space, for stresses from under a MPa to well over a GPa, and at strain rates from less than 10 2 to greater than  $10^4 \text{ s}^{-1}$  must be correctly specified by the material model if soil response is to be satisfactorily calculated. Traditionally, a fairly extensive data base for constructing these models would contain information on generic material properties from previous studies on presumably similar materials, the results of various mechanical and physical tests performed in the laboratory on cores removed from the test site, and some on-site characterization data such as the results of seismic and geologic surveys. Unfortunately, since such data are not always obtained under conditions matching those existing in the event to be calculated, a model constructed from them could possibly be seriously in error when applied to the event. Specific factors that are different from the event conditions in one or more of the data base sources listed above, and that are capable of significantly affecting specimen material response, include (1) in situ environmental conditions such as specimen moisture content and preexisting lithostatic stresses, (2) specimen crack and defect content calculated over volumes scaled to the predominant wavelengths expected in the event being calculated, and (3) loading conditions including amplitude, rate, and stress path.

Various computational and experimental approaches have been pursued,

(a) to determine the relative importance of the present limitations in
the material properties data base, (b) to provide "correction factors"
that account for phenomenology not adequatly addressed to date (e.g.,
rate effects, anisotropy, etc.) and (c) to develop testing equipment
and techniques to address these shortcomings. The approaches include

code studies of parameter sensitivity; laboratory rate dependence and prestress tests, usually with small specimens; in situ quasi-static flat jack tests; the use of larger, faster laboratory mechanical testing devices; and, recently, iterative model adjustments based on field measurements (CIST). In spite of such efforts, the constitutive relations for dynamically loaded in situ material remain a major uncertainty in ground motion, cratering, soil-structure interaction, and vulnerability calculations.

Ideally, what is needed is site material response information obtained under field event conditions. In principle, tests should be performed with representative specimens of site material comparable in size to the wavelengths expected in the actual event, in the in situ environment, at the loading rates and amplitudes of interest in the event, and along several different stress paths.\*

## APPROACH

The method SRI has developed for determining site constitutive properties from which to construct material models is called the LASS technique, after the Lagrange analysis used to reduce the data. In this technique, a buried high explosive (HE) charge, usually 100 kg or larger, is used to induce either spherical or cylindrical flow over several cubic meters or more of the in situ site material of interest. Radial stress and radial particle velocity histories along several particle paths in the induced flow are measured with appropriate ground motion gages,

Since no single experiment is capable of providing all of this information for completely characterizing a given site, it is essential that the various available techniques be correlated and integrated to produce an optimal, cost-effective, site characterization. Field experiments comprise a key element in this approach.

and the field measurements are used in a Lagrange flow analysis to calculate the principal stress and strain histories of particles at various locations in the flow. The resulting stress and strain histories are an important addition to the data base for material modeling for buried events because they apply under conditions close to those existing in the events to be calculated, they are readily related to model parameters, and they can be used to modify or validate previously constructed models.

The Lagrange analysis has been described in detail in previous reports 1-3 and is summarized in Appendix A. Basically it is a numerical analysis in which field measurements of radial stress and radial particle velocity along several particle paths are used to estimate partial derivatives appearing in the conservation of mass and momentum laws for one-dimensional divergent flows (spherical or cylindrical). The conservation laws can then be solved for the material density and the difficult-to-measure tangential principal stress as functions of particle coordinate and time. The principal engineering strains as functions of particle position and time are evaluated from their definitional equations and the measurements of radial particle velocity. Since the analysis determines all the principal stresses and strains as function of Lagrange coordinate and time, any desired stress-strain cross-plot for a given particle within the instrumented region of the flow is available by eliminating the time parameter at that Lagrange coordinate.

The LASS technique is well suited to providing input for the material models of interest to DNA because it is applied to data obtained in moderately large HE field tests and because it uses a mathematically complete analysis to reduce the data. The advantages of obtaining data in a

<sup>\*</sup>In cylindrical flow the axial stress is not determined since it does not appear in the conservation equations.

large-scale HE field test are that the results apply to in situ material, and that the specimen volumes are great enough to statistically average the effects of many in situ flaws, defects, and inclusions that would not be present in the smaller laboratory specimens. The loading rates are greater than those usually achieved in the laboratory and provide an upper bound for (or in some cases are comparable to) those occurring in DNA problems. These advantages also apply, of course, to any similar large amplitude dynamic in situ test, such as CIST, discussed later in this section.

Since the Lagrange analysis is mathematically complete, it has several advantages over in situ material properties determination that do not have this property. The results are unique in the sense that no assumptions concerning the constitutive relations of the test material, and no iterative procedures, are used in data reduction. Also, all the independent stresses and strains, including much-needed shear information, can be calculated for particles within the instrumented region of the flow. Furthermore, LASS output is stress and strain trajectories—a convenient form for constructing material models; error estimates to establish confidence limits for the trajectories can be made; and the technique is applicable in any stress range or material response regime as long as the flow is one-dimensional and the required measurements are obtained.

The limitations of LASS for site modeling are of two types: field data limitations and analysis limitations. Field data obtained by any means are usually noisier and less reliable than laboratory data both because of the uncontrolled environment in which the measurements are made and because of the likelihood of undetected natural inhomogeneities

Except for axial stress in cylindrical flows.

within the test material. In addition, emplacement of the source and/or instrumentation may alter the site properties both in the immediate vicinity of the transducers and throughout the test region.

The LASS analysis limitations are that (1) it is strictly valid only within homogeneous isotropic site regions that support one-dimensional flows, and (2) the accuracy of the results depends on both the quality of the field data and the number of stations at which the data are obtained. Neither limitation is considered severe. The homogeneity and isotropy constraints are consistent with conditions observed at many sites and assumed in many of the models and calculations that LASS is intended to support. Accuracy of any test is limited by the quality and quantity of the measurements; however, the present work demonstrates that LASS produces satisfactory precision with realistic numbers of field quality records and is not unduly sensitive to the uncertainties included in field measurements.

The Air Force Weapons Laboratory (AFWL) has developed a cylindrical in situ test, CIST, which has provided important ground motion information at a number of sites of interest to DNA. In CIST a relatively standardized cylindrical HE source is used to load the site, and the resulting horizontal, and sometimes vertical, acceleration histories are measured in identified site layers at various ranges. Cavity pressures are also measured and usually permit an idealized representation of the source in that test. Attempts at soil stress measurement have so far not been successful because of experimental difficulties, such as bridging around the gage, encountered at the low stress levels (usually less than 50 MPa) examined in a typical CIST.

Material properties are calculated from CIST data by an iterative process in which a model is assumed and the parameters are adjusted until the best agreement with the measured particle velocity (integrated

acceleration) histories is obtained. Although this analysis does not produce unique results, it is necessary because the flow is not fully specified by velocity histories alone. If stress histories were available, much stronger constraints would be put on the model. In some cases, such as for cylindrical flows, the LASS analysis could be used. The results would provide a basis for constructing the models before any iterations and would significantly increase the accuracy and reliability of the resulting constitutive relations.

Because of its cylindrical geometry, CIST is a cost effective means for examining site properties as a function of depth. It is also well suited to layered sites. If the layers are homogeneous and isotropic so the flow is strictly cylindrical within layers until communication from the boundaries occurs, the LASS analysis may be used for data reduction if stress measurements are obtained. After layer interactions, or for transversely isotropic layers, CIST still provides information for evaluating the parameters in appropriate models; however, the uniqueness problem, already significant in homogeneous isotropic noninteracting layers, becomes severe. It probably would not be feasible to use CIST to examine or model higher degrees of site anisotropy; nor are such levels of complexity now likely to be retained in either material models or DNA ground motion calculations. For appropriate sites we have recommended that the LASS analysis be used in conjunction with CIST's, if the experimental problems in measuring low stresses in soils and rocks are solved, to obtain a site characterization method of high accuracy and cost effectiveness.

### PREVIOUS RESULTS

Previous work in the SRI in situ properties program and related areas has been described in a series of DNA reports 1-3,5-14 summarized in Appendix B. Major milestones were the proposal of the LASS concept

and the demonstration of its feasibility, the development of ytterbium stress gages and mutual inductance particle velocity gages to the status of working field gages, 2,5-7 the subsequent use of ytterbium stress gages to make ground motion measurements for DNA in a number of nuclear and HE events, 8,10-14 the development of the piecewise linear LASS analysis (see Appendix A) to code form in which it can calculate stress-strain trajectories for complex time-dependent flows, 1-3,5-7 demonstration that the accuracy of the numerical LASS methods for calculating strains when applied to perfect records from 5 to 8 gage stations is better than 10%, and the first field application of LASS in the WES CENSE II series.

#### REPORT ORGANIZATION

Section 2 describes the layout, instrumentation, and data from this year's field tests. Section 3 contains the LASS analysis of the field tests, a discussion of the results, and a comparison with other data. Section 4 describes analysis developments including new additions, validation studies, and conclusions. Section 5 summarizes the current status of the LASS technique and recommends future material modeling efforts building on the present work.

Appendix A describes the LASS analysis. Appendix B summarizes and references previous results in the SRI material properties program. Appendix C describes the methods for digital smoothing of field data, and Appendixes D through F present error propagation analyses.

### 2. FIELD TESTS

Two spherical field tests, LASS 1 and LASS 2, were performed in the Queen 15 area of White Sands Missile Range (WSMR) near the sites of the Pre-Dice Throw II events. The purpose of the experiments was to provide data for proof testing the LASS technique at a site of interest to DNA. This section describes the experiments and the resulting data.

We encountered the usual problems of field work, including drill rig breakdowns, generator failures, instrumentation malfunctions, site lockouts, and stormy weather. However, thanks to the excellent support provided by WES, CERF, WSMR, and DNAFC, all phases of the field work were completed on schedule and in accordance with our experimental requirements.

The experiments were successful. All the ytterbium stress gages and mutual inductance particle velocity gages worked well; laboratory-quality records were obtained from all data channels.

## GENERAL REQUIREMENTS FOR LASS FIELD TESTS

The objective of a LASS experiment is to determine the stress-strain response of in situ material under conditions of dynamic deformation. Significant features of the LASS technique are that the in situ measurements are made in relatively undisturbed material and that the loading rates of the experiment are at least equal to the loading rates of interest in stress wave hazard calculations. The LASS technique is a general one, adaptable to cylindrical flow, spherical flow, or plane flow. Both the experimental data requirements and the details of the analysis are specific

to the flow geometry chosen; it is crucial to the validity of the analysis that the actual experimental geometry match the geometry assumed for the analysis.

An ideal spherical LASS experiment would comprise a spherical explosive charge embedded in an isotropic medium and surrounded by radial stress and particle velocity gages located at various distances from the charge center. The gages are Lagrangian; they move with the flow along particle paths, and ideally, they do not perturb the flow. Since knowledge of both independent flow variables (radial stress and radial particle velocity) is necessary for a LASS analysis, the range of Lagrange coordinates (initial distance from the charge center) spanned should be the same for both gage types. The measured stress and particle velocity histories permit unambiguous calculation of material properties over the range of deformations and deformation rates spanned by the gages. It is important that the gages survive and record accurately during stress wave decay, since the analysis is valid for determining unloading as well as loading response of the material.

## FIELD TEST DESCRIPTION

#### Site Description

The Queen 15 site of WSMR was of interest to DNA because of previous work there including the two large Pre-Dice Throw II events and a CIST experiment. Furthermore, extensive field and laboratory studies of the properties of the site had been performed by WES in support of the Pre-Dice Throw II events. These studies had indicated the presence of a uniform, fully saturated, clay layer bounded by the water table at a depth of about 2 m and a sandy layer below at about 5 m. This layer appeared ideally suited to a properly designed spherical LASS experiment.

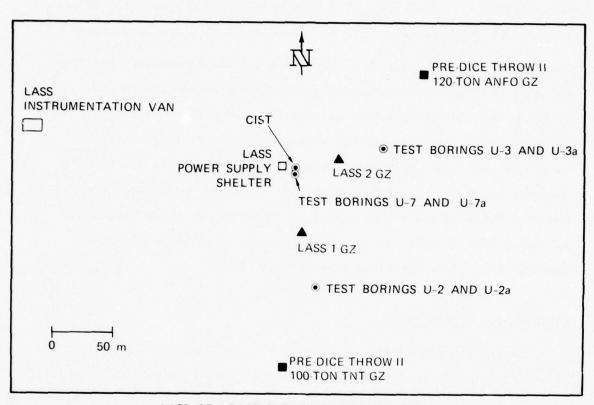
Figure 1, a map of the test area, shows the relationship of the two LASS experiments to the CIST and Pre-Dice Throw II events. The LASS sites may be considered as previously undisturbed; peak pressures from either of the Pre-Dice Throw II events or from the CIST experiment had attenuated to less than a few bars at the LASS ground zeros (GZs). The LASS GZs were selected by DNA Field Command with SRI concurrence.

A basic assumption made in the design of the experiments was that the soil profiles at the LASS GZs would closely correspond to the profiles observed at test borings U-3, U-7, and U-2 (see Figure 1). To check on the validity of this assumption, we were alert for any anomalies that might be observable during drilling of the charge holes and gage holes for the LASS experiments. Over the depth range of concern, 2.4 m to 4.3 m, the clay layer appeared to be uniform, fully saturated, and of very low strength. Results of the WES subsurface exploration studies are given in reference 15.

## Experimental Configuration

The general experimental layout of both LASS experiments is illustrated in the elevation view of Figure 2. The explosive source, a center-initiated 112-kg (256-pound) TNT sphere, was emplaced at a depth (ground level to center of sphere) of 3.66 m (12 feet). Ytterbium stress gages were grouted into vertical drill holes at various distances from the charge center. Mutual inductance particle velocity gages were grouted into 30-degree (with respect to the horizontal) drill holes radial to the charge center.

For practical reasons, various compromises had to be made with the "ideal experiment" described previously. The isotropy of the medium is perturbed by grout in the gage holes, by the presence of the cylindrical grouted-in aluminum charge hole liner, and by the water-saturated sand surrounding the charge.



# LASS GZ LOCATIONS, WSMR COORDINATES

LASS 1 GZ: X - 490,549.78

Y - 541,370.67

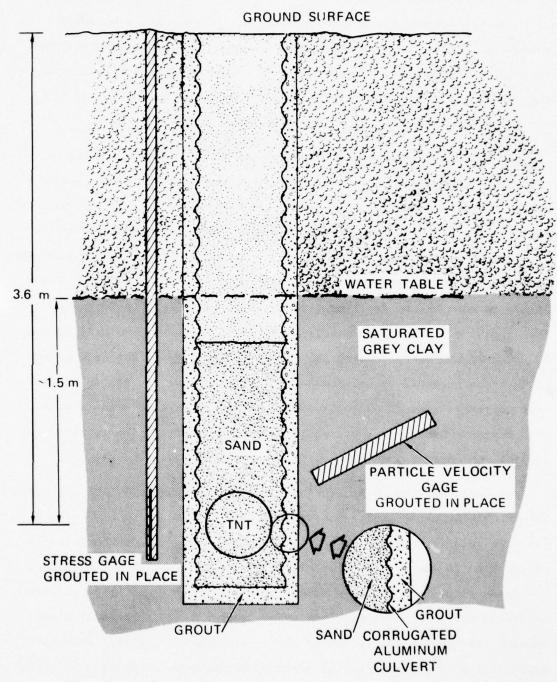
E - 4,199.87

LASS 2 GZ: X - 490,627.78

Y - 541,591.89 E - 4,201.24

MA-4663-9

FIGURE 1 MAP OF TEST AREA



MA-4663-10

FIGURE 2 ELEVATION VIEW OF EXPERIMENTAL LAYOUT, LASS 1 and 2 (not to scale)

The effect of grout in the gage holes is minimized by choosing a grout that closely matches the medium, by spacing the gage holes to avoid shadowing of any gage by a nearby grout column, and by restricting the range of measurement to stresses well in excess of the grout strength. The grout used, DTE-2 (E), was recommended by Ralph Bendenelli of WES for use in the saturated clay at the Pre-Dice Throw II site.

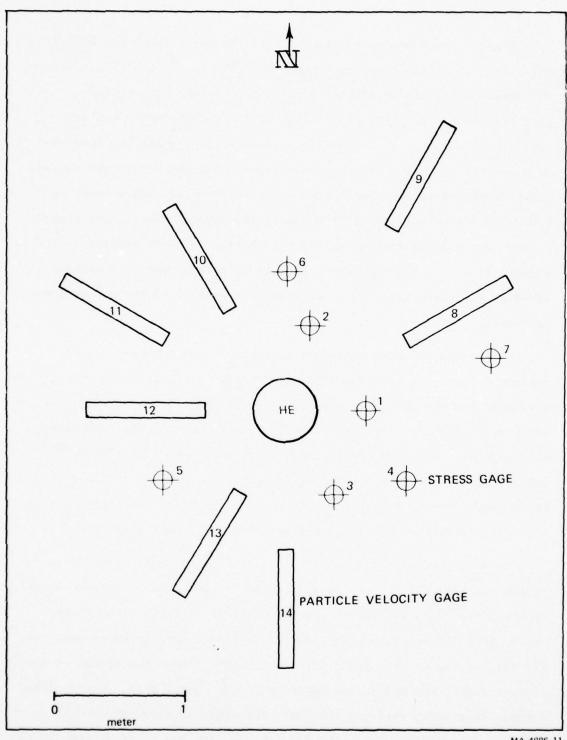
The grouted-in corrugated aluminum charge hole liners and the saturated sand surrounding each charge were required by the logistics of the LASS experiments. To minimize experimental costs, it was necessary to drill the charge holes and the gage holes during the same period of time, about a month before the scheduled execution of the LASS experiments. However, holes drilled in the water-saturated clay layer began to slump almost as soon as the drilling tool was removed. Since emplacement of the explosive charges immediately after drilling would have been unsafe, liners were necessary to keep the charge holes open so that emplacement of each charge could be delayed until the day before the scheduled test. Safe considerations also dictated use of water-saturated sand to stem the charges. Ordinary grouts would not set up sufficiently in 24 hours to stem the charge, and fast-setting grouts become dangerously hot.

It must be noted that spherical flow (for a spherical LASS experiment) is strictly necessary only within the region spanned by the stress and particle velocity gages. Material strength effects due to the presence of the grouted liner are negligible in the high stress close-in region, and water saturated sand is a fairly good shock impedance match to water-saturated clay. By centering the stress gages in the horizontal plane passing through the charge center and by placing the particle velocity gages at the relatively shallow angle of 30 degrees, we believe we avoided the region in which the sphericity of flow was substantially perturbed by the presence of the liner and by the small impedance mismatch between the sand and the clay.

Figure 3 is a schematic plan view of the gage layout for LASS 1. Note that the particle velocity gages actually lie on a conical surface 30 degrees above the horizontal plane of the stress gage centers (see Figure 2). However, Figure 3 shows the true relative radial positions of all gages; the particle velocity gage positions have been rotated into the plane of the stress gages. The gages span the nominal range (radial distance from charge center) from 0.61 m (2.0 feet) to 1.62 m (5.3 feet). Three stress gages, 120 degrees apart, were placed at the same nominal radius of 1.07 m (3.5 feet). Three particle velocity gages, all at the nominal radius of 1.07 m, were placed in a similar 120-degree pattern (rotated 60 degrees with respect to the stress gage pattern).

This redundant gage placement scheme was used because we were concerned about the accuracy with which Lagrangian gage positions (initial distance from the charge center) could be determined under field conditions. Our concern proved to be justified; the saturated clay was so unstable that gage placement and grouting had to be done immediately after removal of the tool from the hole. There was no time to resurvey. Furthermore, even a visual check of gage position and hole straightness was not possible because the holes were over half full of water.

We also encountered problems in accurately emplacing the TNT sphere for LASS 1. The charge floated out of position as we were stemming the hole; we had neglected to consider that the mixture of sand and water could behave as a dense liquid. We used a long stick to push the TNT down to the correct depth, but we could no longer see enough of the charge to tell whether it was centered in the charge hole. Rather than exhume the charge, bail out the hole, and start over, we decided to continue stemming the hole. We did not want to have to delay the firing schedule, and we were certain that it would be simple to determine the true charge center from the redundant 1.07 m particle velocity gage records.



MA-4886-11

FIGURE 3 PLAN VIEW OF GAGE LAYOUT FOR LASS 1.

Particle velocity gages are shown as rectangles, stress gages as circles. Gage locations to scale.

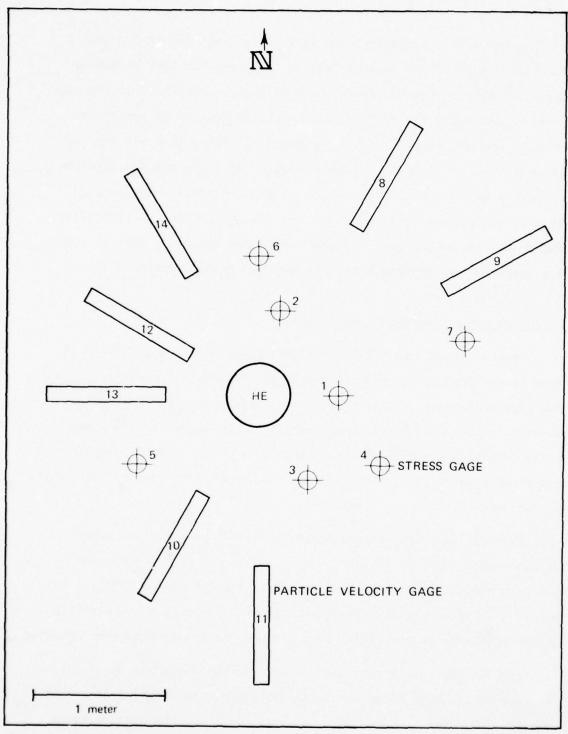
Figure 4 is a schematic plan view of the gage layout for LASS 2. The stress gage layout is identical to that used for LASS 1, but we were forced by circumstances to use a different particle velocity gage layout. The drill rig shifted during drilling of one of the first nominal 30-degree holes and the resultant 25-degree hole was too far off-center to be used for a close-in gage. We therefore modified the layout, dispensing with the 1.07-m redundant particle velocity gages. It was consequently more important to position the charge accurately, and we believe we did so. We then blocked the charge so that it could not float out of position while the hole was being stemmed.

## Determination of Lagrange Gage Positions

Accurate knowledge of Lagrange gage positions (initial distance from charge center) is an important factor in the LASS analysis. Ideally, the gage and charge positions would be determined by post-installation surveys, but, as previously mentioned, this procedure was precluded by field conditions. Therefore, knowledge of gage positions depends on the accuracies of the initial survey, of the drilling of gage holes, and of gage and charge emplacement.

The initial survey of gage hole locations was performed after drilling and lining of the charge holes. The center of each liner was determined at the desired charge emplacement depth of 3.66 m. This point established the desired GZ (the point at surface level directly above the charge center) from which all gage hole locations were measured.

For the vertical stress gage holes, the drill rig was spotted with an accuracy of about 30 mm and initially aligned to within  $\frac{1}{4}$  degree of vertical. However, because of drill rig looseness, the drilled holes could have deviated from vertical by as much as 1 degree. The stress gages were attached to a PVC pipe for installation. A crossbar taped



MA-4886-12

FIGURE 4 PLAN VIEW OF GAGE LAYOUT FOR LASS 2.
Particle velocity gages are shown as rectangles,
stress gages as circles. Gage locations to scale.

to the pipe provided positive control of installation depth. However the position of the gage within the hole could not be controlled, and the actual diameter of the hole at gage depth was not known. Our best estimate is that the uncertainty in stress gage position could have been as large as  $\pm$  60 mm.

The 30-degree angle of the particle velocity gage holes was initially set with an accuracy of 1/2 degree, the radial alignment of the drill in the 30-degree plane was accurate to within  $\frac{1}{4}$  degree, and initial spotting of the drill was accurate to within about 40 mm. PVC pipe handles marked at the correct installation length were used with the particle velocity gages. By measuring the distance from the GZ to the mark on the handle, it was possible to compensate for the drill spotting error. Except for one instance in which a shift of the drill rig resulted in a 5-degree deviation, measurements of the drill stem angle at full drill depth indicated that the 30-degree angle was maintained with an accuracy of about 1 degree. Allowing for possible bending of the poorly supported portion of the drill stem below the water table, we estimate that the uncertainty in particle velocity gage position was no more than about 20 mm.

Because of their greater accuracy, only the particle velocity gage positions were used in constructing a time-of-arrival versus range relation. This relation, together with stress gage time-of-arrival data, was used to obtain more accurate estimates of stress gage ranges.

For LASS 1, the spread in times of arrival for the three particle velocity gages at a nominal range of 1.07 m indicated that the true charge center was displaced from the design center by about 50 mm. Using time-of-arrival data from all seven particle velocity gages, we iteratively adjusted the charge center until the recalculated gage positions fit a smooth time-of-arrival versus range relation.

Time-of-arrival data, nominal gage positions, and corrected gage positions used in subsequent analyses for LASS 1 and LASS 2 are listed in Table 1.

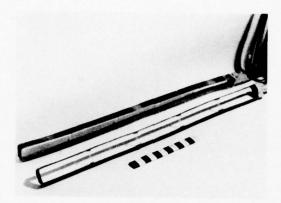
# Instrumentation

The basic transducers used in the LASS experiments were the ytterbium piezoresistive stress gage and the mutual inductance particle velocity gage. Both gage types have been extensively developed and tested in numerous field experiments. 1-3, 5-9, 11-14 Indeed, the design parameters of the LASS experiments were specifically chosen to exploit the stress range (0.05 to 2 GPa) over which both gage types are accurate and have previously exhibited good survival through stress release. The stress gages were of the same designs used in the Pre-Dice Throw II events, 14 Figure 5(b), (c). The particle velocity gages were 1.02 m long, wound with PVC insulated solid AWG 20 copper wire, Figure 5(a). Primary and secondary windings each consisted of ten turns. Series inductances (80  $\mu$ H) were used in the primary circuit; a parallel noninductive 50-ohm resistor was also used in the primary circuit to attenuate the noise pulse that occurs on gage failure.

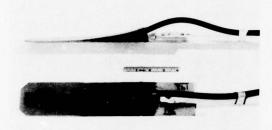
The ytterbium stress gages are powered by the same power supplies used in previous field experiments. The gage and its cable form one leg of a bridge circuit powered by a triggered capacitor discharge. The time constant of the discharge exceeds 100 ms; voltage across the bridge is essentially constant over the few milliseconds spanning gage recording times. The gage changes resistance upon arrival of the stress wave, and the resultant bridge imbalance is recorded by an oscilloscope camera, backed up by a tape recorder. Before the experiment, the system response is calibrated by series insertion of precision resistors spanning the range of expected gage resistance changes. These calibrations are used to convert the observed voltage-time records into relative

 $\begin{tabular}{ll} Table 1 \\ \begin{tabular}{ll} RANGE CORRECTIONS FOR LASS 1 AND LASS 2 \\ \end{tabular}$ 

IASS 1 Stress gages	Gage No.  1 2 3 4 5 6 7	Nominal Range (m)  0.610 0.671 0.732 1.07 1.07 1.07	Time of Arrival (µs) 144 204 189 334 313 343 612	Corrected Range (m)  0.526 0.692 0.655 0.987 0.942 0.999 1.580
LASS 1 Particle velocity gages	$ \begin{cases} 12 \\ 13 \\ 10 \\ 14 \\ 11 \\ 8 \\ 9 \end{cases} $	0.610 0.732 0.884 1.07 1.07 1.07	175 242 290 356 388 404 624	0.610 0.701 0.930 1.02 1.10 1.10
LASS 2 Stress gages	$   \left\{     \begin{array}{c}       1 \\       2 \\       3 \\       4 \\       5 \\       6 \\       7   \end{array} \right. $	0.610 0.671 0.732 1.07 1.07 1.615	150 168 176 308 309 318 572	0.540 0.611 0.631 0.950 0.959 0.976 1.510
LASS 2 Particle velocity gages	$ \begin{cases} 12 \\ 13 \\ 10 \\ 14 \\ 11 \\ 8 \\ 9 \end{cases} $	0.610 0.732 0.884 1.07 1.31 1.49	169 219 267 366 474 596 616	0.610 0.732 0.884 1.07 1.31 1.49



(a) LASS Particle Velocity Gages



(b) LASS Stress Gages  $-6\Omega$ 



(c) LASS Stress Gages  $-25\Omega$  Used only at 1.6 m stations

MP-4663-15

FIGURE 5 LASS GAGES

resistance-time data, with appropriate corrections for cable resistance. Stress-time data, for both loading and unloading, are obtained from the ytterbium calibrations of Ginsberg et al.  $^9$ 

The mutual inductance gages are also powered by capacitor discharge power supplies, as described in a previous report. In the present experiments, the discharge time constant was only about 5 ms, i.e., only an order of magnitude above gage recording time. Consequently, gage currents decayed by about 10% over the times spanned by the particle velocity gage records.

Preshot calibrations of each gage system indicated that the current-versus-time relationship was reproducible to within about 1%. The experimental data are voltage-time histories, recorded by oscilloscope cameras backed up by tape recorders. These voltage histories are converted to particle velocity histories by the following equation:

$$V(t) = \frac{R_T}{R_T + R_C} I(t) \frac{M}{X} u(t)$$

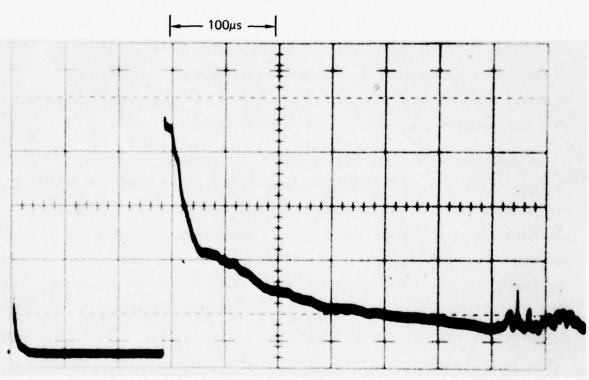
where  $\mathbf{R}_{T}$  is the terminating resistor on the recording end of the signal cable,  $\mathbf{R}_{C}$  is the resistance of the signal cable, M is the mutual inductance of the gage, and X is the length of the gage coils. V(t), I(t), and u(t) are the voltage, current, and particle velocity, respectively. V(t) is measured with respect to the zero-particle-velocity baseline measured in preshot calibrations. Because of the time-varying current and the inductive nature of the gage, the baseline itself is a time-varying voltage.

# Instrumentation Improvements for LASS Experiments

One of the major objectives of the field experiments was to obtain records of sufficiently good quality to permit taking full advantage of the LASS technique. Problems encountered in previous field experiments included premature gage failure (i.e., before complete unloading) at stresses above about 1 GPa, severe electrical noise pickup, and poor signal-to-noise ratio for mutual inductance particle velocity gages at low particle velocities. Electrical crosstalk between gages was also a problem. The improvements described below allowed us to obtain laboratory-quality gage records from both LASS experiments.

Premature gage failure has been traced to a variety of causes including shear failure at the gage package-cable junction, voids in the grout column, and cracking of the grout column (due to excessive moisture loss). The shear failure problem appears to have been solved by simple modifications in the construction of the gage package, shown in Figure 5(b). The RG-8 lead exits the package at a 30-degree angle (rather than in the plane of the package) and loops around to join the PVC pipe used as an installation handle. This package design was also used with good results in the 100-ton TNT and 120-ton ANFO Pre-Dice Throw II events. Voids in the grout column were avoided by careful grouting from the bottom of the hole, and the choice of a wet site circumvented the grout cracking problem. Figure 6 is a reproduction of a LASS 1 stress gage record showing recording duration extending through complete unloading from a peak stress of 1.71 GPa.

The major instrumentation improvement in the WSMR LASS experiments was the modification of the mutual inductance particle velocity gage power supplies for remote operation. This allowed us to place the power supplies near the experiment rather than in the instrumentation van, as had been previous practice. The power supplies were placed in a plywood shelter, protected by sandbags, about 50 m from the LASS 2 GZ (Figure 1).



MP-4663-13

FIGURE 6 LASS 1 STRESS GAGE 1 RECORD.
Peak stress is 1.7. GPa.

Close-in power supply placement effectively eliminates the problem of noise pickup caused by inductive coupling between power supply leads and signal leads. The IR drop in the power leads is reduced, and since the gage signal depends linearly on gage current, the signal-to-noise ratio at low particle velocities is substantially improved. An additional advantage is a substantial reduction in cable costs. In previous field tests it was necessary to use high-cost low-resistance cables (RG-331) for power supply leads whenever the run was over about 300 m. Even so, typical gage currents were limited to 50-70 amperes by cable resistance. In contrast, gage currents in the present experiments were about 175 amperes. Figure 7 is a reproduction of a LASS 1 MIPV gage record, showing good signal-to-noise ratio even at a particle velocity of about 15 m/s.

Major sources of electrical crosstalk between gages are ground loops and inductive coupling between cables. The ground loop problem was minimized by floating all the power supplies and the instrumentation van. A ground loop can be created when a gage shorts to ground as a result of shock wave damage. If this short occurs early with one of the close-in gages, the records of the gages further out can be affected. With a floating instrumentation van, two close-in gages must short to ground before a ground loop can form.

Inductive coupling between cables was negligible in LASS 1. We had time to achieve a very clean cable layout. Each signal cable was separated from parallel adjacent cables by at least 15 cm over the entire run from shot to instrumentation van, and all cable crossings were at right angles. The LASS 1 cables were reused for LASS 2, and we had to forego a clean cable layout in order to meet the firing schedule. Although the LASS 2 records are much better than previous field records, they are inferior to the LASS 1 records.

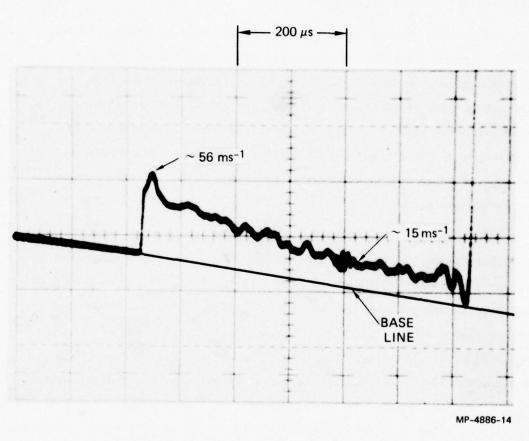


FIGURE 7 LASS 1 PARTICLE VELOCITY GAGE 9 RECORD

#### FIELD TEST DATA AND DISCUSSION

Composite experimental data for LASS 1 and LASS 2 are presented in Figures 8 through 11, and the individual gage profiles are presented in Figures 12 through 15. The original gage records were digitized on a Telerecordex. Simple computer programs apply the calibration data to the digitized records to convert the measured voltage histories to stress and particle velocity histories.

To prepare the data for further reduction and to prepare Figures 8-11, we redigitized the gage profiles at uniform time steps of 2.5  $\mu$ s and removed obvious noise glitches. The solid lines of Figures 12 through 15 show the original profiles, and the dashed lines show the profiles after noise removal. Noise glitches can be unambiguously identified by their simultaneous occurrence on two or more records. In general, a noise burst at late time coincides with the failure of one of the close-in gages.

The results of the WSMR LASS experiments demonstrate that it is possible, under field conditions, to obtain good quality, long duration, stress and particle velocity records over the stress range between 0.05 and 2 GPa. However, all the problems of field measurements have not been solved. Further attention should be given to the problem of gage emplacement in dry soils, in which drying out and cracking of grout columns can lead to early gage failure. Stress gage systems suitable for use in the range below about 0.05 GPa have not yet been adequately developed, although standard accelerometers can be used for particle velocity measurements in this range.

We were able to minimize the electrical noise problem because we had good control over the instrumentation and cabling. However, in the typical large-scale field experiment, instrumentation responsibilities are divided among several agencies, and mutual interference is the rule. Nevertheless, current field recording systems for both stress gages and particle velocity gages could be improved to reduce their sensitivity to resulting extraneous electrical fields.

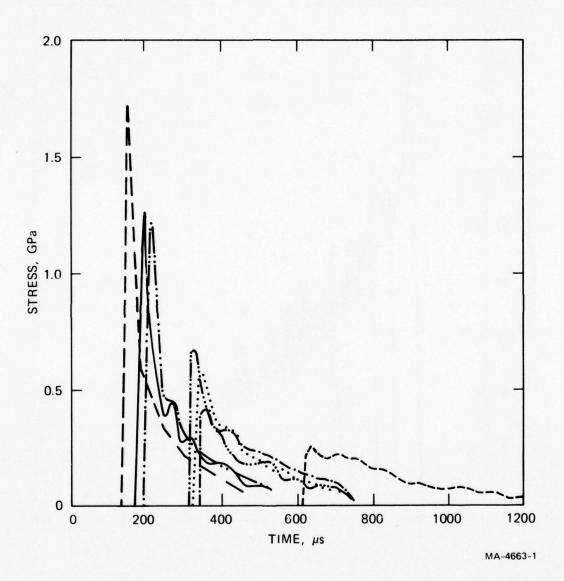


FIGURE 8 RADIAL STRESS HISTORIES, LASS 1.

Gages located 0.526, 0.655, 0.692, 0.942, 0.987, 0.999, and 1.58 m from charge center.

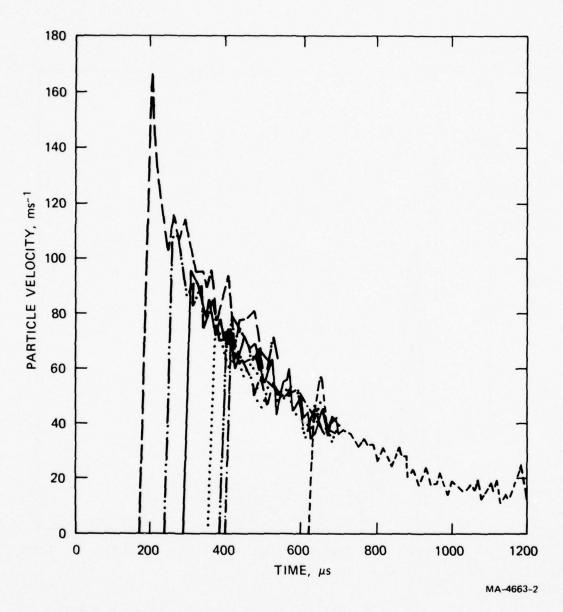


FIGURE 9 PARTICLE VELOCITY HISTORIES, LASS 1.
Gages located 0.610, 0.701, 0.930, 1.02, 1.10, and 1.65 m from charge center.

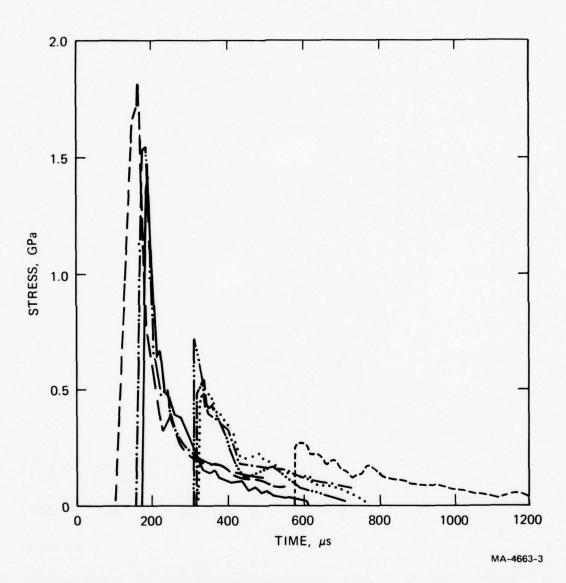


FIGURE 10 RADIAL STRESS HISTORIES, LASS 2.

Gages located 0.540, 0.611, 0.631, 0.950, 0.959, 0.976, and 1.51 m from charge center.

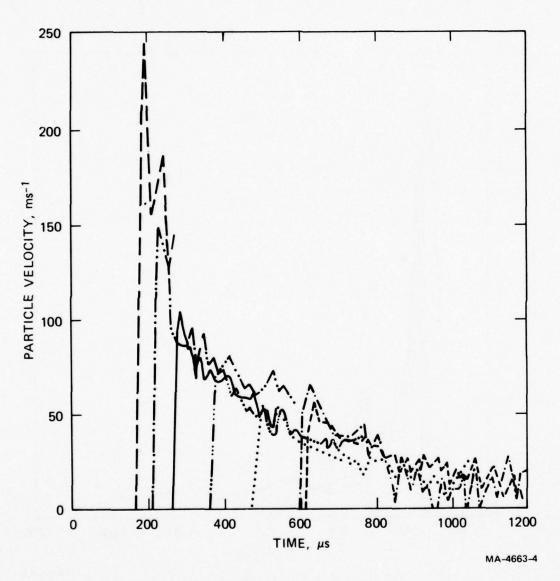


FIGURE 11 PARTICLE VELOCITY HISTORIES, LASS 2.
Gages located 0.610, 0.732, 0.884, 1.07, 1.31, 1.49, and 1.62 m from charge center.

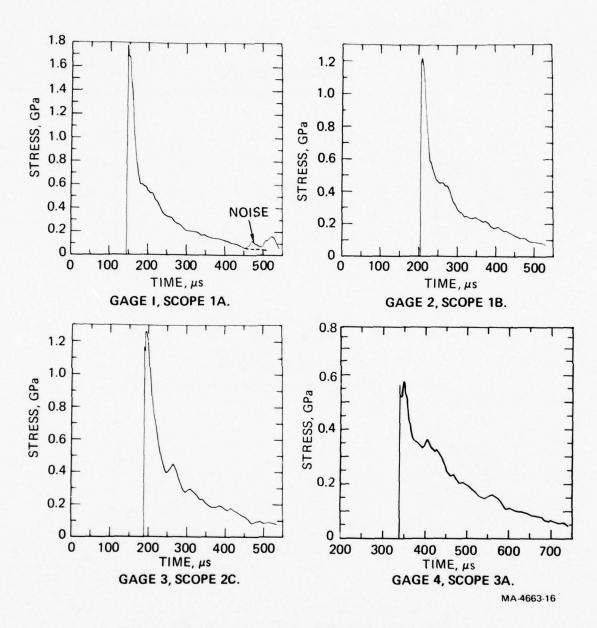


FIGURE 12 INDIVIDUAL STRESS GAGE RECORDS, LASS 1

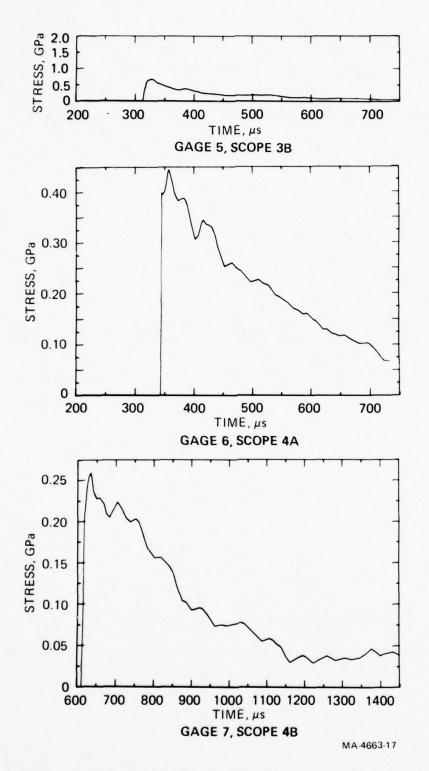


FIGURE 12 INDIVIDUAL STRESS GAGE RECORDS, LASS 1 (Concluded)

The vertical scale for gage 5 was compressed during computer plotting; the recording sensitivity is comparable to the other gages.

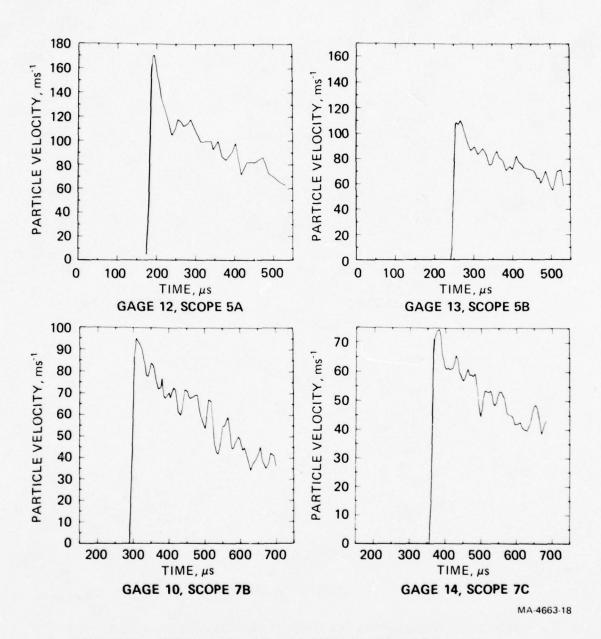


FIGURE 13 INDIVIDUAL PARTICLE VELOCITY GAGE RECORDS, LASS 1

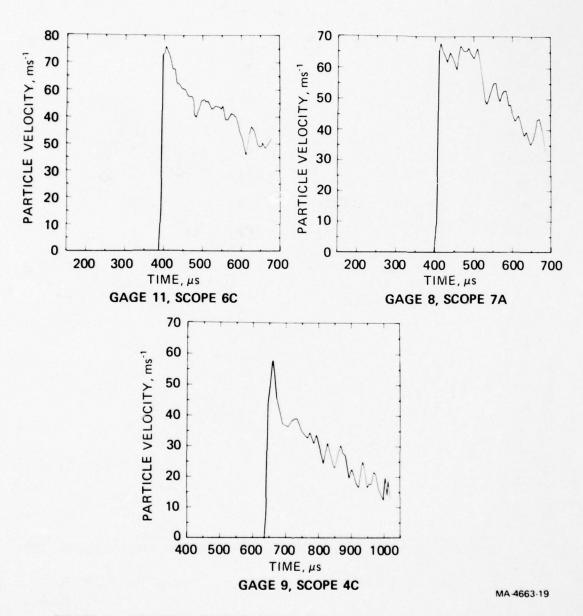


FIGURE 13 INDIVIDUAL PARTICLE VELOCITY GAGE RECORDS, LASS 1 (Concluded)

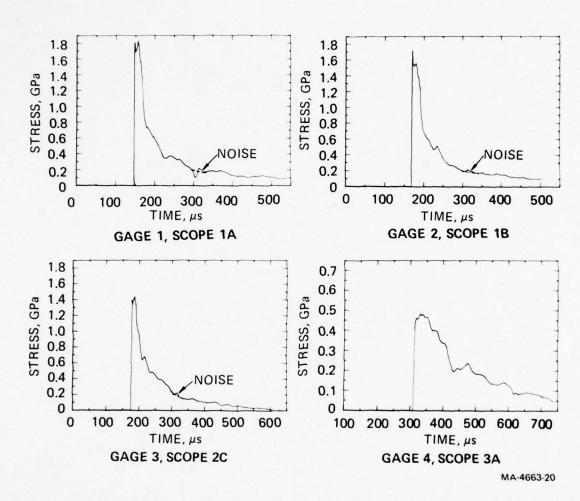


FIGURE 14 INDIVIDUAL STRESS GAGE RECORDS, LASS 2

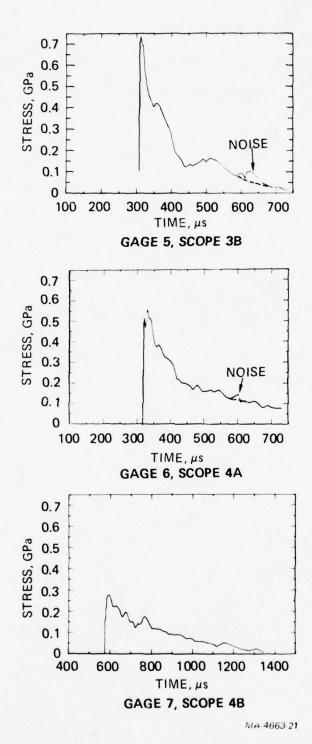


FIGURE 14 INDIVIDUAL STRESS GAGE RECORDS, LASS 2 (Concluded)

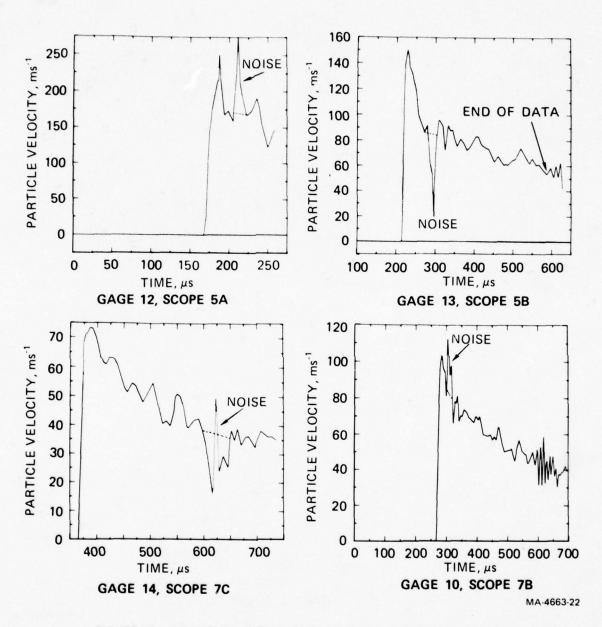


FIGURE 15 INDIVIDUAL PARTICLE VELOCITY GAGE RECORDS, LASS 2

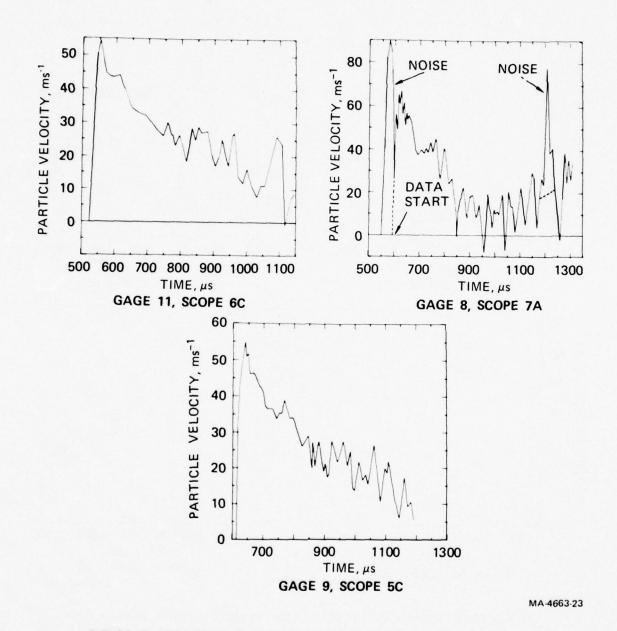


FIGURE 15 INDIVIDUAL PARTICLE VELOCITY GAGE RECORDS, LASS 2 (Concluded)

#### 3. LASS ANALYSIS OF FIELD TESTS

The piecewise linear form of LASS (Appendix A) was used to analyze data from the two spherical field tests, LASS 1 and LASS 2. The objectives were to proof test LASS using field data from a site of interest to DNA and to obtain dynamic in situ material property information for the test material, wet clay from the Pre-Dice Throw II site. Both objectives were satisfied.

### SMOOTHING

The first step in this form of LASS is to presmooth the records to reduce random high frequency noise. The field test records were smoothed with the new modified low-pass filter technique described in Section 4. Specific smoothing parameters are given in Appendix C. The resulting smoothed records are shown in Figures 16 through 19. These may be compared with the original data, Figures 8 through 11, to judge the relatively small amount of smoothing imposed (significant features are not lost).

### LASS 1 ANALYSIS AND RESULTS

The smoothed stress profiles from LASS 1, Figure 16, were used to generate a five-sheet \* gage flow surface for the piecewise linear analysis. Five characteristic features, or knots, in addition to the foot of the wave were identified on each record. Sequentially from the foot these were: the peak  $\sigma_{\rm max}$ , feature A, feature B, feature C,

This terminology refers to the number of piecewise linear sections, or sheets used to characterize the gage flow surface. Figure A4 in Appendix A shows a four-sheet gage flow surface with four piecewise linear gage traces on it crossing each sheet.

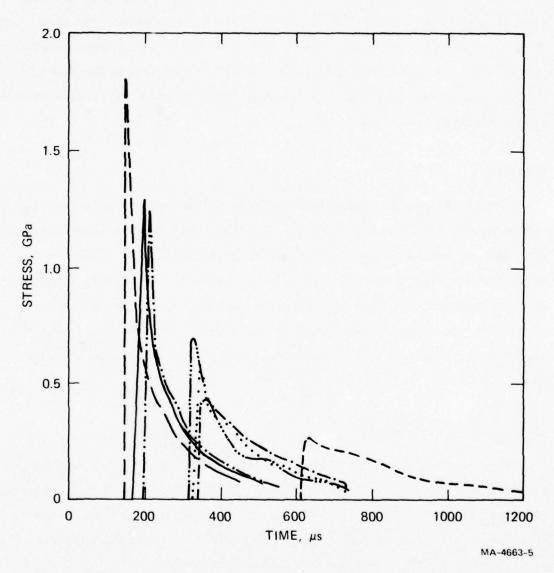


FIGURE 16 SMOOTHED RADIAL STRESS HISTORIES, LASS 1.
Gages located 0.526, 0.655, 0.692, 0.942, 0.987, 0.999, and 1.58 m from charge center.

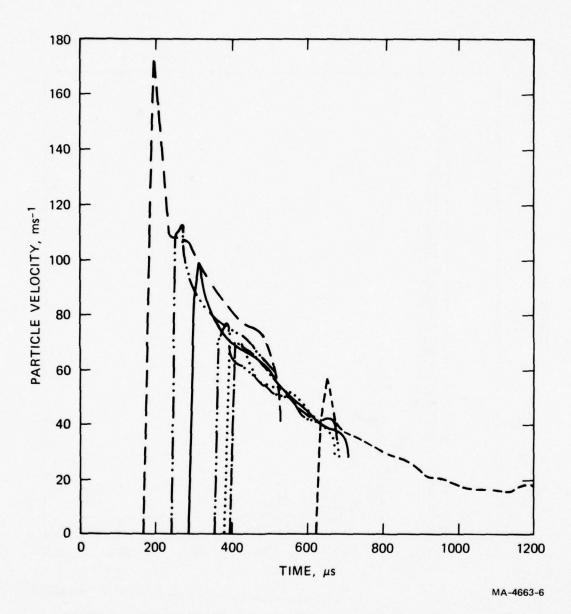


FIGURE 17 SMOOTHED PARTICLE VELOCITY HISTORIES, LASS 1.

Gages located 0.610, 0.701, 0.930, 1.02, 1.10, and 1.65 m from charge center.

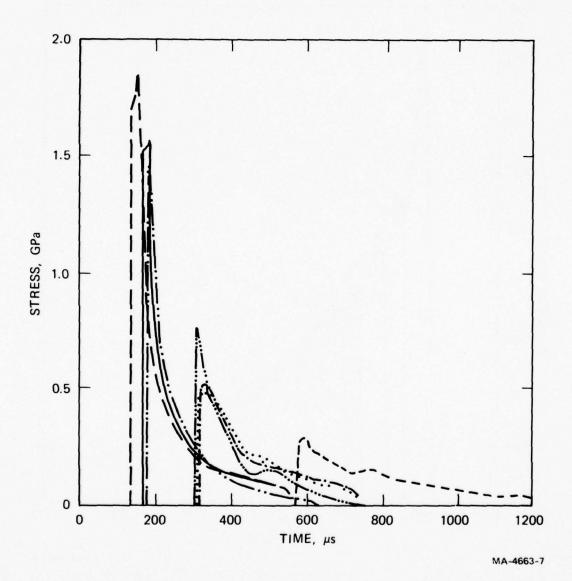


FIGURE 18 SMOOTHED RADIAL STRESS HISTORIES, LASS 2.

Gages located 0.540, 0.611, 0.631, 0.950, 0.959, 0.976, and 1.51 m from charge center.

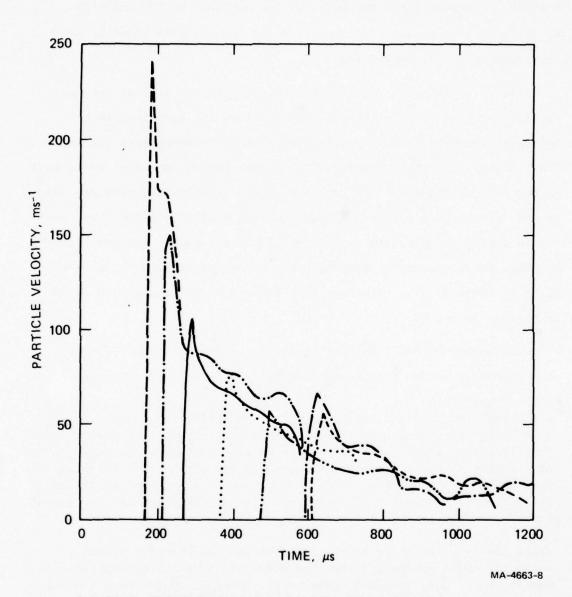


FIGURE 19 SMOOTHED PARTICLE VELOCITY HISTORIES, LASS 2.
Gages located 0.610, 0.732, 0.884, 1.07, 1.31, 1.49, and 1.62 m from charge center

and  $0.1\,\sigma_{max}$ . These features are illustrated on an individual record in Figure 20. These particular five knots were selected because they adequately represent the stress gage flow surface and because they result in a satisfactory representation of the particle velocity gage flow surface, as discussed later.

Next, the relative time (time measured from the foot of the wave at that Lagrange coordinate) and the amplitude for each knot were smoothly connected in the spatial direction by least-squares fitting to functions of Lagrange coordinates, h. Specifically, the time of arrival of the foot of the wave was fit to a linear function of Lagrange coordinate h (initial particle position) and the rest of the features were fit to linear or quadratic exponential functions of h. The specific analytic functions and parameters used for the stress link lines are given in Table 2. The resulting link lines and data points are shown in Figures 21 and 22.

The smoothed LASS 1 particle velocity profiles, Figure 17, were also characterized by five knots in addition to the foot of the wave to

Since the time of first motion in stress and particle velocity is the same, both stress and particle velocity data are generally used to fit this feature. In the present case, however, because of the soupy nature of the site material, the locations, h, of the particle velocity gages were known more accurately than those of the stress gages, as discussed in Section 2. Consequently, only particle velocity gage data were used to fit the foot link line.

Since the relative times at which the stress and particle velocity maxima occurred appeared to scatter about the same curve within experimental error, data from both gage types were used to fit this feature and the resulting link line was used to represent the peak in both gage flow surfaces. When the data scatter about a single curve, fitting them together improves accuracy as discussed in reference 1.

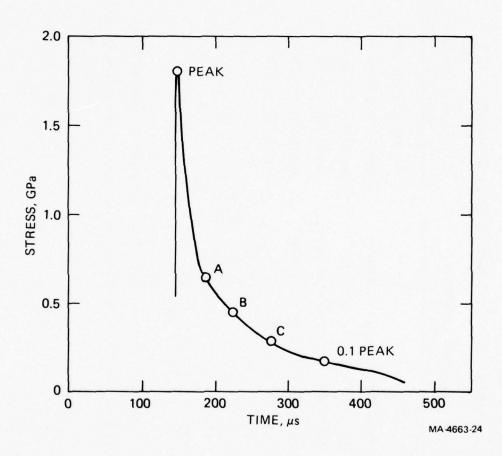


FIGURE 20 FEATURES USED TO CHARACTERIZE LASS 1 STRESS RECORDS FOR PIECEWISE LINEAR LAGRANGE ANALYSIS.

The five features are shown on the stress record from 0.526 m.

Table 2

LASS 1 STRESS GAGE FLOW SURFACE LINK LINES  $^{\rm a}$ 

Relative Time <sup>b</sup> Link Line x µs <sup>-</sup> 1	99.84 + 447.6h <sup>c</sup>	exp(1.602 + 1.093h)	$\exp(3.547 + 0.4528h)$	$\exp(3.987 + 0.5145h)$	$\exp(4.757 + 0.2679h)$	$\exp(4.315 + 2.173h - 0.4866h^2)$
Amplitude Link Line x 10 GPa <sup>-1</sup>		$\exp(4.873 - 4.395h + 1.205h^2)$	$\exp(2.591 - 1.668h + 0.3341h^2)$	$\exp(1.891 - 0.7223h - 0.02481h^2)$	$\exp(1.135 - 0.3992h - 0.01014h^2)$	exp(1.756 - 2.312h)
Feature	Foot	Peak, omax	A	В	D	0.1 σ <sub>max</sub>

a h in meters.

O

Relative time is time measured from first motion (arrival of foot of wave). Q

This feature is fit in real time; relative time is zero by definition at the foot of the wave.

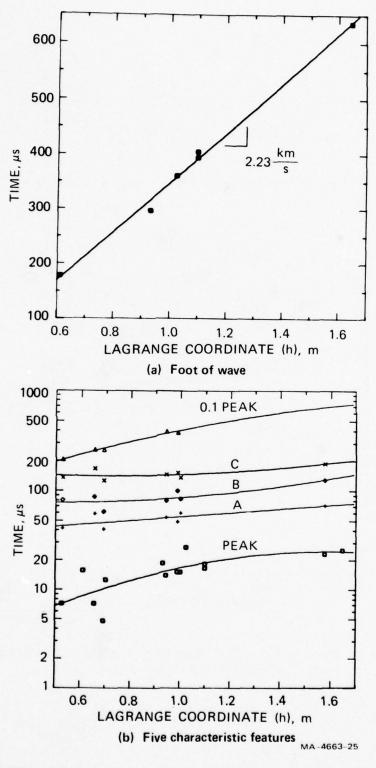


FIGURE 21 TIME LINK LINES FOR LASS 1 STRESS GAGE FLOW SURFACE. Equations for these link lines are given in Table 2.

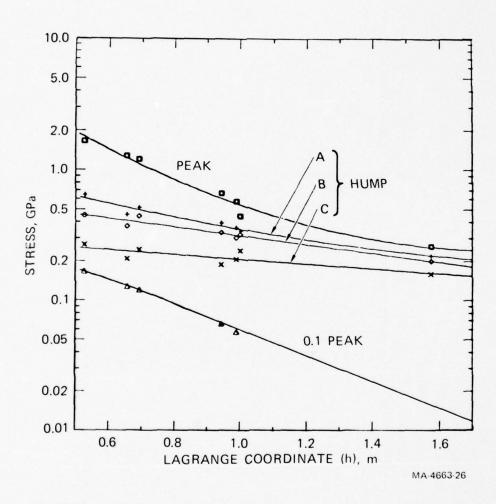


FIGURE 22 AMPLITUDE LINK LINES FOR LASS 1 STRESS GAGE FLOW SURFACE. Equations for these link lines are given in Table 2.

generate a five-sheet gage flow surface. However, these knots were not selected independently of the stress gage features. Instead, at each particle velocity gage location, h, the time of each of the five fitted stress gage flow knots was determined from Figure 21(b). At each of these five times on each smoothed particle velocity record, the amplitude was determined. These are the five knots used to represent the particle velocity records; they are illustrated on one of the individual particle velocity records in Figure 23. This procedure, developed in the previous year to improve the stress difference calculation, ensures compatibility of stress and particle velocity derivatives at joints in the respective gage flow surfaces. With this procedure, the relative time link lines are the same ones used for the stress gages (Table 2 and Figure 21).

The link line functions used to fit the particle velocity amplitudes are given in Table 3 and shown in Figure 24. Stress and particle velocity records generated from the link lines in Tables 2 and 3 are given in Figures 25 and 26 for comparison to the input profiles in Figures 16 and 17.

The link lines in Tables 2 and 3 and an initial density value of 1.85 g/cm<sup>3\*</sup> were used in the LASS subroutine STPV to calculate the stress and strain histories of different particles during the LASS 1 event. From these, any desired stress-strain, stress-stress, or strain-strain cross-plot can be constructed. The results are given in Figures 27 through 29.

Figure 27 shows radial stress versus volume strain at five particle locations within the instrumented region of the flow. For weak site material at high stresses (the present case), radial stress is expected to be very close to mean stress, so Figure 27 is equivalent to a mean stress-volume strain plot. This is often the most important stress-strain information for modeling purposes. Figure 28 gives three other

Private communication, A. E. Jackson, WES.

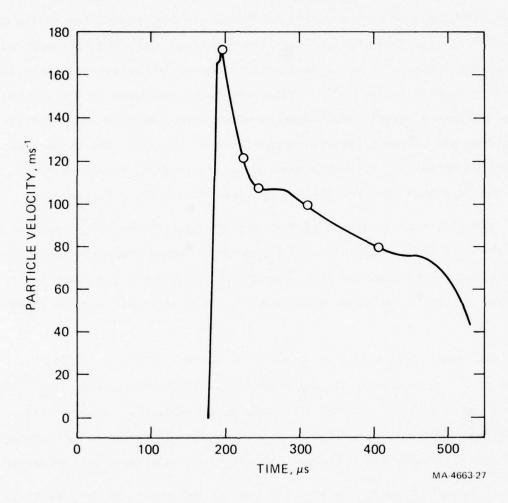


FIGURE 23 FEATURES USED TO CHARACTERIZE LASS 1 PARTICLE VELOCITY RECORDS FOR PIECEWISE LINEAR LAGRANGE ANALYSIS.

These features are derived from the stress records as discussed in the text. The features are shown on the particle velocity record from 0.610 m.

 ${\tt Table~3}$   ${\tt LASS~1~PARTICLE~VELOCITY~GAGE~FLOW~SURFACE~LINK~LINES}^{\tt A}$ 

Featureb	Amplitude Link Line x \mu s/mm	Relative Time Link Line x µs <sup>-1</sup>
Foot		
Peak	exp(-1.454 - 0.9602h)	
A $_{\sigma}$	exp(-1.519 - 0.120h)	Same coefficients as those for $\sigma$ , Table 2
$B_{\sigma}$	$\exp(-1.655 - 1.075h)$	
$^{\mathrm{C}}\sigma$	exp(-1.712 - 1.130h)	
$0.1\sigma_{max}$	exp(-1.247 - 2.160h)	

h in meters.

Features are determined from the stress gage flow surface, as discussed in text.

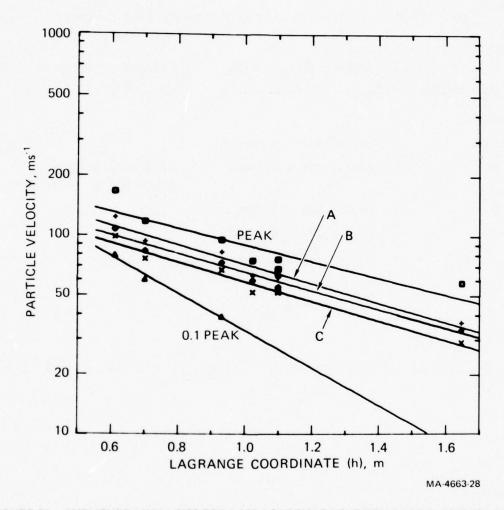


FIGURE 24 AMPLITUDE LINK LINES FOR LASS 1 PARTICLE VELOCITY GAGE FLOW SURFACE. Equations for these link lines are given in Table 3.

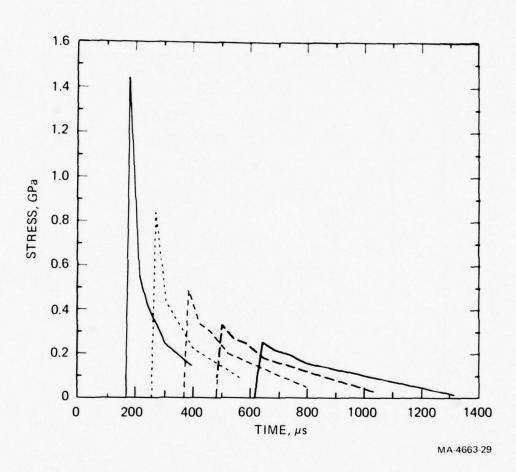


FIGURE 25 PIECEWISE LINEAR GAGE FLOW SURFACE REPRESENTATIONS OF LASS 1 STRESS HISTORIES AT LAGRANGE COORDINATES 0.6, 0.8, 1.05, 1.3, and 1.6 m (measured from charge center)

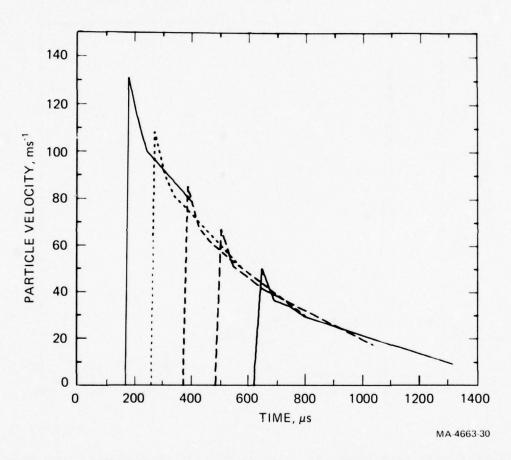


FIGURE 26 PIECEWISE LINEAR GAGE FLOW SURFACE REPRESENTATION OF LASS 1
PARTICLE VELOCITY HISTORIES AT LAGRANGE COORDINATES 0.6, 0.8,
1.05, 1.3, and 1.6 m (measured from charge center)

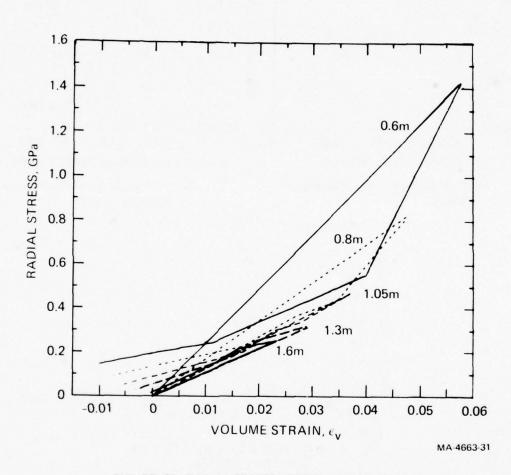


FIGURE 27 RADIAL STRESS VERSUS VOLUME STRAIN, LASS 1

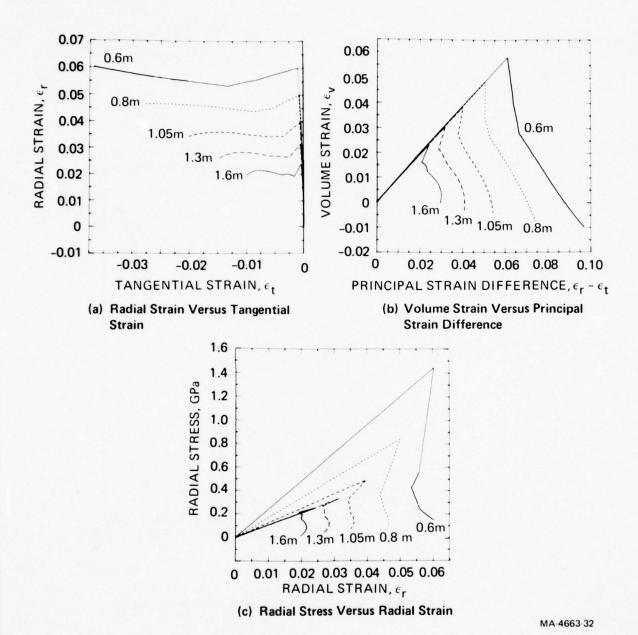


FIGURE 28 RADIAL STRAIN VERSUS TANGENTIAL STRAIN, VOLUME STRAIN VERSUS PRINCIPAL STRAIN DIFFERENCE, AND RADIAL STRESS VERSUS RADIAL STRAIN, LASS 1, AT LAGRANGE COORDINATES 0.6, 0.8, 1.05, 1.3, and 1.6 m

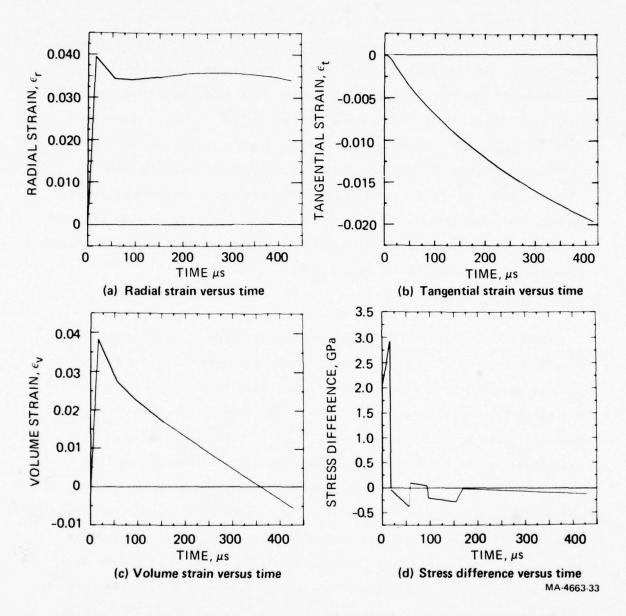


FIGURE 29 RADIAL STRAIN, TANGENTIAL STRAIN, VOLUME STRAIN, AND STRESS DIFFERENCE VERSUS RELATIVE TIME AT LAGRANGE COORDINATE h = 1.05 m, LASS 1

stress-strain or strain-strain cross plots also of interest for modeling, namely, radial strain/tangential strain, volume strain/strain difference, and radial stress/radial strain. Figure 29 gives the individual stresses and strains as function of time for the particle at the middle of the instrumented interval. These trajectories are available for any particle; those for the middle of the analyzed interval, 1.05 m, have been reproduced in Figure 29. From these histories and the radial stress-time profiles in Figure 25, any stress-strain cross-plots such as those in Figures 27 and 28 can be constructed. The results in Figures 27 through 29 are discussed below. Note that in all LASS analyses, results reported at the middle of the h-interval should be considered most accurate because numerical approximations are best there.

#### LASS 2 ANALYSIS AND RESULTS

The IASS 2 analysis approach, except for details, is the same as that used for LASS 1 and the present discussion parallels that for IASS 1. The smoothed IASS 2 radial stress profiles, Figure 18, were characterized by six features in addition to the foot of the wave: the peak  $\sigma_{\rm max}$ , A, B, C, 0.2  $\sigma_{\rm max}$ , and 0.1  $\sigma_{\rm max}$ . These features are illustrated on an individual record in Figure 30. The amplitude and relative time link lines used to connect these knots are given in Table 4 and shown graphically in Figures 31 and 32. Note that as in IASS 1 the time of arrival (real time, not relative time) of the foot of the wave was fit to a linear function using the particle velocity gage data only. Also, as in IASS 1, the relative time of occurrence of stress and particle velocity peaks were fit together by a single function since they scatter about a single curve.

The smoothed LASS 2 particle velocity profiles, Figure 19, were characterized, as in LASS 1, by their amplitudes at the relative times of the fitted knots in stress. The resulting knots on an individual

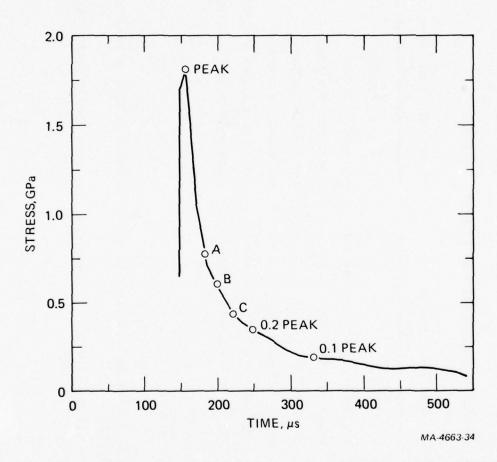


FIGURE 30 FEATURES USED TO CHARACTERIZE LASS 2 STRESS RECORDS FOR PIECEWISE LINEAR LAGRANGE ANALYSIS.

The six features are shown on the stress record from 0.540 m.

Table 4

LASS 2 STRESS GAGE FLOW SURFACE LINK LINES $^{\rm a}$ 

Relative Time <sup>b</sup> Link Line x µs <sup>-1</sup>	-113.8 + 452.1h <sup>c</sup>	$\exp(1.941 + 0.8529h)$	exp(3.518 + 0.1181h)	$\exp(3.857 + 0.4703h)$	$\exp(4.504 + 0.3937h)$	$\exp(2.729 + 3.722h - 0.9409h^2)$	$\exp(3.718 + 3.035h - 0.7922h^2)$
Amplitude Link Line x 10 GPa <sup>-</sup> 1		$\exp(5.270 - 5.079h + 1.493h^2)$	exp(2.661 - 1.201h)	exp(2.249 - 1.063h)	exp(1.368 - 0.7476h)	$\exp(3.728 - 5.189h + 1.535h^2)$	$\exp(2.968 - 5.079h + 1.493h^2)$
Feature	Foot	Peak, omax	А	В	S	0.2 dmax	0.1 omax

h in meters.

a

Relative time is time measured from first motion (arrival of foot of wave) at that Lagrange coordinate h. q

This feature is fit in real time; by definition, relative time is zero at the foot of the wave. o

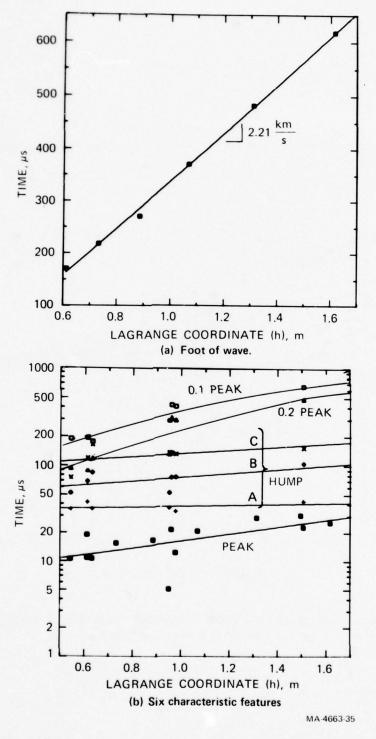


FIGURE 31 TIME LINK LINES FOR LASS 2 STRESS GAGE FLOW SURFACE. Equations for these link lines are given in Table 4.

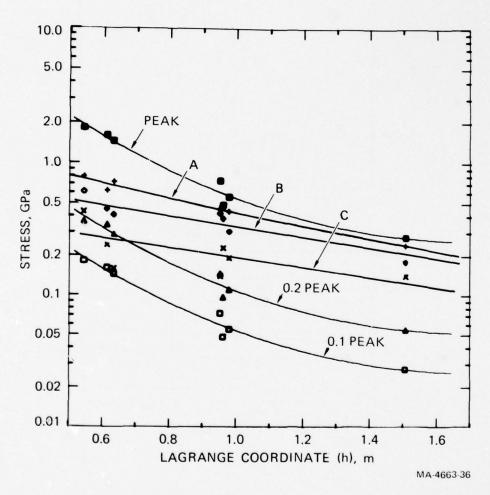


FIGURE 32 AMPLITUDE LINK LINES FOR LASS 2 STRESS GAGE FLOW SURFACE. Equations for these link lines are given in Table 4.

particle velocity record are shown in Figure 33. Because of the procedure used, the relative time-h link lines are the same for the stress and particle velocity records; this was also the case in the IASS 1 analysis. The link lines fit to the particle velocity amplitudes at the knots are given in Table 5 and shown in Figure 34. The stress and particle velocity record representations resulting from this analysis are shown in Figures 35 and 36.

The link lines in Tables 4 and 5 and the initial density value of 1.85 g/cm<sup>3\*</sup> were input into the LASS stress- and strain-calculating subroutines to complete LASS 2 analysis. The results are presented in Figures 37 through 39. Because the quality of the data from LASS 2 was lower than that from LASS 1, it was necessary to reduce the h-interval over which stresses and strains were calculated. Consequently, when comparing the LASS 1 and 2 results, one must take care that the results apply to the same particle position, h, in the flow.

## DISCUSSION

The results from LASS 2 are qualitatively the same as those from LASS 1. The following observations regarding deformation, material response, and accuracy are based on data from LASS 1, but they apply equally to the results of LASS 2.

### Deformation

The idealized deformation of the site material in these spherical experiments is nearly pure radial strain in compression followed by nearly constant radial strain during release (see, for example, Figure 28(a)).

Note that these conclusions can also be inferred from other plots of the

Private communication, A. E. Jackson, WES.

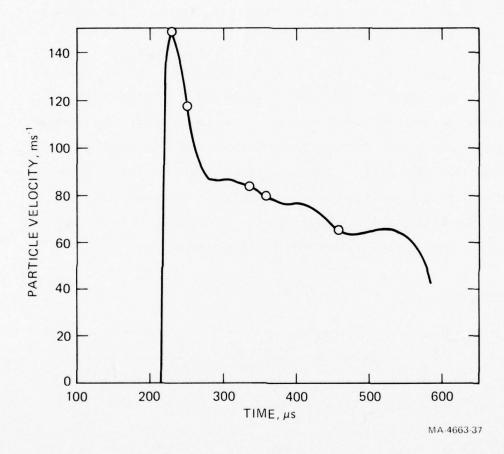


FIGURE 33 FEATURES USED TO CHARACTERIZE LASS 2 PARTICLE VELOCITY RECORDS FOR PIECEWISE LINEAR LAGRANGE ANALYSIS.

These features are derived from the stress records as discussed in the text.

The features are shown on the particle velocity record from 0.732 m.

 ${\tt Table~5}$   ${\tt IASS~2~PARTICLE~VELOCITY~GAGE~FLOW~SURFACE~LINK~LINE}^{\tt a}$ 

Featureb	Amplitude Link Line x µs/mm	Relative Time Link Line
Foot		
Peak, u <sub>max</sub>	exp(-0.9186 - 1.315h)	Same as coefficients for $\sigma$ , Table 4
A <sub>σ</sub>	exp(-1.326 - 1.099h)	
В	exp(-1.346 - 1.286h)	
$c_{\sigma}$	exp(-1.835 - 1.019h)	
$0.2 \sigma_{max}$	exp(-0.9548 - 2.180h)	
0.1 $\sigma_{max}$	exp(-0.9844 - 2.429h)	

h in meters.

b Features are determined from the stress gage flow surface as discussed in text.

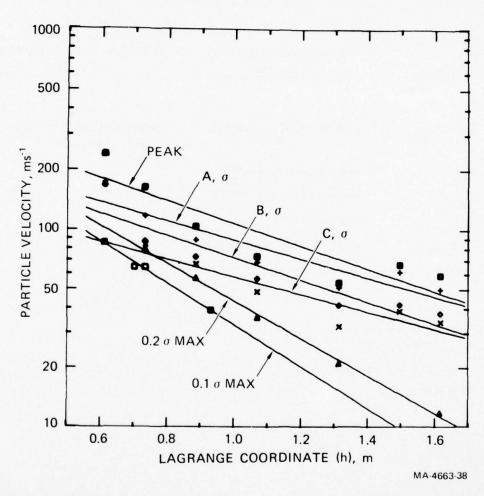


FIGURE 34 AMPLITUDE LINK LINES FOR LASS 2 PARTICLE VELOCITY GAGE FLOW SURFACE. Equations for these link lines are given in Table 5.

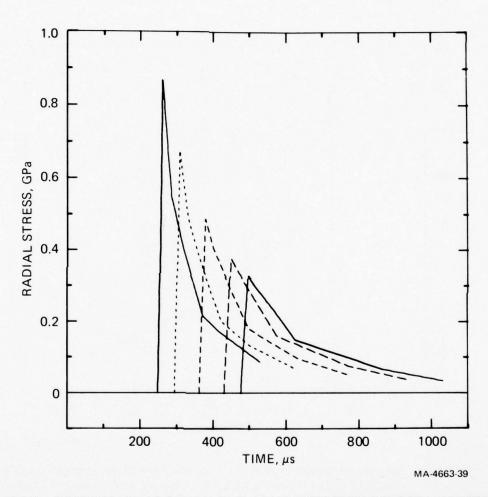


FIGURE 35 PIECEWISE LINEAR GAGE FLOW SURFACE REPRESENTATIONS OF LASS 2 STRESS HISTORIES AT LAGRANGE COORDINATES 0.8, 0.9, 1.05, 1.2, AND 1.3 m

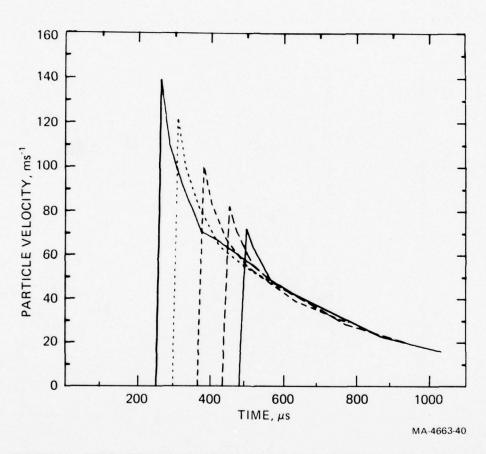


FIGURE 36 PIECEWISE LINEAR GAGE FLOW SURFACE REPRESENTATION OF LASS 2 PARTICLE VELOCITY HISTORIES AT LAGRANGE COORDINATES 0.8, 0.9, 1.05, 1.2, AND 1.3 m

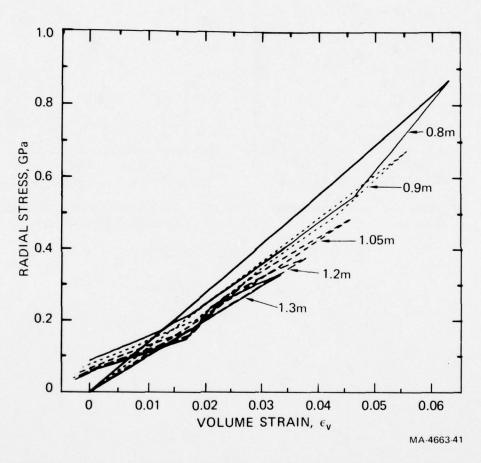


FIGURE 37 RADIAL STRESS VERSUS VOLUME STRAIN, LASS 2, AT LAGRANGE COORDINATES 0.8, 0.9, 1.05, 1.2, AND 1.3 m

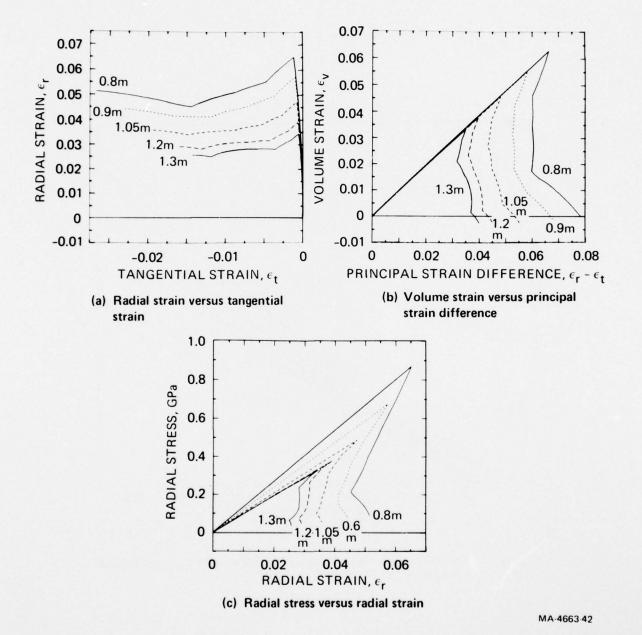


FIGURE 38 RADIAL STRAIN VERSUS TANGENTIAL STRAIN, VOLUME STRAIN VERSUS PRINCIPAL STRAIN DIFFERENCE, AND RADIAL STRESS VERSUS RADIAL STRAIN, LASS 2, AT LAGRANGE COORDINATES 0.8, 0.9, 1.05, 1.2, AND 1.3 m

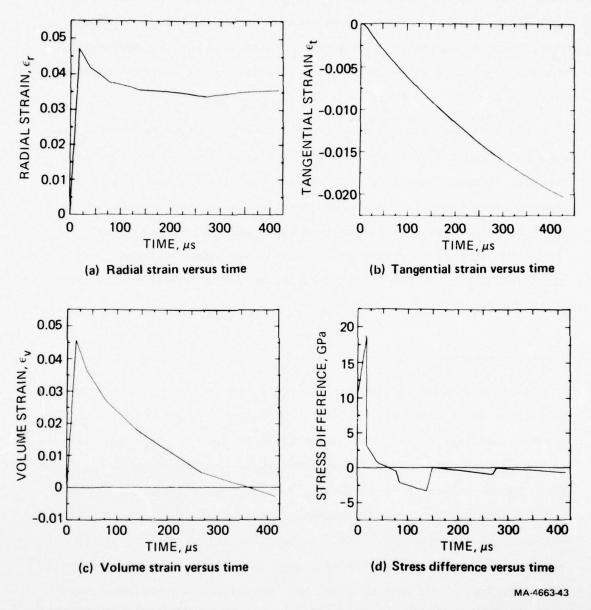


FIGURE 39 RADIAL STRAIN, TANGENTIAL STRAIN, VOLUME STRAIN, AND STRESS DIFFERENCE VERSUS RELATIVE TIME AT LAGRANGE COORDINATE h = 1.05 m, LASS 2

LASS results, such as the individual strain histories in Figure 29 and radial stress-radial strain cross-plot as in Figure 28(c). Although the idealized deformation is one-dimensional (radial) in compression, it is not uniaxial unless the radius of curvature of the wave front at the particle in question is effectively infinite.

The fact that the radial strain is nearly constant in release can also be determined directly from the composite plots of the raw particle velocity records, Figure 9. The release profiles for each gage lie approximately along a single line, meaning that at any instant the radial particle velocities of all particles undergoing release are equal. Therefore there is no change in the radial dimension (thickness) of a small volume element and hence no change in radial strain during this portion of the flow.

#### Material Response

For the purpose of discussing material response, we have reproduced the radial stress-volume strain plots of Figure 27 and added an "equilibrium compression curve," the dark line in Figure 40. This is the locus of end or peak compression states achieved at each particle during loading. In the limits of instantaneous loading and uniaxial strain, this curve approaches the familiar Hugoniot. Remember that the individual trajectories calculated by LASS represent the actual loci of states traversed by individual particles during the dynamic load-release cycle; the particles do not load up along the "equilibrium compression curve" in high rate loading.

Note first in Figure 40 that the equilibrium compression-dynamic release paths are nearly reversible until release to low stresses; i.e., the equilibrium behavior of the material is not hysteretic. The loading

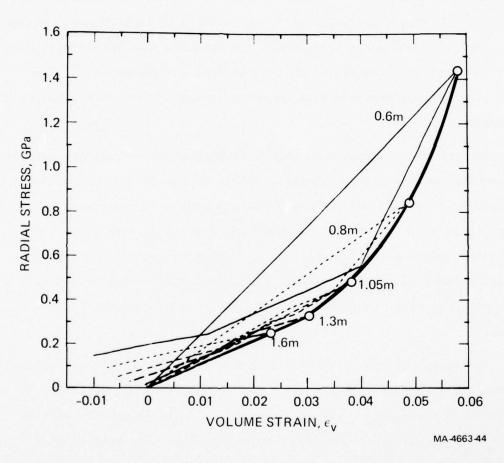


FIGURE 40 RADIAL STRESS VERSUS VOLUME STRAIN, LASS 1, FROM FIGURE 27 WITH EQUILIBRIUM COMPRESSION CURVE ADDED (DARK LINE)

strain rate varies by approximately a factor of 10 among the trajectories from about  $10^4 \mathrm{s}^{-1}$  at 0.6 m to about  $10^3 \mathrm{s}^{-1}$  at 1.6 m. Consequently to the extent that the reversibility observation is valid, and over this strain rate range, the IASS 1 material is rate insensitive. The data in Figure 40 indicate not only that the site material is not hysteretic at high stresses, but that at low stresses it has not been irreversibly compacted. In fact, the trajectories indicate some bulking at zero stress. Finally, note that the relatively high-stress trajectories show no indication of any site material strength or of initial high compressibility. The individual stress profiles also showed no precursor or other evidence of strength.

In summary the results in Figure 40 suggest (1) reversible equilibrium compression-release behavior, (2) no compaction either initially or upon release, and (3) no detectable strength at these stresses. This behavior is very reasonable for clay material below the water table. Quantitative parameters can be evaluated from the LASS plots once a specific model is selected. Comparison of the LASS results with data determined by other tests for the same material is given in the Conclusions.

small errors in the field data or its representation cause large errors in the  $\Phi$  calculation.

In spite of the large expected errors, we did calculate  $\Phi$  from the LASS 1 field data. The resulting  $\Phi$ -t history for the particle at the center of the interval is shown in Figure 29. The initial large positive excursion of about 20  $\mu$ s duration occurs during compression when the flow derivatives and experimental errors in determining them are largest. During release, the derivatives and the errors in estimating them are significantly smaller. In this region the  $\Phi$  estimate shows much smaller excursions (maximum about 0.3 GPa, average about 0.15). These are estimated to be comparable to or less than the error propagated in the calculation (see following error discussion). Consequently, after the first 20  $\mu$ s, the results suggest that  $\Phi$  is bounded by about + 0.1, - 0.3 GPa. Therefore, to the precision and on the scale of these high level tests, the result  $\Phi$  equal zero is permitted. This is consistent with the behavior expected for a wet clay for which  $\Phi$  should be on the order of  $\Phi$  10-3 GPa or less.

## Errors

Three sources of error in the LASS results have been identified and considered. These are (1) deviations from the assumed flow symmetry (spherical in this case), (2) errors in taking the field measurements and reducing them to the form in Figures 8 through 11 where they are ready for LASS analysis, and (3) numerical or modeling errors related to the representation of the records (piecewise linear in this case) and to the numerical approximations in the LASS analysis. After examining the field records, especially those from gages located at similar ranges but along different azimuths, we consider the first error source (deviations from spherical symmetry) to be insignificant compared

with the other sources for both LASS field tests. The magnitudes of these other errors are discussed below.

To estimate the effect of input errors on the calculations, we used results of the global Lagrange analysis and error propagation feasibility demonstration performed on the LASS 1 data and described in Section 4. This is the first time any quantitative error propagation analysis has been attempted for LASS calculations, and the resulting estimates are meant to indicate only analysis sensitivity and order of magnitude of the errors. The approach is not rigorous since different analyses (global and piecewise linear) have been used to estimate the errors and to calculate the results, since the global analysis itself was quite crude (see Section 4), and since the errors in the input are modeled in the simplest way.

The LASS input consists of the presmoothed stress and particle velocity records and the gage locations. The dominant sources of errors in these data are taken to be (1) amplitude errors in the smoothed gage records resulting from gage package variations, calibration uncertainties, and so on, and (2) uncertainties in the gage ranges from the source. For the error propagation analysis, we took the standard deviation in smoothed velocity records to be 5 m s<sup>-1</sup>, in smoothed stress records to be 0.013 GPa, and in the gage locations to be 0.038 m. The resulting standard deviations in the calculated strains and stresses are shown in Section 4. They may be taken as about 15% of the peak strains and as about 0.5 GPa for the stress difference or about 40 times the assumed error in the radial stress measurements. This large error magnification is expected since the radial stresses are about 103 times larger than the expected stress difference. In such cases, the flow equations are not sensitive to the precise magnitude of \$, and \$ cannot be accurately estimated by LASS. Note that 0.5 GPa is about 15% of the peak stress difference calculated for LASS 1.

AD-A063 565

SRI INTERNATIONAL MENLO PARK CA
IN SITU CONSTITUTIVE RELATIONS OF SOILS AND ROCKS. SPHERICAL FI--ETC(U)
APR 77 J T ROSENBERG, P S DE CARLI
DNA-4379F

LOSENBERG, P S DE CARLI
DNA-

To estimate the magnitude of errors attributable to the specific modeling function or characterization selected for the gage flow surface, we performed a second piecewise linear analysis of LASS 1 using seven knots instead of five and quadratic exponential rather than linear exponential functions for the particle velocity amplitude link lines. Because this analysis introduced small artifacts in the representation of the particle velocity gage flow surface near the locus of local maxima, this treatment was somewhat less accurate than the reported LASS 1 analysis. Nevertheless, the differences in gage flow surface representations between the two analyses are probably typical of the largest modeling variations or errors possible in the reported LASS 1 analysis.

Since at the center of the measurement interval (h = 1.05 m) the differences in the strains and stress difference calculated by the two analyses are about 10% of the peak values of the calculated quantities, this may be taken as an estimate of the modeling error in the LASS 1 results. This estimate is consistent with our finding reported last year of 5-10% error in strains calculated with piecewise linear LASS on a test problem for which the solution was known. It is also consistent with the observation in Section 4 that the crude global analysis of LASS 1 performed as a feasibility demonstration of the global technique gave surprisingly reasonable results in spite of large modeling errors.

An estimate of the total error in the calculated results is then the root mean square of the experimental and modeling errors. Therefore the reported LASS 1 results at the middle of the h-interval are estimated to be accurate to about  $\pm$  20% of their peak values.

#### **CONCLUSIONS**

Both field tests yielded a 100% data return and excellent quality records. LASS 1 data are slightly superior to those from LASS 2, as expected, since more nearly ideal procedures were possible in the first shot for logistics reasons. The stress-strain trajectories calculated by LASS for each of the two field tests are estimated to be accurate near the center of the instrumented h-interval to about 20% of their peak values. Results from the two tests are in close agreement qualitatively. Quantitatively, also, most comparable calculations are within 20% of each other, indicating agreement between the two shots to well within experimental error. Efforts were made both in advance and on site to avoid differences in geology between the two test regions, which are separated by about 60 m. Although such geology differences have been observed at the Pre-Dice Throw II site in borings separated by similar distances, <sup>15</sup> none were detected or are known in the present case.

Two other material properties tests have been performed in the PreDice Throw II wet clay stratum in which we fired the field tests:

CIST 15 by AFWL\* and quasi-static laboratory uniaxial strain (UX)

tests by WES. 16 The results of all three tests were compared by

Dr. J. G. Jackson, Jr., of WES at the 1977 DNA strategic structures

meeting and are summarized here in a stress-volume strain plot in

Figure 41. The LASS results are represented by the equilibrium com
pression curves (see Figure 40) based on the data in Figures 27 and 37.

The CIST results are represented by a nearly linear mean stress-volume

strain relation fit to the measured velocity histories and an assumed fail
ure surface; and the UX results by the measured uniaxial strain stress
strain path. All results pertain to the wet clay stratum centered at a

Private communication, G. Wayne Ullrich, Air Force Weapons Laboratory.

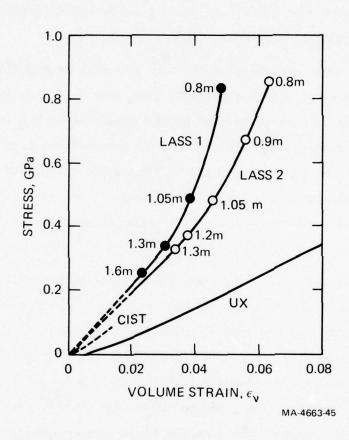


FIGURE 41 STRESS VERSUS VOLUME STRAIN FOR PRE-DICE THROW II WET CLAY FROM THREE DIFFERENT TESTS: LASS, CIST, AND UX

depth of about 3.7 m. Because the strength of the test material is known a priori to be negligible on the stress scale of Figure 41 (Ullrich in fact estimated it to be about  $10^{-3}$  GPa from the CIST data), <sup>16</sup> the stress-strain trajectories for each of the three investigations are essentially hydrostats. However, each "hydrostat" is determined for different deformations (spherical, cylindrical, and uniaxial), different strain rates (from about  $10^4 \, \mathrm{s}^{-1}$  to about  $1 \, \mathrm{s}^{-1}$ ), and different specimen sizes and environments (laboratory and in situ).

Figure 41 shows clearly that the test material is significantly less compressible (by a factor slightly less than three) in the present high strain rate in situ tests than in the quasi-static laboratory tests. The CIST results, determined in situ and at intermediate strain rates ( $\sim$ 10 s<sup>2</sup>), fall between the LASS and UX responses. It should be noted, however, that all the CIST data are determined at stresses below 0.05 GPa and that the accuracy of the results extrapolated to higher stresses is not known.

We conclude from Figure 41 that the results of the three investigations indicate statistically significant response dependence on loading path, strain rate, and environment. Additional sensitivity studies beyond the scope of the present work would be required to determine which of these factors is dominant in altering response. Evidently any material model constructed for the wet clay test material may be in error by about a factor of three unless it is based on data obtained under the conditions of interest or it contains the appropriate path, strain rate, and/or environment dependence.

The objective of the work described in this section was to proof test the IASS technique using field data. We feel that the proof test has been very successful and that the technique is ready for use in characterizing sites of interest to DNA. In addition, valuable new characterization data have been provided for the Pre-Dice Throw II site.

#### 4. ANALYSIS DEVELOPMENTS

LASS has been successfully proof tested with field data and in the future may be one of several techniques used concurrently to determine material properties at sites of interest to DNA. Therefore this year we made extensions to the technique and performed validation studies to establish and/or increase the confidence limits for LASS results. The purpose is to provide information for properly weighting LASS results in material modeling efforts. These extensions and validation studies are described below.

#### **EXTENSIONS**

The three major additions to LASS capabilities this year were; (1) digital smoothing for the field records, (2) an alternative form of Lagrange analysis called the global analysis, and (3) statistical error propagation expressions for the piecewise linear, global, and finite difference Lagrange analyses.

### Digital Smoothing of Field Data

Previously in this program we smoothed the field data "by eye" to eliminate random noise and obvious artifacts before Lagrange analysis. The smoothing was done by the experimenter based on his evaluation of the specific data and on his past experience with similar experiments. Although this procedure is scientifically valid, it is not reproducible or easily documented for those who may wish to reinterpret the data or the LASS results.

This year we formulated and reduced to code a digital low-pass window filtering technique. The technique was used to smooth the LASS 1 and LASS 2 field data (Section 3). The basic approach is to (1) digitize each record at regular time steps, (2) select the number of time steps, data points, or the "window-width," centered about the time step in question over which the data is to be smoothed, (3) Fourier-decompose

the data within the window, (4) filter out the noise using an appropriately shaped filter, (5) retransform to obtain the amplitude of the smoothed function at the center of the window, and (6) repeat at the next time step. The width of the window and the shape of the filter are continuously adjustable as the window moves. In this way we can account for the time-variant nature of the signal and noise. In addition we constrain the procedure to avoid (1) pulse-spreading equivalent to information traveling at greater than local sound velocity (causality violation) and (2) mean-square amplitude attenuation (power loss). The specific procedures used to smooth the LASS 1 and LASS 2 data are given in Appendix C.

# Global Lagrange Analysis

The spherical and cylindrical Lagrange analyses are means of numerically solving the flow equations (conservation of mass and momentum) for unmeasured quantities of interest starting with several experimental measurements of Lagrange radial stress and particle velocity histories (see e.g., Appendix A). These analyses are extremely sensitive to the local estimated values of partial derivatives, which are determined from the discrete spatially separated gage records. Because these field records are often noisy and are determined at widely separated coordinates in the flow, the accuracy of the analysis depends critically on the numerical procedures used to estimate the required intermediate quantities from the individual field records. Three possible approaches are (1) straight finite differences in which time derivatives are taken directly from digitized gage records and spatial derivatives are taken by comparing adjacent records, (2) the piecewise linear analysis discussed in Appendix A in which individual records are represented as piecewise linear functions of time but all records are used to establish spatial dependences and profile amplitude at

an individual gage location, and (3) the global approach discussed below in which a more general global function (not usually piecewise linear in time) is fit to all the data.

With perfect data a sophisticated version of the finite difference approach would be optimal. However, because of the noise in individual field records, the finite difference method is unsatisfactory in this application. Therefore in previous work in this program we developed the piecewise linear Lagrange analysis, which averages over all the gage records. We have demonstrated here and in the earlier work that this method gives good results for all calculated quantities if the stress range of the flow measurements is comparable to the stress difference in the flow. If not, the strains can still be accurately calculated, but the flow is insensitive to the stress difference which is not accurately predicted. To improve the stress difference estimate in this unfavorable condition, we formulated and reduced to code the global analysis, which makes nearly optimal use of the available data.

In this analysis a global model function,  $f_s$ , of Lagrange position h, relative time t, and parameters  $a_i$ ,  $i=1,2,\ldots N$ , is selected and fitted to all the stress records; another function,  $f_v$ , is fitted to all the particle velocity records:

The fitting operation determines values for the model function parameters a and a to minimize the Chi-square error between the model function and the gage records. Once analytic global model functions have been generated

Time measured from the foot of the wave.

for the stress and particle velocity fields, the flow equations (Appendix A) are solvable directly since the necessary partial derivatives and integrals can be evaluated analytically.

Like the piecewise linear Lagrange analysis discussed in Appendix A, the global analysis reduces the effect of random gage errors by systematically averaging (globally smoothing) the gage records. However, it goes beyond the piecewise linear analysis in that it uses the entire gage record rather than just its magnitude at characteristic points, i.e., at the knots in the piecewise linear representations. In this way the global analysis makes more nearly optimal use of the data by extracting information from the regions between the characteristic features, thereby improving time-derivative estimates.

The global analysis is also convenient for enforcing known physical constraints. Such constraints can be enforced during global fitting in three separate ways:

- (1) The constraint can be used to eliminate a parameter from the global model before fitting is attempted.
- (2) The constraint can be strictly enforced during fitting by using Lagrange multipliers.
- (3) The constraint can be weakly enforced by adding a penalty term to the chi-square sum before attempting the fit.

Several examples are discussed below.

Causality is enforced by insisting that both  $f_v$  and  $f_s$  be identically zero before the shock front arrives. That is, the global model is designed so that  $f_v$  and  $f_s$  are always zero, when t<0, where t is relative time. (Recall that t=0 on shock arrival.) The arrival time of the shock front is fitted to a uniform (elastic) or nonuniform (inelastic) form, as the case may be, to relate relative time to real time.

The stress difference  $\Phi$  is known to start from zero at t = 0 and become positive on arrival of the shock front, t > 0. In practice, one parameter of the global model is eliminated with the first (t = 0) condition.

The second condition (t > 0) is enforced during fitting with an inequality constraint.

In the initial (elastic) regime, the stress difference, tangential strain, and radial strain are linked by the following relation:

$$\Phi = g (\epsilon_r - \epsilon_t)$$

where g is constant. When the experimental data contain large errors, it may prove advantageous to enforce this constraint and thereby eliminate another parameter from the model. If the experimental data are well defined, the above condition can be weakly enforced during the fitting procedure. (Both procedures require an a priori estimate of a constant g.) Alternatively, at high stresses  $\Phi$  is often known a priori to be negligible, and the condition  $\Phi = 0$  can be used to correlate the forms of  $f_v$  and  $f_v$ .

In some flows the peak signal will occur at the same relative time for equidistant velocity and stress gages. This constraint is enforced by insisting that

$$\left(\frac{\partial f}{\partial t}\right)_{h} \approx 0 = \left(\frac{\partial f}{\partial t}\right)_{h}$$

at the same relative time, t.

In summary the global analysis is an alternative form of LASS that makes nearly optimal use of the field data, provides built-in data smoothing, and permits enforcement of known physical constraints although it is not necessary to make such assumptions on the material model. As described later in this section we have derived error propagation analyses for it and have used it in several validation studies this year.

## Error Propagation Analyses

This year we performed the first quantitative treatment of error propagation in the Lagrange analyses. For the finite difference, global, and piecewise linear forms of LASS, we derived approximate expressions for the magnitudes of the errors in calculated quantities resulting from propagation of the dominant experimental uncertainties, namely, amplitude uncertainty in the gage records and gage position uncertainties. The treatment was statistical with liberal use of simplifying assumptions and first-order mathematical approximations. The analyses and resulting expressions are presented in Appendixes D through F. The global form, Appendix E, was reduced to code and used in several test problems as described below.

The addition of error propagation capabilities to LASS is a significant advance not only because it allows us to assign confidence levels to LASS results, but also because it permits us to perform pretest sensitivity studies to optimize field test design. For example, proposed tests can be evaluated with regard to both maximum expected accuracy and costeffectiveness of data channel utilization.

## VALIDATION STUDIES

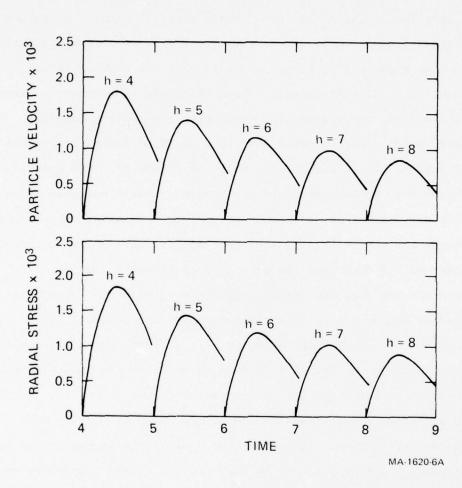
Validation studies were performed to refine, determine the sensitivity of, or otherwise provide information for evaluating or improving the accuracy of present Lagrange analyses. We studied the piecewise linear form of LASS developed previously and used to reduce the LASS 1 and 2 field test data, as well as the global form of LASS developed this year and used to estimate the errors in the field test results. In this work we used an elastic test problem for which we have analytic solutions for all quantities of interest. A more complex inelastic test problem for which we have numerical solutions for all quantities of interest, and the LASS 1 field data. Below we briefly

describe these studies categorized by the form of LASS analysis and the data source and give the primary conclusions drawn from them.

# Piecewise Linear LASS, Elastic Test Problem

A specific set of analytic solutions to an elastic spherical flow problem was described by Grady in a previous report in this program. Five Lagrangian radial stress and radial particle velocity histories at coordinates 4, 5, 6, 7, and 8 from the analytic solution for this problem are reproduced in Figure 42 (note that all quantities are normalized to be dimensionless). These histories correspond to errorfree gage records and provide the input data for testing Lagrange analyses. Grady analyzed these data by a modified finite difference form of LASS to obtain the results shown in Figure 43. The accuracy is within 1/2%. Because the data are perfect, finite differences can give time derivatives as accurately as desired. Consequently the errors that accrue are primarily from imperfect spatial derivative estimates, which must be based on just the five gage stations available. Grady's work demonstrated that the Lagrange analysis approach is feasible given a reasonable number of realistically separated and accurate gages. Note also that the stress difference,  $\phi$ , is well defined by the flow equations (i.e., the Lagrange analysis) in this case in which the magnitude of  $\Phi$ is comparable to the magnitude of the radial stress.

We performed three piecewise linear Lagrange analyses on this problem to test improved numerical techniques and to determine how the LASS accuracy would be degraded by the modeling errors introduced in replacing the correct profiles with piecewise linear representations. Basically the piecewise linear LASS is itself a finite difference analysis but with very large steps, giving much cruder time derivative estimates than Grady's analysis. As stated earlier, this approach is used because conventional finite difference Lagrange analyses of field data are unstable due to the noise in the data.



4.

FIGURE 42 ANALYTIC STRESS AND PARTICLE VELOCITY PROFILES, ELASTIC TEST PROBLEM

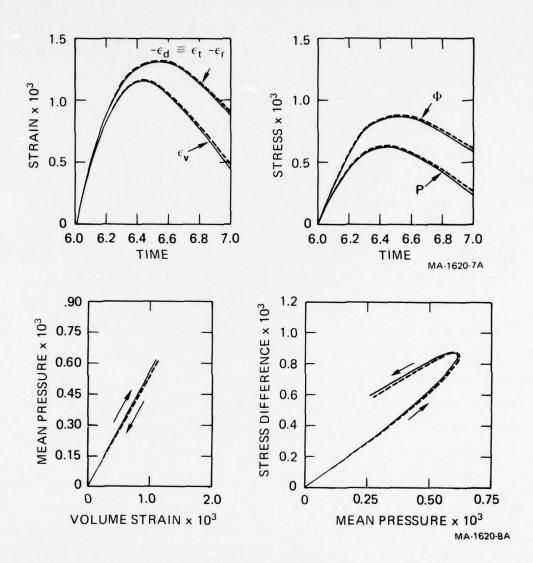


FIGURE 43 FINITE DIFFERENCE LASS CALCULATIONS (SOLID CURVES) COMPARED WITH THE ANALYTIC PROFILES (DASHED CURVES) AT LAGRANGE COORDINATE h = 6, ELASTIC TEST PROBLEM

In the first piecewise linear analysis, the "gage records," i.e., the data in Figure 42, were represented with 10 knots or piecewise linear segments, a relatively large number. The second analysis used only two knots, the minimum number, maximizing modeling error. The third again used 10 knots, but the presumed gage locations were altered randomly to determine analysis sensitivity to the surveying problem encountered in the field. Gage location errors are expected to significantly impare accurate estimates of spatial derivatives. The new perturbed locations of the gages are: 3.886, 4.962, 6.037, 6.977, and 8.063 for particle velocity and 3.899, 4.959, 6.031, 7.044, and 7.991 for stress.

The results of the three calculations, namely, the calculated strains and stress difference at the middle gage position, h=6, are shown in Figure 44 as solid lines. The analytic solutions are shown dashed. The results indicate that the modeling errors detectably affect the calculations, but that the quantitative and qualitative nature of the flow is reproduced with excellent accuracy even for the severe two-knot case. The conclusion is that the present piecewise linear analysis is accurate and stable with respect to modeling and gage position errors. In particular, the stress difference estimates are quite acceptable, within 10% for 10 knots and accurate records and positions. This again is because  $\Phi$  is well defined by the flow parameters in regions where it is comparable in magnitude to the radial stress, at these attenuation rates.

All three of these calculations include two significant improvements over previous piecewise linear analyses. First, the knots in the stress and particle velocity records are chosen to occur at the same relative times at a given Lagrange coordinate. This better correlates the stress and particle velocity record representations and thereby improves the accuracy of calculations comparing derivatives of different gage types. Second, we determined that the analysis is relatively more sensitive to the time-distance representation of the foot of the wave than to the other

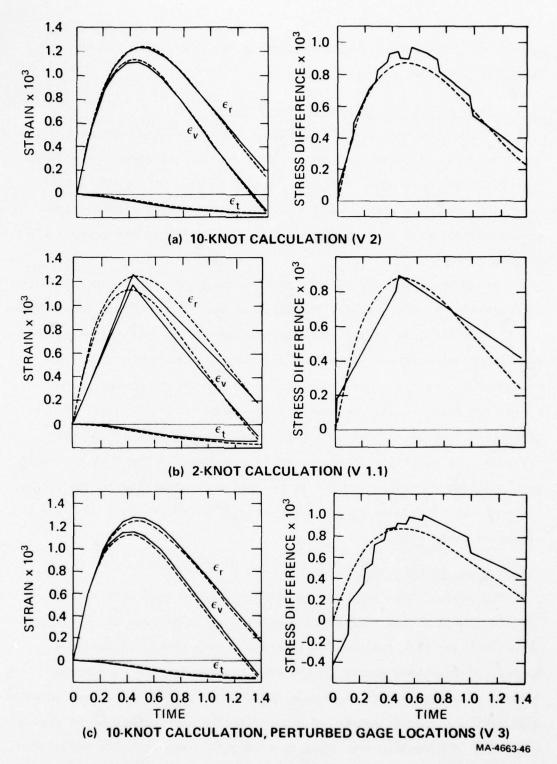


FIGURE 44 PIECEWISE LINEAR LASS CALCULATIONS (SOLID CURVES) COMPARED WITH ANALYTIC SOLUTIONS (DASHED CURVES) AT LAGRANGE COORDINATE h = 6, ELASTIC TEST PROBLEM

link-lines. Therefore, greater attention was devoted to selection of the functional form for this link line.

# Piecewise Linear LASS, Inelastic Test Problem

An inelastic test problem involving a complex flow with an evolving precursor was described last year. This problem was generated with the spherical PUFF code using a known material model. We showed in that work that piecewise linear LASS could calculate radial stress-volume strain trajectories accurate to 5-10% at the center of the gaged region in such a flow.

This year we reanalyzed that problem using the two improvements in the piecewise linear analysis described above. The original and present radial stress-volume strain calculations and the correct trajectories from spherical PUFF are shown in Figure 45. In the new calculation, the accuracy has been somewhat improved in the center of the gaged region and significantly improved at the edges. The calculated  $\Phi$  histories were noisy, because  $\Phi$  is small compared with the radial stresses. On the basis of this work we now estimate that, with five gage stations at which accurate stress and particle velocity histories are obtained, strain calculations to within 5% are possible with the piecewise linear LASS.

# Global LASS, Elastic Test Problem

The elastic test problem was used to perform four sensitivity studies of the global Lagrange analysis. The intent was to determine the effects on this analysis of modeling errors (case 1), modeling errors and amplitude errors in the gage records (case 2), modeling errors, amplitude errors, and gage position errors (case 3), and fewer gage stations (three instead of five) with the same errors as in case 3 (case 4). The results are shown in Figure 46 along with the analytic solution (dashed).

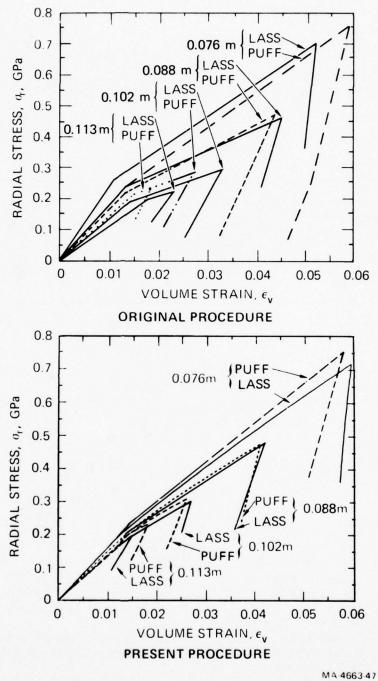


FIGURE 45 PIECEWISE LINEAR LASS RESULTS FOR COMPLEX FLOW PROBLEM GENERATED BY PUFF CODE.

Note that this year's calculations are significantly closer to the correct (PUFF) trajectories everywhere, but especially near the ends of the interval (h = 0.076 m and h = 0.113 m).

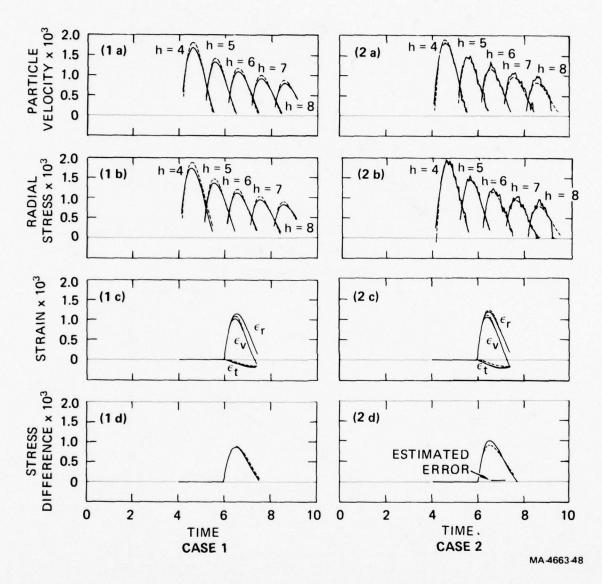


FIGURE 46 GLOBAL LASS CALCULATIONS (SOLID CURVES) COMPARED WITH ANALYTIC SOLUTIONS (DASHED CURVES) AT LAGRANGE COORDINATE h = 6, ELASTIC TEST PROBLEM.

Case 1, modeling errors only; Case 2, Case 1 plus amplitude errors; Case 3, Case 2 plus gage position errors; Case 4, Case 3, but only the middle three gages used in global Lagrange analysis.

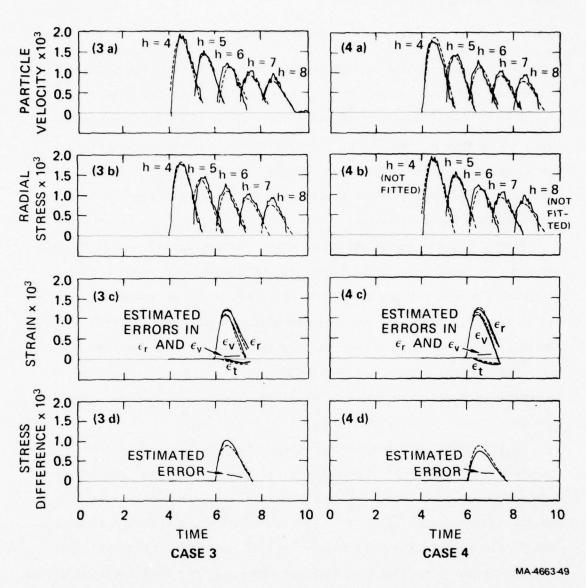


FIGURE 46 GLOBAL LASS CALCULATIONS (SOLID CURVES) COMPARED WITH ANALYTIC SOLUTIONS (DASHED CURVES) AT LAGRANGE COORDINATE h = 6, ELASTIC TEST PROBLEM (CONCLUDED)

Case 1, modeling errors only; Case 2, Case 1 plus amplitude errors; Case 3, Case 2 plus

gage position errors; Case 4, Case 3, but only the middle three gages used in global Lagrange analysis.

<u>Case 1--The stress</u> and particle velocity gage profiles in Figure 42 were fit to the modeling function

$$(At + Bt^2 + Ct^3) \exp (Dt)/(h + 1)$$

where t is relative time at the Lagrange coordinate h. The fit is reasonably good as can be seen from the top two plots for case 1 in Figure 46. The strains and stress difference calculated at h = 6 are shown in the bottom two plots. The differences between calculations and analytic solutions are due solely to modeling errors. Better model functions would reduce these errors, but the present fit would be more than adequate for field work.

Case 2--Random amplitude noise with standard deviation of 10<sup>-4</sup> was added to the gage records of Figure 42 and global LASS rerun. The perturbed records and new model functions are shown in the first two plots, case 2, Figure 46, and the calculations are compared with the analytic solutions in the last two plots. In addition, the propagated error due to amplitude uncertainties of 10<sup>-4</sup> was calculated by the techniques described in Appendix D and are shown in Figure 46. For the strains, these are too small to be in this plot.

Case 3--Gage position perturbations described in the discussion of the piecewise linear LASS calculation for the elastic test problem were then added and global LASS was rerun and errors were reestimated. The results, the analytic solutions, and the estimated errors are shown in case 3, Figure 46. The differences between the calculations and the analytic solution are due to modeling, position, and gage location errors. The error estimate does not include modeling errors.

Case 4--The curves presented in Cases 1 through 3 were obtained by fitting simulated data from five particle velocity and five stress gages. When only three particle velocity and stress gages were used, the results presented in case 4 were obtained. Although profiles are shown at all five gage stations in the first two plots of case 4, only the middle three were

used in the global analysis. Note that the assigned errors increase by a factor of nearly 2 when fewer gage records are available for global fitting.

These calculations demonstrate the type of sensitivity studies that can be performed using a LASS analysis with error estimation capabilities. For example, before a field test, we could specify the degree of the maximum allowable uncertainty acceptable in the results and the expected precision of the experimental measurements and then determine how many data channels were required to achieve the specified accuracy. We could examine the cost effectiveness of deleting channels, improving gage surveying procedures, and so on. The present results also demonstrate that the global LASS is highly stable to noise and position errors.

# Global LASS, LASS 1 Field Test

A preliminary global analysis of the LASS 1 field data presented in Section 2 was performed to test this analysis with real data and to generate approximate error assignments for the Lagrange analysis results in Section 3. Although a very crude model producing severe modeling errors was used in this preliminary analysis, plausible estimates of strains and stress difference were obtained and noise and gage position errors were properly assigned.

The stress and particle velocity profiles were fit to the function

$$At^2 \exp (Bt + Ct^2 + Dh)$$

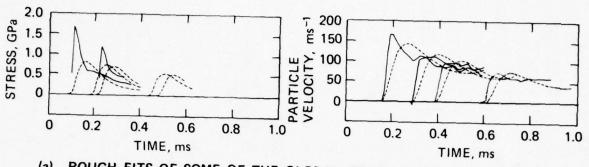
where t is relative time at the Lagrange coordinate h. This form was selected for the feasibility demonstration for convenience and a semblance of plausibility. Other forms can be accommodated with minor changes; however, the noise and gage position errors are propagated correctly regardless of the selected form. As discussed in Section 3, we made the following error assignments:

particle velocity ± 5 ms<sup>-1</sup>
radial stress ± 0.013 GPa
gage position ± 38 mm

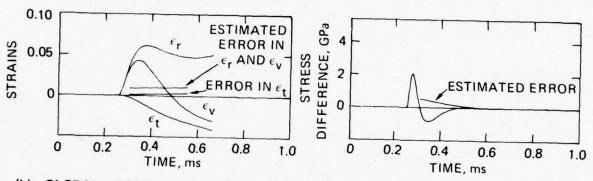
The results, shown in Figure 47, are quite similar to the piecewise linear analysis presented in Section 3 in spite of the large modeling errors evident in plots (a). The most important results in this figure are the ratios of estimated errors to the calculated quantities. These relative error estimates were used in the LASS analysis described in Section 3.

# Finite Difference LASS, Elastic Test Problem and LASS 1

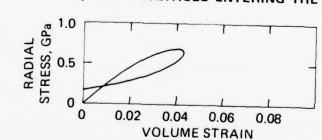
Modified finite difference Lagrange analyses of both the elastic problem and the LASS 1 field data were performed to determine the stability of an analysis using a nonglobal approach to evaluating the temporal derivatives in the flow equations. The spatial derivatives were still determined by path lines and hence use global smoothing. This modified finite difference approach is the method used by Grady to obtain the elastic results shown in Figure 43. The elastic profiles with both noise and gage location errors (case 3, Figure 46) were used. The results for both the elastic problem and the LASS 1 field data are presented in Figure 48. The radial strains are smooth (since they involve only integrals and not derivatives of the gage records) while the volume and radial strains are slightly unstable. The stress difference, appearing in the flow equations as a small difference in two large derivatives of the experimental data, is extremely unstable and oscillates randomly off-scale for the elastic problem. The scale on which the LASS calculation is shown is very insensitive compared with the expected stress difference amplitude of ~10 GPa or it would look the same. These results demonstrate the significant improvements obtained by the global and piecewise linear Lagrange analysis approaches when the experimental data contain errors.



(a) ROUGH FITS OF SOME OF THE GLOBAL MODEL FUNCTIONS (DASHED) TO SOME OF THE FIELD TEST DATA.



(b) GLOBAL LASS CALCULATIONS OF STRAINS AND STRESS DIFFERENCE, WITH ERROR ESTIMATES, FOR A PARTICLE ENTERING THE FLOW AT ABOUT 2.5 ms.



(c) RADIAL STRESS-VOLUME STRAIN AT THE SAME PARTICLE.

MA-4663-50

FIGURE 47 PRELIMINARY GLOBAL ANALYSIS AND ERROR ESTIMATES BASED ON LASS 1 FIELD TEST DATA.

These are preliminary results intended to test and demonstrate the global LASS analysis and should not be quoted or used in any quantitative research related to LASS 1 and LASS 2 field tests.

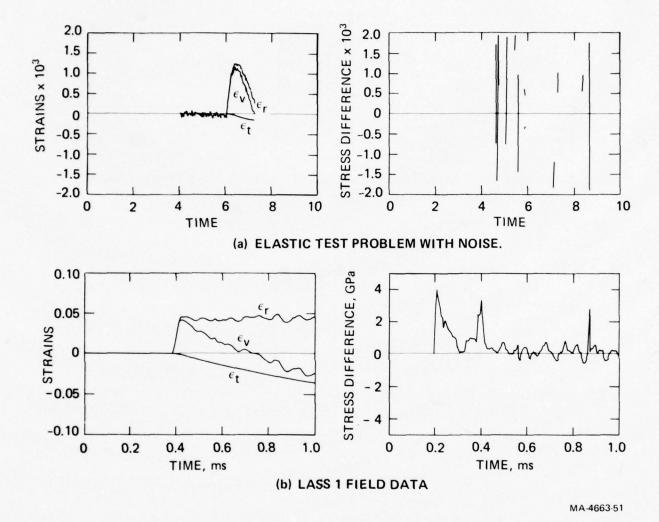


FIGURE 48 FINITE DIFFERENCE LASS CALCULATIONS OF ELASTIC TEST PROBLEM WITH NOISE AND OF LASS 1 FIELD DATA FOR COMPARISON WITH PIECEWISE LINEAR AND GLOBAL CALCULATIONS.

Note that the stress difference calculations are very noisy (off scale for case a) and are reported at smaller Lagrange coordinates than the strain calculations.

#### CONCLUSIONS

The most important conclusions of the validation studies were that (1) stress differences can be calculated by current techniques to 10% given accurate gage records obtained in a flow region where the radial stress is comparable to the stress difference, (2) strains can be calculated to within 5% given a realistic number of accurate records even from a complex flow, (3) the global and piecewise linear Lagrange analyses are not unstable to reasonable perturbations (errors) in the experimental data, and (4) the new error propagation capabilities can be used to assign confidence levels to LASS results or to perform sensitivity studies in advance of field tests to evaluate or improve the probability of achieving the desired test objective.

### 5. CONCLUSIONS AND RECOMMENDATIONS

This year LASS has been successfully proof tested in conjunction with two spherical HE field tests we performed at the Pre-Dice Throw II site. In addition, error propagation capabilities have been added to the technique and tested. We estimate that the LASS results reported for the two field tests are accurate to about 20% of the peak values of the calculated quantities. We have also demonstrated that the LASS approach now allows accurate determination of stress difference if reasonable experimental measurements are obtained in a stress range comparable to the stress difference supportable by the test material.

Based on these results and our understanding of the major material modeling problems of concern to DNA and the status of techniques available in the community to solve these problems, we suggest four research tasks warranting consideration for future work.

- (1) An experimental program to improve dynamic stress measurement capabilities in the important stress range between 10<sup>-3</sup> and 10<sup>-1</sup> GPa. The strengths of many geologic materials of interest lie within this range where we are currently unable to make reliable stress measurements. If reliable measurements are obtained, LASS and perhaps other techniques could be used to obtain material properties data in this important and poorly understood region.
- (2) The application of LASS techniques to future CISTs. If the stress measurement problems can be solved, LASS can be used to reduce CIST data to determine unique stress-strain trajectories and assign confidence levels to them. This would support the objectives and enhance the usefulness of future CISTs.
- (3) LASS sensitivity analyses of proposed field tests. Such analyses can be used to establish the accuracy expected from a given test for comparison with the test objectives. In this

- way the test can be designed either for optimum accuracy given testing constraints or for maximum cost-effectiveness within predetermined accuracy specifications.
- (4) A sensitivity study to evaluate the error caused by applying LASS to data from anisotropic or nonuniform sites that do not support strictly one-dimensional flows. Since LASS has been successfully proof tested, it is desirable to remove, reduce, or quantify this one restriction on its applicability.

#### REFERENCES

- 1. J. T. Rosenberg, C. W. Smith, and D. R. Curran, "In Situ Constitutive Relations of Soils and Rocks," SRI Draft Final Report, DNA 4087F, Menlo Park, California (1976).
- D. E. Grady, C. W. Smith, G. M. Muller, K. D. Mahrer, and
   C. F. Petersen, "In Situ Constitutive Relations of Soils and Rocks," SRI Final Report, DNA 3671Z, Menlo Park, California (1974).
- C. W. Smith, C. F. Petersen, K. D. Mahrer, J. T. Rosenberg, M. J. Ginsberg, and L. B. Hall, "In Situ Constitutive Relations of Soils and Rocks," SRI Final Report, DNA 3678F, Menlo Park, California (1974).
- 4. Stephen E. Davis, "General Test Plan for the Cylindrical In Situ Test (CIST)," AFWL-TR-74-136, Air Force Weapons Laboratory, Kirtland Air Force Base, New Mexico (1974).
- 5. D. D. Keough, C. W. Smith, and M. Cowperthwaite, "Constitutive Relations from In Situ Lagrangian Measurements of Stress and Particle Velocity," SRI Interim Report--Phase I, DASA 2685, Menlo Park, California (1971).
- C. W. Smith, D. E. Grady, L. Seaman, and C. F. Petersen, "Constitutive Relations from In Situ Lagrangian Measurements of Stress and Particle Velocity," SRI Final Report, DNA 2883I, Menlo Park, California (1972).
- 7. D. E. Grady, C. W. Smith, and L. Seaman, "In Situ Constitutive Relations of Rocks," SRI Final Report DNA 3172-Z, Menlo Park, California (1973).
- 8. C. W. Smith, "Dynamic Measurements of Stress Pulses in Tuff at Nevada Test Site," SRI Report, DNA 2811F, Menlo Park, California (1971).
- M. J. Ginsberg, D. E. Grady, P. S. De Carli, and J. T. Rosenberg, "Effects of Stress on the Electrical Resistance of Ytterbium and Calibration of Ytterbium Stress Transducers," SRI Final Report, DNA 3577F, Menlo Park, California (1973).
- 10. A. H. Jones and S. J. Green, "The Role of Material Properties in Determining Ground Motion from High-Energy Detonators," Terra Tek, TR 71-41, Draft Final Report for Defense Nuclear Agency, Salt Lake City, Utah (1972).
- C. W. Smith, "Stress Wave Measurements on the Mine Dust High Explosive Test," SRI Final Report, Contract DNA001-72-C-0235, Menlo Park, California (1972).

- C. W. Smith, "Ytterbium Gage Measurements in Dido Queen and Husky Ace," SRI Final Report for Systems, Science and Software, Menlo Park, California (1973).
- C. W. Smith, "Ytterbium Stress Gage Measurements at the Hardpan Site," SRI Topical Report, DNA 3805T, Menlo Park, California (1975).
- 14. W. J. Murri and C. W. Smith, "Stress Gage Measurements on Pre-Dice Throw II," SRI Project Officer's Report (Draft) for Defense Nuclear Agency, Contract DNA001-75-C-0077, Menlo Park, California (1976).
- 15. A. E. Jackson, Jr., R. F. Ballard, Jr., and J. R. Curro, Jr., "Material Property Investigation for Pre-Dice Throw I and II: Results from the Subsurface Exploration Programs," Waterways Experiment Station Report, Vicksburg, Mississippi (June 1976).
- 16. A. E. Jackson, Jr., and R. W. Peterson, "Material Property Investigation for Pre-Dice Throw I and II: Results from the Laboratory Testing Programs," Final Report, U. S. Army Engineer Waterways Experiment Station, Vicksburg, Mississippi (November 1976).
- 17. R. P. Swift, "Examination of a Static and Dynamic Material Response for a Mixed Company Sandstone," Physics International Technical Report 482 (November 1973).
- 18. Lynn Seaman, "Lagrangian Analysis for Multiple Stress or Velocity Gages in Attenuating Waves," J. Appl. Phys., Vol. 45, No. 10, pp 4303-4313 (October 1974).

## Appendix A

### LAGRANGE ANALYSIS FOR SPHERICAL FLOWS

The LASS analysis for one-dimensional divergent flows calculates the stress and strain trajectories of dynamically loaded in situ site material from field measurements of radial stress and radial particle velocity. The approach is to use the field measurements to numerically solve the partial differential equations defining strains and expressing the conservation of mass and momentum for the flow. The importance of the LASS method is that it is mathematically complete, so no assumptions whatsoever are required concerning the thermodynamic or mechanical constitutive relations of the material. Accuracy is limited only by the degree to which the flow satisfies the symmetry conditions, by the validity of the numerical estimates of partial derivatives, and by the experimental errors in the field measurements. Thus in situ HE events that induce high symmetry (planar, spherical, or cylindrical) flows serve as large material loading machines, and the LASS analysis fully defines the resulting load-response behavior.

The partial differential equations expressing conservation of mass and momentum for planar, spherical, and cylindrical one-dimensional\*

flows may be written

$$\frac{\rho_{o}}{\rho} = \left(\frac{\mathbf{r}}{\mathbf{h}}\right)^{N} \left(\frac{\partial_{\mathbf{r}}}{\partial_{\mathbf{h}}}\right)_{\mathbf{r}} \qquad \text{mass} \qquad (A-1)$$

$$-\rho \left(\frac{\partial \mathbf{u}_{\mathbf{r}}}{\partial \mathbf{t}}\right)_{\mathbf{h}} = \left(\frac{\partial \sigma_{\mathbf{r}}}{\partial \mathbf{r}}\right)_{\mathbf{t}} + N\frac{\Phi}{\mathbf{r}}$$
 momentum (A-2)

 $<sup>^{</sup>st}$  Flows parametrized by one spatial coordinate.

where:

stresses are taken as positive in compression

- o and o are the initial and present densities
- r is the Eulerian radial coordinate
- h is the Lagrange coordinate of a particle, i.e., its initial radial coordinate
- N is a constant with value 0, 1, or 2 for planar, cylindrical, or spherical flows, respectively.
- t is time
- $\boldsymbol{u}_{_{\boldsymbol{r}}}$  and  $\boldsymbol{\sigma}_{_{\boldsymbol{r}}}$  are radial particle velocity and radial stress
- $^{\Phi}$  is the difference between radial and tangential stress ( $^{\sigma}_{r}$   $^{\sigma}_{t}$ )

The definition of radial particle velocity as the time rate of change of Eulerian particle position provides a third flow equation, which may be written in differential or integral form

$$u_{r} = \left(\frac{\partial r}{\partial t}\right)_{h} \tag{A-3}$$

or

$$r = h + \int_{T_0(h)}^{t} u_r(h,\tau) d\tau \qquad (A-3b)$$

Where  $T_0(h)$  is the time of first motion of the particle h.

For N = 0 (planar flow), the system of three equations and four flow variables  $\sigma_r$ ,  $u_r$ ,  $\rho$ , and r can be solved numerically if either stress or particle velocity histories along several particle paths are measured. For the divergent flow cases of interest in this program where N = 1 or 2 (cylindrical or spherical flows), the momentum equation contains an extra term involving the additional flow variable, stress difference,  $\Phi$ . For these flows, both stress and particle velocity histories along several particle paths must be measured to allow the system of equations to be solved for the remaining unmeasured flow variables.

Note that for the divergent flows not all of the five flow variables are independent. Consequently, measurement of some pairs of variables is not sufficient to solve for the others. Inspection of the equations shows that any of the seven pairs that can be formed from  $\sigma_{\mathbf{r}}$ ,  $\Phi$ , and one of the remaining displacement-related variables is sufficient, although some are computationally or practically more convenient. Note, in particular, that no pair of displacement-related variables is independent. All work to date has used the pair  $\sigma_{\mathbf{r}}$  and  $\sigma_{\mathbf{r}}$ .

To provide stress-strain trajectories for the divergent flows, the analysis further calculates strain histories from the displacement field r(h,t). The following principal engineering strain definitions are used to evaluate radial strain  $\epsilon_r$ , tangential (hoop) strain  $\epsilon_t$ , and volume strain  $\epsilon_r$ :

$$\epsilon_{\mathbf{r}} = 1 - \left(\frac{\partial_{\mathbf{r}}}{\partial \mathbf{h}}\right)_{\mathbf{t}}$$
 (A-4)

$$\epsilon_{t} = 1 - \frac{r}{h} \tag{A-5}$$

$$\epsilon_{\mathbf{v}} = 1 - \left(\frac{\mathbf{r}}{h}\right)^{N} \left(\frac{\partial \mathbf{r}}{\partial h}\right)_{\mathbf{t}} = 1 - \frac{\rho_{\mathbf{o}}}{\rho}$$
 (A-6)

LASS methods for solving equation (A-1) through (A-6) have been described in several of our reports. 1-3,7 The general procedure is that the field data are smoothed by low-pass filtering, if necessary, and fitted to a functional form. The functions may be either piecewise-linear in time (the piecewise linear analysis) or a general analytic function of h and t (the global analysis). Alternatively, one may estimate the required partial derivatives by straight finite differences (the finite difference analysis); this analysis, however, is generally not useful with field data because unavoidable experimental errors in the data make the derivative estimates excessively noisy. The

fitted representations are then used to solve the flow equations, (A-1) - (A-3), and the defining strain equations, (A-4) - (A-6), for the instantaneous values of all components of the stress and strain tensors at any location in the flow. (Note, however, that accuracy is greatest near the center of the measurement interval.) Uncertainties may be estimated by normal error propagation methods (see Section 4) once the uncertainties in the initial measurements are specified.

The basic approach of the piecewise linear IASS analysis developed in this program is described below. The global and finite difference analyses use standard methods and are not discussed here.

The first step in the piecewise linear analysis is to use the individual field records  $\sigma_{r}(h_{i},t)$  and  $u_{r}(h_{i},t)$  to create analytic representations for the gage flow surfaces, the  $\sigma_{r}$  and  $u_{r}$  surfaces over the h-t domain spanned by the measurements. The field records are constant -h traces on these surfaces as shown schematically in Figure A-1.

The major problem in creating accurate representations of the gage flow surfaces, or in performing any LASS analysis, is the high level of noise and other anomalies often present in field records. These occur both because of the difficulty in making precise measurements outside the laboratory and because of the numerous geologic inhomogeneities present in real sites. To handle the problem of errors in individual gage measurements, we use all the gage measurements to establish an averaged flow surface amplitude at specific h<sub>i</sub>,t coordinates. Having created an averaged mathematical representation of the gage flow surface, we can then generate smoothed estimates of individual records as needed to solve equations (A-1) through (A-6). This technique is more circuitous than using the field records directly, but it significantly improves the accuracy of the calculations and is computationally convenient.

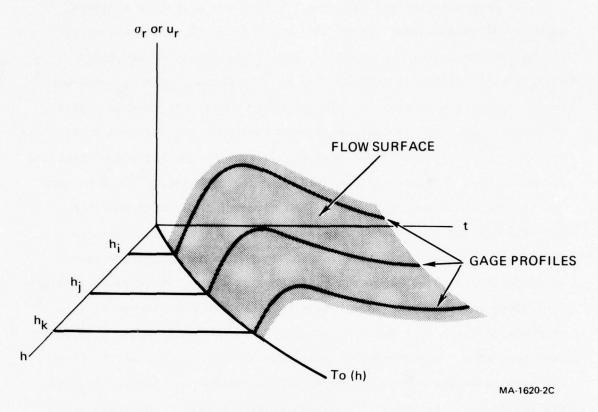


FIGURE A-1 GAGE FLOW SURFACE.

The traces on this surface provided by the gage profiles are used to approximate the surface.

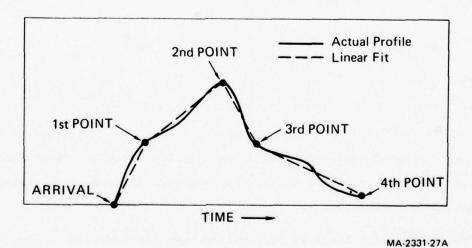


FIGURE A-2 PIECEWISE LINEAR REPRESENTATION OF GAGE RECORD.

Points shown are parameters that were selected as best characterizing the data.

The procedure for creating the two averaged gage flow surfaces consists of three steps. First, the significant flow features on each record are identified and labeled. Significant features are those clearly identifiable in the majority of the records, such as precursor foot, a plastic wave peak, a point at which decay rate changes rapidly, or simply a specific percentage of peak amplitude for a smooth featureless profile. Second, since other features present in the individual profiles are not deemed statistically significant, the labelled features on each profile are connected by straight line segments to produce piecewise linear (in time) gage record représentations as shown in Figure A-2. The third step provides interpolation between Lagrange measurements locations h, and averages the individual profiles. This is accomplished by linking the amplitude coordinates and the time coordinates at each discrete position h, for each feature, such as peak stress, with smooth functions of h. A hypothetical peak stress amplitude versus h linking is shown in Figure A-3. Of course, a time versus h linking for this feature is also necessary to complete specification of the peak stress trace on the gage flow surface. Linear or quadratic exponential functions are generally used for the h-linking:

amplitude or 
$$\begin{cases} & e^{\alpha+\beta h}, \text{ linear exponential fit} \\ & \\ & \\ time & \end{cases} = \begin{cases} & e^{\alpha+\beta h}, \text{ linear exponential fit} \\ & \\ & \\ & e^{\gamma+\delta h+\lambda h}, \text{ quadratic exponential fit} \end{cases}$$

where  $\alpha$  and  $\beta$  are constants created by the linear least squares fit, and  $\gamma$ ,  $\delta$ , and  $\lambda$  are constants created by the quadratic least squares fit. A different set  $(\alpha,\beta)$  or  $(\gamma,\delta,\lambda)$  is generated for each amplitude and each time link line.

The fitted link lines in conjunction with the piecewise linear form for gage records generate the gage flow surface representations shown schematically in Figure A-4. From this point solution of equations

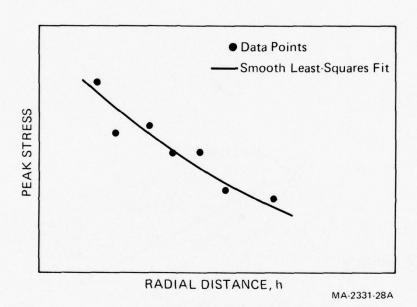


FIGURE A-3 AMPLITUDE-h LINK LINE FOR PEAK STRESS.

This is an example of a link line generated to describe the spatial variation of one of the characteristic points (in this case, peak stress) from the piecewise linear representation of the stress records.

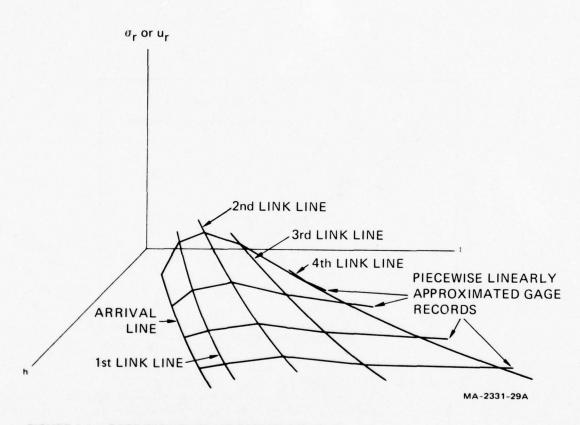


FIGURE A-4 GAGE FLOW SURFACE REPRESENTATION.

Determined from the experimental data by selecting parameters that best describe the character of the flow within the quality of the data. Note that gage records are piecewise linear and that link lines are smooth.

(A-1) through (A-6) proceeds by straightforward methods. These methods, including explanation of the path line analysis (exterior derivatives), have been described by Grady et al.  $^{7}$ 

# Appendix B

### BACKGROUND

Previous work by SRI in the in situ properties program and in related areas has been described in a series of DNA reports and is summarized here. In 1971 Keough et al. investigated the feasibility of applying the Lagrange analysis concept to radial flows and of making the in situ ground motion measurements required for the analysis. They presented the spherical flow equations and formulated an analysis for calculating specific volume from multiple Lagrange histories of radial particle velocity. This analysis was tested against an analytic solution for a specific decaying spherical shock problem and shown to be accurate. They also showed that the ytterbium piezoresistive stress gage could be modified for field use in divergent flows, and they surveyed possible radial particle velocity measurement techniques.

In 1972 Smith et al.<sup>6</sup> modified the ytterbium stress gage design and emplacement technique and obtained successful field measurements of stress in Middle Gust, Event 1. The mutual inductance particle velocity (MIPV) gage concept originally proposed by Engineering Physics Company was adopted following a survey of particle velocity measurement techniques. Two forms of this gage were built, evaluated, and shown to be feasible.

In 1973 Grady et al. <sup>7</sup> developed the technology and supporting theory for the longitudinal MIPV gage currently used in the LASS technique and performed successful field tests with it. They further improved ytterbium stress gage response, especially stretch sensitivity, by modifying the package design and emplacement procedures. High explosive proof tests of stress and particle velocity gages were conducted under conditions similar to field events, and stress measurements were

made on Middle Gust, Event III. A practical numerical IASS analysis was developed and successfully applied to a spherical elastic problem with a known analytic solution. When applied to experimental records obtained from small spherical shots in Westerly granite, the analysis gave poorer results, especially during loading; however, these results provided insight for subsequent analysis development.

In 1974 Grady et al.<sup>2</sup> developed the basic piecewise linear form of the numerical LASS analysis now used for reducing field quality stress and particle velocity records to dynamic in situ stress-strain trajectories. A rate-independent variable-modulus model was fitted to the analysis results using data from small shots in Mixed Company sandstone. This procedure demonstrated how the Lagrange analysis might be used to support ground motion calculations. The model, in conjunction with a spherical wave propagation code, produced wave profiles that compared favorably with the experimental data. The MIPV gage was developed to field instrument capability. Stress and particle velocity data were obtained for the CENSE I event, near Grand Junction, Colorado, and for four large HE tests for the Essex program at Fort Polk, Louisiana.

In late 1974, Smith et al.<sup>3</sup> refined the analysis to handle more accurately flows that exhibit rapidly changing or developing features such as precursor formation. Analysis sensitivity to internal data handling procedures was identified during reduction of records from small shots, and suggestions for improvement were offered. The stress and particle velocity records obtained in the Essex I, Phase 2, event in Fort Polk, Louisiana, added to our experience with ground motion measurements.

In 1976 Rosenberg et al. reported the first application of LASS techniques to field data. The data were obtained by appending ytterbium stress gages and mutual inductance particle velocity gages to several fully buried shots in the WES CENSE II series near Hattiesburg, Mississippi.

The radial stress-volume strain trajectory calculated at the center of the measurement interval agreed with quasi-static laboratory data in strain amplitude at peak stress, but indicated considerably stiffer local response (higher tangent modulus) for the dynamically loaded in situ material. They also reported simple two-dimensional code calculations, indicating that mutual inductance particle velocity gages fielded inside and near the bottom of radial grout columns would equilibrate to velocities acceptably close to the free field velocity even with slip and significant impedance mismatches between the grout and soil.

Rosenberg et al. also examined the accuracy of numerical methods and especially finite difference approximations used in the LASS analysis and reported that, given accurate records from 5 to 8 realistically separated gage stations, strains could be calculated to within 5% to 10% for complex flows. They concluded that further work was necessary to calculate stress differences using LASS methods but that LASS was ready for field use at appropriate sites.

At DNA's request SRI has fielded the gages developed for the in situ program, particularly the ytterbium stress gage, in several other programs during the past few years. In 1971 Smith described measurements on two 1000-pound high explosive shots at the Nevada Test Site (NTS). Subsequent ytterbium calibration work by Ginsberg et al. led Smith to replot some of the waveforms: these are included in a summary report by Jones and Green. In 1972 Smith reported measurements on another 1000-pound test at NTS, the Mine Dust high explosive test. Predictions and measurements were in generally good agreement in all of these high explosive tests and helped to establish the importance of air-filled porosity in controlling the rate of stress wave attenuation in tuff.

In 1973 Smith presented ytterbium gage measurements made on two nuclear shots, Dido Queen and Husky Ace.  $^{12}$  The records were very clean and consistent, the best that had been obtained at the time.

In 1975 Smith<sup>13</sup> reported ytterbium gage measurements made at the AFWL Hardpan test site in a series of shots designed to investigate the stress and motion fields generated under multiple loading by arrays of HE charges. The high quality, long duration records obtained clearly showed signals from individual charges. The measurements demonstrated that the first wave produced unexpectedly large alterations in the medium, resulting in significant enhancement of the amplitude of subsequent waves.

In 1976 Murri and Smith<sup>14</sup> obtained high quality, long duration stress measurements in the 0.1-1.0 GPa range in the 100-ton and 120-ton (90.7 and 109 Mg) Pre-Dice Throw Events. These measurements provided information for use in designing the 600-ton (544 Mg) Dice Throw event and made stress-time and stress-range data for the Pre-Dice Throw site material available to the ground shock community.

### Appendix C

### DIGITAL SMOOTHING OF FIELD DATA

### D. G. Falconer

## INTRODUCTION

Field measurements of stress and particle velocity histories in explosively loaded geologic materials contain experimental noise that complicates the interpretation and use of such data in Lagrange stress-strain analyses. To suppress such noise and thus improve the scientific value of the field experiments, one can smooth the gathered data by some reproducible and objective means. The simplest smoothing procedure is window averaging. Here a prescribed period, T, is established and a simple average formed about each data point:

$$\bar{v}(t) = \frac{1}{T} \int_{-T/2}^{+T/2} v(t - t') dt'$$

where v(t) represents the history being smoothed, e.g., a particle velocity record. The selected period T should be long enough to average the noise away, but short enough to preserve important physical features. A sophisticated form of this approach called low-pass window filtering was used in the present program.

Spline functions are another method of data smoothing that might be applied. For example, spline functions can be developed for the velocity and stress records, with the "knots" located at the discontinuities in the shock-wave histories. The advantages of spline functions are that they: (1) allow for some curvature in the shock-wave histories between knots, (2) provide continuous derivatives for calculating accelerations and gradients, and (3) make no pretense about an underlying model.

(Piecewise-linear approximations to the velocity and stress histories may be interpreted as a first-order spline analysis.) Two-dimensional spline functions could provide velocity and stress estimates over h-t space, thus gaining greater averaging power and eliminating the need for pathline approximations for gradient derivatives. This approach was not considered to be cost-effective in the present application.

Global modeling is another approach to the data-smoothing problem. This procedure features the same advantages as the spline functions but allows greater use of a priori knowledge and physical law. For example, it is known a priori that the stress difference becomes positive on arrival of the shock front. Similarly, physical law requires that the shock histories obey causality. Like the spline analyses, the global model of the shock histories must have "knots" between physically distinct regions such as compression and release. In addition, the selected model must have two modes: one for the velocity data and one for the stress data. Because such models (1) approach the data globally, (2) allow for a priori knowledge and physical law, and (3) simplify error assignments, they represent, in theory, a best-approach to the data-analysis problem.

### LOW-PASS FILTERING

Although window averaging is quite simple, it is far from optimum. The chief criticism of this technique is that it makes no provision for the time-variant nature of the signals and noise in velocity and stress records. Also, the window shape is uniform, rather than specially tailored for the signal and noise. If the power spectra of the expected signal and the interferring noise are known a priori at each point t in the time histories, then an optimum smoothing filter can be designed. In practice, these spectra are known only approximately, so that sub-optimal filtering must be considered.

A good low-pass filter can be designed using the following steps:

- (1) The signal history is first assigned a window width T(t) that equals, approximately, the period over which the signal is believed stationary—that is, its power spectrum remains constant.
- (2) The window shape is then prescribed by the Wiener formula:

$$W(f) = A/(1 + P_n/P_s)$$

where P(P) is the power spectrum of the signal (noise) at the temporal frequency f. Here W(f) is the Fourier transform of the window function w(t).

(3) The constant A is given by:

$$A = 1 + P_n(0)/P_s(0)$$

This requirement keeps the filtering process from lowering the general signal level.

(4) The smoothed data  $\tilde{v}(t)$  is then obtained with the following formula:

$$\bar{v}(t) = \frac{1}{T(t)} \int_{-T(t)/2}^{+T(t)/2} w(t') v(t - t') dt'$$

These steps lead to a time-variant, Wiener filter with a normalized response.

## LASS SMOOTHING

A modified version of the above procedure was used to smooth the LASS data. Because the stationary period, T(t), of the shock histories was known only crudely, a simple linear form was presumed. That is,

$$T(t) = \begin{cases} 0, t < t \\ peak \end{cases}$$

$$B(t - t_{peak}), t > t_{peak}$$

where the constant B = 0.4  $\mu$ s<sup>-1</sup>. In other words, no filtering was

carried out before the signal peak. After the signal peak, the stationary period (window width) increased linearly with time.

The filter form was presumed to have a gaussian form:

$$W(f) = \exp(-f^2/f_0^2)$$

The half-power point was defined with:

$$f_0 = 4/T$$

The averaging-window was thus decreased inversely with the averaging time, T. The filtering process was made casual by insisting that the window function w(t) be zero for  $t \le 0$ . This constraint was enforced by multiplying the window function by a unit step function h(t). The new window function, w(t)h(t), was then inverse transformed for a new (and thus casual) filter function w(t). The mean and variance of the filtered signal were then set equal to the mean and variance of the original signal to obtain the final smoothed profiles.

## Appendix D

# STRESS-STRAIN ERROR ASSIGNMENTS FOR FINITE-DIFFERENCE LAGRANGE ANALYSIS

## D. G. Falconer

#### INTRODUCTION

Field measurements of ground motion contain several types of experimental interferences. Two are particularly important: amplifier noise and position errors. Amplifier noise here refers to the total (presumably) additive, zero-mean, gaussian, random disturbances in the recorded signals. It may be caused by site inhomogeneities or many other factors. Similarly, position errors refer to additive, zero-mean, gaussian, random errors in the geometrical positions of the velocity and stress gages. The principal objective of this appendix is to assign approximate errors to stress and strain trajectories calculated by a finite-difference form of Lagrange analysis. These trajectories are derived from shockwave data recorded at various times and positions. Accordingly, the amplifer noise and position errors must be propagated from the experimental domain to the stress-strain domain.

Error assignments are made assuming a finite-difference analysis in which partial derivatives are calculated along path lines connecting corresponding features in h-t space. (Here h represents the initial gage position and t the elapsed time.) Only first-order approximations for the error assignments are attempted. Thus, minor sources of error are omitted and mathematical approximations used liberally. These conditions greatly simplify the error analysis yet give satisfactory error assignments on stress and strain.

Data smoothing may be expected to modify the assigned errors. Such smoothing might consist of low-pass filtering, spline-function analysis,

piecewise-linear approximations, or global modeling. The present analysis provides a strong basis for developing error assignments for smoothed data.

# BACKGROUND

In this discussion, t represents the elapsed time and h the initial or Lagrange gage position. Also, r(h,t), v(h,t), s(h,t), and e(h,t) represent, respectively, the position, velocity, stress, and strain at the point (h,t). The velocity and stress gages measure v(h,t) and s(h,t) at several locations,  $h_1,h_2$ , .... These measurements suffer errors with standard deviations  $\sigma_V$  and  $\sigma_S$ , respectively. In addition, survey errors  $\delta h_1$ ,  $\delta h_2$ ,  $\delta h_3$ , ... exist; these errors give the distance between the actual gage position  $h_m'$  and the assumed one  $h_m$ ,  $m=1,2,\ldots$  M.

Stress and strain profiles are obtained by looking at the spatial and temporal derivatives and integrals of the shock-wave records. The velocity and stress records are denoted, respectively, by

$$v(h_m,t_n), s(h_m,t_n)$$

where  $m=1, 2 \ldots M$ , and  $n=1, 2 \ldots N$ . The derivatives and integrals are obtained with finite-difference techniques. For example, particle position  $r(h_m, t_n)$  is calculated from the velocity samples using:

$$r(h_m, t_n) = h_m + \sum_{i=1}^{n} v(h_m, t_i) \delta t$$

where  $\delta t$  is the sampling interval and  $h_m$  is the initial particle position. Similarly, the particle acceleration (at constant h) is obtained with:

$$\frac{\partial \mathbf{v}}{\partial t}(\mathbf{h}_{m}, \mathbf{t}_{n}) = \frac{\mathbf{v}(\mathbf{h}_{m}, \mathbf{t}_{n+1}) - \mathbf{v}(\mathbf{h}_{m}, \mathbf{t}_{n})}{\delta t}$$

Finally, the velocity gradient (at constant time) is approximated by

$$\frac{\partial v}{\partial h}(h_m, t_n) = \frac{v(h_{m+1}, t_n) - v(h_m, t_n)}{\Delta h}$$

where  $\Delta h$  is the gage separation, here assumed constant.

The finite-difference procedure makes important use of the identity:

$$\frac{\partial \mathbf{v}}{\partial \mathbf{h}}\Big|_{\mathbf{t}} = \frac{\mathbf{d}\mathbf{v}}{\mathbf{d}\mathbf{h}}\Big|_{\mathbf{path}} - \frac{\partial \mathbf{v}}{\partial \mathbf{t}}\Big|_{\mathbf{h}} \frac{\Delta \mathbf{t}}{\Delta \mathbf{h}}\Big|_{\mathbf{path}}$$

When errors exist in the right-hand quantities, it is important to select a path line that minimizes the error assigned to the left-hand quantity. As discussed by Grady<sup>7</sup> and Seaman, <sup>18</sup> the path line that connects corresponding features of the gage records tends to minimize such errors. Accordingly, this path is used in what follows (see Figure D-1).

For simplicity, the following (unambiguous) notation is used:

$$\frac{\partial \mathbf{v}}{\partial \mathbf{t}} \begin{vmatrix} \mathbf{v} \\ \mathbf{h} \end{vmatrix} = \frac{\partial \mathbf{v}}{\partial \mathbf{t}} \qquad \frac{\partial \mathbf{v}}{\partial \mathbf{h}} \begin{vmatrix} \mathbf{v} \\ \mathbf{v} \end{vmatrix} = \frac{\partial \mathbf{v}}{\partial \mathbf{h}} \qquad \frac{\partial \mathbf{v}}{\partial \mathbf{h}} \begin{vmatrix} \mathbf{v} \\ \mathbf{v} \end{vmatrix} = \frac{\partial \mathbf{v}}{\partial \mathbf{h}} \qquad \frac{\partial \mathbf{v}}{\partial \mathbf{h}} \begin{vmatrix} \mathbf{v} \\ \mathbf{v} \end{vmatrix} = \frac{\partial \mathbf{v}}{\partial \mathbf{h}} \qquad \frac{\partial \mathbf{v}}{\partial \mathbf{h}} \qquad \frac{\partial \mathbf{v}}{\partial \mathbf{h}} \qquad \frac{\partial \mathbf{v}}{\partial \mathbf{h}} = \frac{\partial \mathbf{v}}{\partial \mathbf{h}} \qquad \frac{\partial \mathbf{v}}{\partial \mathbf{h}} \qquad \frac{\partial \mathbf{v}}{\partial \mathbf{h}} = \frac{\partial \mathbf{v}}{\partial \mathbf{h}} \qquad \frac{\partial \mathbf{v}}{\partial \mathbf{h}} = \frac{\partial \mathbf{v}}{\partial \mathbf{h}} \qquad \frac{\partial \mathbf{v}}{\partial \mathbf{h}} \qquad \frac{\partial \mathbf{v}}{\partial \mathbf{h}} = \frac{\partial \mathbf{v}}{\partial \mathbf{h}} \qquad \frac{\partial \mathbf{v}}{\partial \mathbf{h}} \qquad$$

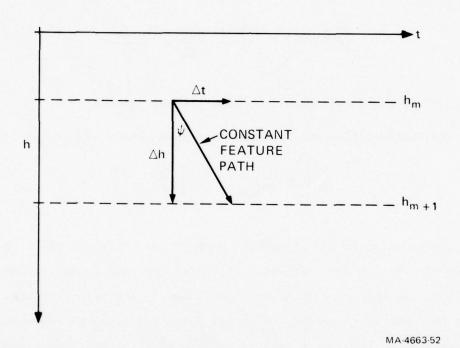


FIGURE D-1 CONSTANT-FEATURE PATH Note that  $\tan (\psi) = \Delta t/\Delta h$ .

To avoid excessively cumbersome expressions, all errors will be presumed uncorrelated, even when it is clear that they are correlated. This procedure may decrease the error assignments as much as 50%, or it may significantly increase them. In either case, a reasonable upper bound is obtained.

Finally, the errors introduced by the finite-difference analysis are ignored. Such errors can be quite significant, especially on partial derivatives across two gages, e.g.,  $\partial v/\partial h$ .

## STRAINS

The tangential, radial, and volumetric strains, are defined by

$$e_t = 1 - (r/h)$$
 $e_r = 1 - (\partial r/\partial h)$ 
 $e_v = 1 - (r/h)^2 (\partial r/\partial h)$ 

where r is given above. These quantities are estimated from the velocity data using finite-difference techniques. The errors introduced in  $e_r$ ,  $e_t$ , and  $e_v$  by amplifier and position errors are considered in turn below.

#### Tangential Strain

The tangential strain,  $e_t$ , depends linearly on the position r. Accordingly, only this quantity is considered in what follows.

Amplifier Noise. Let the amplifier noise at the gage position h at the sample time t be denoted by q(h,t). Then the position estimate will have the basic form:

$$\mathbf{r}(\mathbf{h}_{m},\mathbf{t}_{n}) = \mathbf{h}_{m} + \sum_{\mathbf{i}} \left[ v(\mathbf{h}_{m},\mathbf{t}_{\mathbf{i}}) + q(\mathbf{h}_{m},\mathbf{t}_{\mathbf{i}}) \right] \delta \mathbf{t}$$

The statistical variation in the position estimate is then given by:

$$V[r] = E[(r-\vec{r})^{2}]$$

$$= E[\{\sum q(h,t_{i}) \delta t\}^{2}]$$

$$= n \sigma_{v}^{2} \delta t^{2}$$

where  $\frac{2}{\sigma_{\mathbf{V}}}$  is the variance of the noise. The variance in the tangential strain is thus

$$V[r/h] = n\sigma_v^2 \delta t^2/h^2$$

Because the tangential strain involves an integral over the experimental data, amplifier noise has only nominal impact on the estimated value for the tangential strain.

<u>Position Errors</u>. Let  $\delta h$  equal the difference between the true gage location h' and the surveyed one h. Then the r estimate will suffer error because the velocity data taken at the position h' will be used to estimate r at h, where h' = h +  $\delta h$ . That is,

$$\mathbf{r}(\mathbf{h}, \mathbf{t_{ii}}) = \mathbf{h} + \sum_{i} \mathbf{v}(\mathbf{h}', \mathbf{t_{i}}) \delta \mathbf{t}$$

$$= \mathbf{h} + \sum_{i} \mathbf{v}(\mathbf{h} + \delta \mathbf{h}, \mathbf{t_{i}}) \delta \mathbf{t}$$

$$= \mathbf{h} + \sum_{i} \mathbf{v}(\mathbf{h}, \mathbf{t_{i}}) \delta \mathbf{t} + \sum_{i} \frac{\partial \mathbf{v} (\mathbf{h}, \mathbf{t_{i}})}{\partial \mathbf{h}} \delta \mathbf{h} \delta \mathbf{t}$$

The first two terms represent the usual finite-difference formula for the position r. The last term is an error term. The variance of this term is:

$$V[r] = E[\left(\sum_{i} \frac{\partial v}{\partial h} \delta h \delta t\right)^{2}]$$

To evaluate this expression, the summation must be writtern in terms of the measured data.

The above error assignment contains gradients with respect to h. These gradients are evaluated along a constant-feature path using the identity:

$$\frac{\partial \mathbf{v}}{\partial \mathbf{h}} = \frac{\mathbf{d}\mathbf{v}}{\mathbf{d}\mathbf{h}} - \frac{\partial \mathbf{v}}{\partial \mathbf{t}} \frac{\Delta \mathbf{t}}{\Delta \mathbf{h}}$$

The ratio  $\Delta t/\Delta h$  can be extracted directly from the experimental data. (This extraction gives  $\Delta t$ , since  $\Delta h$  comes from the experimental layout.)

The particle acceleration is obtained by differentiating the velocity record:

$$\frac{\partial \mathbf{v}}{\partial \mathbf{t}} = \frac{\mathbf{v} (\mathbf{h}_{m}, \mathbf{t}_{n+1}) - \mathbf{v} (\mathbf{h}_{m}, \mathbf{t}_{n})}{\delta \mathbf{t}}$$

Similarly, the total derivative is obtained by differentiating across two velocity records:

$$\frac{dv}{dh} = \frac{v(h_{m+1}, t_n + \Delta t) - v(h_m, t_n)}{\Delta h}$$

The last three expressions allow evaluation of the variance in the r-estimate due to position errors.

Because particle velocity varies slowly with h, gage position errors will have only nominal impact on the tangential strain.

## Radial Strain

The radial strain,  $e_r$ , depends linearly on the partial derivative  $\partial r/\partial h$ . Accordingly, only this quantity is considered in what follows:

Amplifier Noise. The position gradient is obtained from the constant-feature path using the identity:

$$\frac{\partial \mathbf{r}}{\partial \mathbf{h}} = \frac{\mathbf{dh}}{\mathbf{dh}} - \frac{\partial \mathbf{r}}{\partial \mathbf{t}} \frac{\Delta \mathbf{t}}{\Delta \mathbf{h}}$$

The particle velocity  $\partial r/\partial t$  at constant h is an experimental measurement  $v(h_m,t_n)$ , with standard error  $\sigma_v$ . The total derivative, on the other hand, depends on two velocity records:

$$\frac{d\mathbf{r}}{dh} = \frac{\mathbf{r}(h_{m+1}, t_n + \Delta t) - \mathbf{r}(h_m, t_n)}{\wedge h}$$

The standard error in the r-estimate was obtained above in the discussion of amplifier noise for tangential strain.

The gage records are, of course, statistically independent. Also, we are ignoring incidental correlations among quantities derived from the same data set, e.g.,  $r(h_m, t_n)$  and  $v(h_m, t_n)$ . The variance in  $\partial r/\partial h$  then takes the uncorrelated form:

$$V[\partial r/\partial h] = 2V[r]/\Delta h^2 + (\partial_v \Delta t/\Delta h)^2$$

(The V[r] was obtained above.) Generally speaking, the second term dominates the first. Since  $\Delta t/\Delta h \approx 1$ , the noise in  $\partial r/\partial h$  is comparable to that in the v measurements.

Position Errors. The position error will cause a corresponding error in the partial derivative  $\partial r/\partial h$ . In particular,

$$\frac{\partial \mathbf{r}}{\partial t} = \mathbf{v}(\mathbf{h}', \mathbf{t}_n) = \mathbf{v}(\mathbf{h}, \mathbf{t}_n) + \frac{\partial \mathbf{v}}{\partial \mathbf{h}} \delta \mathbf{h}$$

The partial derivative  $\partial v/\partial h$  was estimated in the discussion of tangential strains above.

Position errors Oh also propagate to the total derivative.

$$\frac{d\mathbf{r}}{dh} = \frac{\mathbf{r}(h'_{m+1}, t_n + \Delta t) - \mathbf{r}(h'_m, t_n)}{\Delta h}$$

$$= \frac{\mathbf{r}(h_{m+1}, t_n + \Delta t) - \mathbf{r}(h_m, t_n)}{\Delta h}$$

$$+ \frac{\partial \mathbf{r}(h_{m+1}, t_n + \Delta t)}{\partial h} \frac{\delta h_{m+1}}{\Delta h}$$

$$- \frac{\partial \mathbf{r}(h_m, t_n)}{\partial h} \frac{\delta h_m}{\Delta h}$$

The last two terms represent the first-order impact of position errors on the total derivative. These errors are statistically independent, since  $\delta h_m$  +  $_1$  and  $\delta h_m$  are independent.

The variance in  $\partial r/\partial h$  due to position errors thus takes the form:

$$V\left[\frac{\partial \mathbf{r}}{\partial \mathbf{h}}\right] = 2\left(\frac{\partial \mathbf{r}}{\partial \mathbf{h}} \frac{\delta \mathbf{h}}{\Delta \mathbf{h}}\right)^2 + \left(\frac{\partial \mathbf{v}}{\partial \mathbf{h}} \frac{\Delta \mathbf{t}}{\Delta \mathbf{h}} \delta \mathbf{h}\right)^2$$

In practice, the second term dominates the first since r is an integrated quantity, while v is not.

# Volumetric Strain

The volumetric strain,  $e_v$ , depends quadratically on the position r and linearly on the partial derivative  $\partial r/\partial h$ . Thus, the total error

consists of two terms:

$$\Delta \left(\frac{\mathbf{r}^2}{\mathbf{h}^2} \frac{\partial \mathbf{r}}{\partial \mathbf{h}}\right) = \left(\frac{\mathbf{r}^2}{\mathbf{h}^2}\right) \Delta \frac{\partial \mathbf{r}}{\partial \mathbf{h}} + \frac{2\mathbf{r}}{\mathbf{h}} \frac{\partial \mathbf{r}}{\partial \mathbf{h}} \Delta(\mathbf{r})$$

Compared with  $\partial r/\partial h$ , the errors in r are quite small. Thus, we concentrate on the first term in what follows.

Amplifier Noise. The amplifier noise affects the 2r/2h estimate and thus also the volumetric strain. The variance in the volumetric strain is, thus, approximately

$$V\left[\frac{\mathbf{r}^2}{h^2} \frac{\partial \mathbf{r}}{\partial h}\right] = \frac{\mathbf{r}^2}{h^2} V\left[\frac{\partial \mathbf{r}}{\partial h}\right]$$

where V[3r/3h] is given above in the discussion of radial strain.

<u>Position Errors</u>. Position errors affect the  $\partial v/\partial h$  estimate and hence also the volumetric strain. In particular,

$$V\left[\frac{\mathbf{r}^2}{h^2} \frac{\partial \mathbf{r}}{\partial h}\right] = \frac{\mathbf{r}^2}{h^2} V\left[\frac{\partial \mathbf{r}}{\partial h}\right]$$

The variance  $V[\partial v/\partial h]$  was derived above in the discussion of radial strain.

## STRESS DIFFERENCE

The stress difference  $\Phi$  depends both on the velocity and stress records. In addition, this quantity is obtained as a small difference between two large quantities. That is,  $\Phi$  has the approximate form:

$$\Phi = \frac{3}{h} \left( \frac{9 t}{9 t} + \frac{9 t}{9 s} \right)$$

(The two partial derivatives have opposite signs.) Typically, the

magnitude of  $\phi$  is 10% of either  $\partial v/\partial t$  or  $\partial s/\partial h$ . Accordingly, small errors in either partial derivative lead to large errors in the stress difference. The situation is further aggravated by the fact that both partials are obtained as derivatives of the experimental data, a calculational process that also magnifies noise.

## Amplifier Noise

The amplifier noise in the velocity gages leads to a noisy acceleration estimate. That is,

$$\frac{\partial \mathbf{t}}{\partial \mathbf{t}} = \frac{\mathbf{v}(\mathbf{h}, \mathbf{t}_{n+1}) - \mathbf{v}(\mathbf{h}, \mathbf{t}_{n})}{\delta \mathbf{t}}$$

has a variance of the form:

$$v\left[\frac{\partial v}{\partial t}\right] = \frac{2\sigma_v^2}{\delta t^2}$$

For small  $\delta t$ , this variance becomes quite large. Conversely, large  $\delta t$  reduces the variance, but also increases the finite-difference errors.

The stress gradiant is obtained with the path-line technique:

$$\frac{\partial s}{\partial h} = \frac{ds}{dh} - \frac{\partial s}{\partial t} \frac{\Delta t}{\Delta h}$$

The variance in the first term,

$$\frac{ds}{dh} = \frac{s(h_{m+1}, t_n + \Delta t) - s(h_m, t_n)}{\Delta h}$$

is just

$$v\left[\frac{ds}{dh}\right] = \frac{2\sigma_s^2}{\Delta h^2}$$

Similarly, the second-term variance is

$$V\left[\frac{\partial s}{\partial t} \frac{\Delta t}{\Delta h}\right] = \frac{2\sigma_{s}^{2}}{\delta t^{2}} \left(\frac{\Delta t}{\Delta h}\right)^{2}$$

The total variance due to amplifier noise follows by addition:

$$V[\Phi] = \left(\frac{h}{2}\right)^2 \left[\frac{2\sigma_v^2}{\delta t^2} + \frac{2\sigma_s^2}{\Delta h^2} + \frac{2\sigma_s^2}{\delta t^2} \left(\frac{\Delta t}{\Delta h}\right)^2\right]$$

We are again ignoring minor correlations that occur, for example, between ds/dh and  $\partial s/\partial t$ . In practice,  $\Delta t \approx \Delta h \gg \delta t$ , so that the first and third terms dominate the second.

## Position Errors

Position errors  $\delta h$  affect the partial derivatives  $\partial s/\partial h$  used to calculate the stress difference  $\Phi$ . The particle acceleration  $\partial v/\partial t$  will be in error according to

$$\frac{\partial \mathbf{v}}{\partial \mathbf{t}} = \frac{\mathbf{v}(\mathbf{h}'_{m}, \mathbf{t}_{n+1}) - \mathbf{v}(\mathbf{h}'_{m}, \mathbf{t}_{n})}{\delta \mathbf{t}}$$

$$= \mathbf{v}(\mathbf{h}_{m}, \mathbf{t}_{n+1}) - \mathbf{v}(\mathbf{h}_{m}, \mathbf{t}_{n})$$

$$\frac{\delta \mathbf{t}}{\delta \mathbf{t}}$$

$$+ \frac{\partial \mathbf{v}(\mathbf{h}_{m}, \mathbf{t}_{n+1})}{\partial \mathbf{h}} \frac{\delta \mathbf{h}_{m}}{\delta \mathbf{t}} - \frac{\partial \mathbf{v}(\mathbf{h}_{m}, \mathbf{t}_{n})}{\partial \mathbf{h}} \frac{\delta \mathbf{h}_{m}}{\delta \mathbf{t}}$$

The last two terms represent the induced errors; they can be written as  $(\frac{2}{2}v/\partial h\partial t)\delta h$ . The variance in the acceleration estimate is thus

$$V\left|\frac{\partial V}{\partial t}\right| = \left(\frac{\partial^2 V}{\partial h \partial t} \delta h\right)^2$$

The second derivative can be estimated with the formula given in Appendix E.

The position errors  $\delta h$  also affect the stress gradient:

$$\frac{\partial \mathbf{s}}{\partial \mathbf{h}} = \frac{\mathbf{d}\mathbf{h}}{\mathbf{d}\mathbf{h}} - \frac{\partial \mathbf{t}}{\partial \mathbf{t}} \frac{\Delta \mathbf{t}}{\Delta \mathbf{h}}$$

By symmetry, the variance in  $\partial s/\partial t$  is given by:

$$V\left[\frac{\partial s}{\partial t}\right] = \left(\frac{\partial^2 s}{\partial h \partial t} \delta h\right)^2$$

The second partial is obtained by the formula:

$$\begin{split} \frac{\partial^{2} v}{\partial t \partial h} &= \frac{\partial}{\partial h} \left[ \frac{\partial v}{\partial t} \right] \\ &= \frac{d}{dh} \left[ \frac{\partial v}{\partial t} \right] - \frac{\partial}{\partial t} \left[ \frac{\partial v}{\partial t} \right] \frac{\Delta t}{\Delta h} \\ &= \left\{ \frac{v \left( h_{m+1}, t_{n+1} + \Delta t \right) - v \left( h_{m+1}, t_{n} + \Delta t \right)}{\delta t \Delta h} \right. \\ &- \frac{v \left( h_{m}, t_{n+1} \right) - v \left( h_{m}, t_{n} \right)}{\delta t \Delta t} \right\} \\ &- \left\{ \frac{v \left( h_{m}, t_{n+1} \right) - v \left( h_{m}, t_{n} + \Delta t \right)}{\delta t \Delta t} \right. \\ &- \frac{v \left( h_{m}, t_{n+1} \right) - v \left( h_{m}, t_{n} \right)}{\delta t \Delta t} \right\} \end{split}$$

The total derivative has the form:

$$\begin{split} \frac{\mathrm{ds}}{\mathrm{dh}} &= \frac{\mathbf{s}(h'_{m+1}, t_n + \Delta t) - \mathbf{s}(h', t_n)}{\Delta h} \\ &= \frac{\mathbf{s}(h_{m+1}, t_n + \Delta t) - \mathbf{s}(h_m, t_n)}{\Delta h} \\ &+ \frac{\partial \mathbf{s}}{\partial h} \delta h_{m+1} - \frac{\partial \mathbf{s}}{\partial h} \delta h_m \end{split}$$

Here the two  $\delta h$  are uncorrelated. The total variance in ds/dh is thus

$$V\left[\frac{ds}{dh}\right] = 2\left(\frac{\partial s}{\partial h} \delta h\right)^2$$

where ds/dh is calculated in the usual way.

The total variance in the stress difference is thus

$$V[\Phi] = \left(\frac{h}{2}\right)^{2} \left[ \left(\frac{\partial^{2} v}{\partial h \partial t} \delta h\right)^{2} + 2 \left(\frac{\partial s}{\partial h} \delta h\right)^{2} + \left(\frac{\partial^{2} s}{\partial h \partial t} \frac{\Delta t}{\Delta h} \delta h\right)^{2} \right]$$

In many instances, the second derivative will prove mild, thus allowing the second term to dominate the error assignment.

#### Appendix E

# STRESS-STRAIN ERROR ASSIGNMENTS FOR GLOBAL LAGRANGE ANALYSIS

#### D. G. Falconer

#### INTRODUCTION

Global Lagrange analysis of shock-wave field data offers several advantages over finite-difference techniques. In particular, global analyses:

- Reduce the impact of random amplifier noise and gage position errors by systematically averaging (smoothing) the experimental data.
- Allow enforcement of known physical constraints (e.g., causality) during the fitting effort.

The chief purpose of this appendix is to develop error assignments for the stress and strain trajectories calculated by the global Lagrange analysis.

#### BACKGROUND

Shock-wave experiments generate velocity  $v(h_m, t_n)$  and stress  $s(h_m, t_n)$  data at various gage locations  $h_m, m=1, 2, 3 \ldots M$ . Each of these may be digitized at regular times  $t_n, n=1, 2, 3 \ldots N$ . In a global fitting procedure, these space-time profiles are used to determine a best set of model parameters  $a_j, j=1, 2, 3 \ldots R$ . In particular, the fitting procedure attempts to minimize the chi-square error between the experimental values and model function f,

$$f = f(h,t,k; a_j)$$

Here k = 1 for velocity data, and k = 2 for stress data.

The chi-square error has the basic form:

$$x^{2} = \sum \left[f(h_{m}, t_{n}, 1; a_{j}) - v(h_{m}, t_{n})\right]^{2} / \sigma_{v}^{2}$$
  
+  $\sum \left[f(h_{m}, t_{n}, 2; a_{j}) - s(h_{m}, t_{n})\right]^{2} / \sigma_{s}^{2}$ 

In practice, the standard errors in  $\,v\,$  and  $\,s\,$  may also depend on position and time, that is,

$$\sigma_{v} = \sigma_{v}(h_{m}, t_{n})$$

$$\sigma_{s} = \sigma_{s}(h_{m}, t_{n})$$

However, adjacent measurements, i.e., at  $\binom{h}{m}$ , t and  $\binom{h}{m}$ , t are presumed uncorrelated.

The chi-square fitting algorithm minimizes chi-square by picking a best set of numerical values for the parameters  $a_j$ . During the fitting effort, the computer algorithm also obtains an error covariance matrix for the parameters  $a_j$ . This matrix

$$V[a] = E[\delta a_i \delta a_j] = [A_{i,j}],$$

gives the variances  $\begin{pmatrix} A \\ ii \end{pmatrix}$  and correlations  $\begin{pmatrix} A \\ ij \end{pmatrix}$  in the fitted values  $a_j$ . (Note that  $A_i$  is a single matrix element, not an algebraic product.)

Once a best fit is obtained, the function f is used to deduce stress and strain profiles. In particular, the following quantities are of interest:

$$\begin{array}{ll} \mathbf{e}_{\,\mathbf{t}} = \mathbf{1} - \mathbf{r}/h & \text{tangential strain} \\ \\ \mathbf{e}_{\,\mathbf{r}} = \mathbf{1} - \partial \mathbf{r}/\partial h & \text{radial strain} \\ \\ \mathbf{e}_{\,\mathbf{v}} = \mathbf{1} - \left(\mathbf{r}/h\right)^2 \left(\partial \mathbf{r}/\partial h\right) & \text{volume strain} \\ \\ \Phi \approx \frac{h}{2} \left(\frac{\partial \mathbf{v}}{\partial \mathbf{t}} + \frac{\partial \mathbf{s}}{\partial h}\right) & \text{stress difference} \\ \\ \mathbf{r}(\mathbf{h},\mathbf{t}) = \mathbf{h} + \int \mathbf{v}(\mathbf{h},\mathbf{t}') \mathrm{d}\mathbf{t}' & \text{particle position} \end{array}$$

(The derivative notation used above is explained in Appendix D.) Accordingly, the principal objective of this appendix is to use the errors assigned to the parameters  $\mathbf{a}_{\mathbf{j}}$  to develop errors for the stress and strain quantities.

STRAINS

For simplicity, we write

$$f_v = f(h,t,1;a_j)$$

$$f_s = f(h,t,2;a_j)$$

Strain estimates, of course, make use of only  $f_v$ .

For definiteness, we assume the following forms for f and f:

$$f_v = (a_1^x + a_2^x^2 + a_3^x^3)(1 + a_4^h + a_5^h^2)$$

$$f_s = (a_6 x + a_7 x^2 + a_8 x^3)(1 + a_4 h + a_5 h^2)$$

Here x represents the elapsed time since shock arrival at the gage position h:

$$x = t + a_9^h$$

where  $a_9$  is always a negative number. This nine-parameter model meets causality if  $f_v = f_s = 0$  for x < 0.

The particle position r(h,t) is used for both the tangential and radial strains. It has the explicit form:

$$r(h,t) = h + \int_{0}^{t} f_{v}(h,t')dt'$$

$$= h + (a_{1} \frac{x^{2}}{2} + a_{2} \frac{x^{3}}{3} + a_{4} \frac{x^{4}}{4})(1 + a_{4}h + a_{5}h^{2})$$

Small variations  $\delta a_{\ j}$  in the fitted parameters produce a small variation  $\delta r$  in the position estimate:

$$\delta \mathbf{r} = \sum \frac{\partial \mathbf{r}}{\partial \mathbf{a}_{j}} \delta \mathbf{a}_{j}$$

$$= (\frac{x^{2}}{2} \delta \mathbf{a}_{1} + \frac{x^{3}}{3} \delta \mathbf{a}_{2} + \frac{x^{4}}{4} \delta \mathbf{a}_{3}) (1 + \mathbf{a}_{4} \mathbf{h} + \mathbf{a}_{5} \mathbf{h}^{2})$$

$$+ (\mathbf{a}_{1} \frac{x^{2}}{2} + \mathbf{a}_{2} \frac{x^{3}}{3} + \mathbf{a}_{3} \frac{x^{4}}{4}) (\mathbf{h} \delta \mathbf{a}_{4} + \mathbf{h}^{2} \delta \mathbf{a}_{5})$$

The variance in the position estimate is thus given by;

$$V[r] = \sum_{i,j} \frac{\partial r}{\partial a_i} \frac{\partial r}{\partial a_j} A_{i,j}$$

where the quantity  $\mathbf{A}_{i,j}$  comes from the fitting program.

## Tangential Strain

The tangential strain,  $\mathbf{e}_{\,\mathbf{t}},$  depends linearly on the position r. Thus, the assigned error follows readily:

$$V[e_{t}] = V[r]/h^{2}$$

# Radial Strain

The radial strain,  $\mathbf{e_r}$  , depends linearly on the partial derivative  $\partial \mathbf{r}/\partial h$  . According to our model:

$$\frac{\partial \mathbf{r}}{\partial \mathbf{h}} = 1 + (\mathbf{a}_1 \frac{\mathbf{x}^2}{2} + \mathbf{a}_2 \frac{\mathbf{x}^3}{3} + \mathbf{a}_3 \frac{\mathbf{x}^4}{4}) (\mathbf{a}_4 + 2\mathbf{a}_5 \mathbf{h})$$

$$+ (\mathbf{a}_1 \mathbf{x} + \mathbf{a}_2 \mathbf{x}^2 + \mathbf{a}_3 \mathbf{x}^3) \mathbf{a}_9 (1 + \mathbf{a}_4 \mathbf{h} + \mathbf{a}_5 \mathbf{h}^2)$$

Small changes  $\delta a_{\ j}$  thus produce the following change in the partial derivative:

$$\delta \left( \frac{\partial \mathbf{r}}{\partial \mathbf{h}} \right) = \sum_{\mathbf{j}} \frac{\partial^2 \mathbf{r}}{\partial \mathbf{a}_{\mathbf{j}} \partial \mathbf{h}} \delta \mathbf{a}_{\mathbf{j}}$$

The variance in  $\partial r/\partial h$  and hence also e thus has the form:

$$V[e_r] = \sum_{i,j} \frac{\partial^2 r}{\partial a_i \partial r} \frac{\partial^2 r}{\partial a_j \partial h} A_{i,j}$$

where A obtains during data fitting.

# Volumetric Strain

The volumetric strain, e  $_{\rm V}$  , depends quadratically on r and linearly on  $\partial r/\partial h$  . Small changes in these quantities lead to the following changes in e : v

$$\delta e_{v} = -\frac{r^{2}}{h^{2}} \delta \left(\frac{\partial r}{\partial h}\right) - \frac{2r}{h^{2}} \frac{\partial r}{\partial h} \delta r$$

$$= -\frac{r^{2}}{h^{2}} \sum \frac{\partial^{2} r}{\partial a_{j} \partial h} \delta a_{j} - \frac{2r}{h^{2}} \frac{\partial r}{\partial h} \sum \frac{\partial r}{\partial a_{j}} \delta a_{j}$$

$$= -\frac{r}{h^{2}} \sum_{j} \left[ r \frac{\partial^{2} r}{\partial a_{j} \partial h} + 2 \frac{\partial r}{\partial h} \frac{\partial r}{\partial a_{j}} \right] \delta a_{j}$$

where we have propagated through to the parameter errors. The variance in volumetric strain is thus:

$$V[\epsilon_{v}] = \frac{r^{2}}{h^{4}} \sum_{i,j}^{\Sigma} [\ldots]_{i} [\ldots]_{j} A_{i,j}$$

where bracket is written out just above. The respective partial derivatives are specified above and in the discussion of radial strain.

STRESS

The stress difference  $\Phi$  depends linearly on  $\partial v/\partial t$  and  $\partial s/\partial h$ . The particle acceleration depends on the fitted parameters in the following way

$$\frac{\partial \mathbf{v}}{\partial \mathbf{t}} = \frac{\partial \mathbf{f}}{\partial \mathbf{t}}$$

Small changes in the fitted parameters thus lead to:

$$\delta \left( \frac{\partial \mathbf{v}}{\partial \mathbf{t}} \right) = \Sigma \frac{\partial^2 \mathbf{f}}{\partial \mathbf{a_j} \partial \mathbf{t}} \delta \mathbf{a_j}$$

Similarly, the stress gradient has the following form:

$$\frac{\partial \mathbf{s}}{\partial \mathbf{h}} = \frac{\partial \mathbf{f}}{\partial \mathbf{h}}$$

Small changes in a thus produce the following changes in the stress gradient:

$$\delta \left( \frac{\partial \mathbf{s}}{\partial \mathbf{h}} \right) = \Sigma \frac{\partial^2 \mathbf{f}_{\mathbf{s}}}{\partial \mathbf{a}_{\mathbf{j}} \partial \mathbf{h}} \partial \mathbf{a}_{\mathbf{j}}$$

The above expression is messy, but easy for a digital computer.

Small changes in the fitted parameters thus impact the stress difference in the following way:

$$\Phi = \frac{h}{2} \left[ \delta \left( \frac{\partial v}{\partial t} \right) + \delta \left( \frac{\partial s}{\partial h} \right) \right]$$
$$= \frac{h}{2} \Sigma \left[ \frac{\partial^2 v}{\partial a_j \partial t} + \frac{\partial^2 s}{\partial a_j \partial h} \right] \delta a_j$$

The variance in the stress difference thus takes the basic form:

$$V[\Phi] = \left(\frac{h}{2}\right)^2 \sum_{i,j} \left[ \dots \right]_i \left[ \dots \right]_j A_{i,j}$$

OTHER MODELS

Other models for the experimental data are handled in a completely analogous way. One such model is the following:

$$f_{v} = \left[a_{1}^{x} + a_{2}^{x^{2}} + a_{3}^{x^{3}}\right] \exp(a_{4}^{x})/(h+1)^{a_{5}}$$

$$f_{s} = \left[a_{6}^{x} + a_{7}^{x^{2}} + a_{8}^{x^{3}}\right] \exp((a_{4}^{x})/(h+1)^{a_{5}}$$

where

$$x = t + a_9^h + a_{10}^h^2$$

The above formulas allow for exponential release, power-law amplitude loss, and nonuniform propagation speeds.

Note that global fitting avoids the need for path-line derivatives to evaluate the gradients  $\partial r/\partial h$  and  $\partial s/\partial h$ .

#### Appendix F

# STRESS-STRAIN ERROR ASSIGNMENTS FOR PIECEWISE-LINEAR LAGRANGE ANALYSIS

#### D. G. Falconer

## INTRODUCTION

Previously in this program we have extracted stress and strain trajectories from field data using the piecewise-linear Lagrange analysis (Appendix A). This analysis consists of the following steps:

- (1) The key features of each velocity and stress history are identified, located, and measured. (Both time and magnitude errors exist with this procedure.)
- (2) Corresponding features on the several velocity and several stress records are then fit with exponential-type functions F (h) and G (h), respectively.  $F_n$  (h) gives the particle velocity associated with the n feature at the gage position h, and G (h) gives the stress level associated with the n feature at the gage position h.
- (3) Similarly functions T (h) are fitted to the times at which the n feature occurs at the gage position h. The functions
  F, G, T provide continuous estimates of particle velocity, n n n the stress level, and occurrence time of the n feature.

  Velocities and stresses between the key features are interpolated linearly using F and G.

The principal objective of this appendix is to develop error assignments for the strains and stresses derived from the experimental data using the piecewise-linear Lagrange analysis. Mathematical approximations are used liberally and correlated errors are properly accounted for.

#### BA CKGROUND

Let the gage positions be denoted by  $h_m$ ,  $m=1, 2, \ldots M$ , and the occurrence time of the n feature be denoted by  $t_n$ . Thus, following step (1) above, the velocity and stress data are of the form:

$$v(h_m,t_n)$$
,  $s(h_m,t_n)$ 

The standard errors in the velocity and stress measurements are denoted by  $\sigma_v$  and  $\sigma_s$ , respectively. Also, the standard errors in the gage position and occurrence time are denoted by  $\sigma_h$  and  $\sigma_t$ , respectively.

The fitting step (2) defines the parameterized functions  $F_n(h, a^n_i)$  and  $G_n(h, b^n_i)$ , where  $a^n_i$  and  $b^n_i$  are the fitted parameters for the  $n^n$  features. During fitting, error covariance matrices for the  $a^n_i$  and  $b^n_i$  are developed. For convenience, these matrices are written in the following form:

$$V[a^n] = E[\delta a_i^n \delta a_j^n] = [A_{i,j}^n]$$

$$V[b^{n}] = E[\delta b_{i}^{n} \delta b_{j}^{n}] = [B_{i,j}^{n}]$$

(Here  $A^n_{ij}$  and  $B^n_{ij}$  are matrix elements (numbers), not algebraic products.) The diagonal elements represent the variances in the fitted parameters; the off-diagonal ones represent the convariance between the fitted parameters.

The error matrices  $V[a^n]$  and  $V[b^n]$  depend on the standard deviations  $\sigma_v$ ,  $\sigma_s$ , and  $\sigma_h$ . The error represented by  $\sigma_v$  is an amplitude error and thus handled in the usual way during fitting. The error represented by  $\sigma_h$ , however, must be propagated to look like an amplitude error. An easy way to accomplish this task is to first fit F(t,a) to the data set assuming  $\sigma_h = 0$ , and then use the fitting function in the following propagation formula:

$$\Delta F_{n} = \frac{\partial F_{n}}{\partial h} \Delta h$$

The errors represented by  $\sigma_{\rm v}$  and  $\sigma_{\rm h}$  are, of course incoherent, so that their variances add:

$$\sigma^2 = \sigma_v^2 + \left(\frac{\partial F}{\partial h}\right)^2 \sigma_h^2$$

The fitting process is then repeated, using  $\sigma^2$  in place of  $\sigma_v^2$ . A similar approach is taken with fitting  $G_n(h,b_i^n)$ . In practice,  $\sigma_v$ ,  $\sigma_s$ , and  $\sigma_h$  may depend on the gage position  $h_m$  and the feature number n.

Under step (3), the function  $T_n(h,c_i^n)$  is fit to the occurrence times of the  $n^{th}$  feature. This fit suffers uncertainty  $(\sigma_t)$  in the time estimate and uncertainty  $(\sigma_h)$  in the position estimate. The first uncertainty, being an amplitude error, is handled in the usual way during fitting. The second uncertainty is accounted for following an initial fit with  $\sigma_h = 0$ . The fitted function is then used to derive a total amplitude error:

$$\sigma^2 = \sigma_t^2 + \left(\frac{\partial T_n}{\partial h}\right)^2 \sigma_h^2$$

In practice, both  $\sigma_t$  and  $\sigma_h$  may depend on gage position  $h_m$  and the feature number n. In other words:

$$\sigma_t = \sigma_t(m,n)$$

$$\sigma_h = \sigma_h(m,n)$$

This dependence is readily handled by chi-square fitting routines.

## STRAINS

The tangential, radial, and volumeric strains have the following forms:

$$e_{t} = 1 - r/h$$

$$e_{r} = 1 - \partial r/\partial h$$

$$e_{v} = 1 - (r/h)^{2} (\partial r/\partial h)$$

The error assignments for these quantities are developed below.

# Tangential Strain

The main ingredient of the tangential strain,  $\epsilon_{\rm t}$ , is the particle position r. This quantity obtains in the usual way by integrating the smoothed (i.e., fitted) velocity records:

$$r(h,t) = h + \int_{0}^{t} v(h,t')dt'$$

$$= h + \frac{1}{2} \sum_{n=1}^{\infty} \left[ F_{n}(h,a_{i}^{n}) - F_{n-1}(h,a_{i}^{n-1}) \right] (t_{n} - t_{n-1})$$

$$= h + \sum_{n=1}^{\infty} F_{n}(h,a_{i}^{n}) \Delta^{2} t_{n}$$

We have introduced the notation

$$\Delta^2 t_n = 1/3 (2t_n - t_{n+1} - t_{n-1})$$

The occurrence times,  $t_n$ , are taken from the fitted values, that is,  $t_n(h) = T_n(h, c_i^n)$ . The final time, t, is interpolated if it falls between two key features.

Small changes  $\delta a \frac{n}{i}$  in the fitted parameters then lead to the following changes in the particle position:

$$\Delta \mathbf{r} = \sum_{n,i} \frac{\partial F_n}{\partial a_i} \Delta^2 t_n \, \delta a_i^n$$

(For simplicity, we have presumed that temporal errors are small.)

The variance in the r-estimate follows immediately

$$V[r] = E \left[ \sum_{\substack{n,m \ i,j}} \frac{\partial F_{n}}{\partial a_{i}^{n}} \Delta^{2} t_{n} \frac{\partial F_{m}}{\partial a_{j}^{m}} \Delta^{2} t_{m} \delta a_{i}^{n} \delta a_{j}^{m} \right]$$

$$= \sum_{\substack{n,i,j}} \frac{\partial F_{n}}{\partial a_{i}^{n}} \frac{\partial F_{n}}{\partial a_{j}^{n}} (\Delta^{2} t_{n})^{2} A_{ij}^{n}$$

(The variations  $\delta a_i^n$  and  $\delta a_j^m$  are presumed statistically independent unless n=m.) The above formula is readily handled with a digital computer.

## Radial Strain

The main constituent of the radial strain, e , is the partial derivative  $\partial r/\partial h$ . This quantity obtains from the r-estimate:

$$\frac{\partial \mathbf{r}}{\partial \mathbf{h}} = 1 + \sum_{\mathbf{n}} \frac{\partial \mathbf{F}_{\mathbf{n}}}{\partial \mathbf{h}} \Delta^{2} \mathbf{t}_{\mathbf{n}}$$

Small variations in  $\partial F_n/\partial h$  thus lead to the following change in the partial derivative:

$$\Delta \left( \frac{\partial \mathbf{r}}{\partial \mathbf{h}} \right) = \sum_{\mathbf{n}} \Delta \left( \frac{\partial F_{\mathbf{n}}}{\partial \mathbf{h}} \right) \Delta^{2} \mathbf{t}_{\mathbf{n}}$$

For simplicity we presumed that the various  $\Delta(\partial F_n/\partial h)$  are statistically independent. In this case the variance follows directly:

$$V\left[\frac{\partial \mathbf{r}}{\partial h}\right] = \sum_{n,m} (\Delta^2 t_n) E\left[\frac{\partial F_n}{\partial h} \frac{\partial F_m}{\partial h}\right]$$

Thus, we need the expectation of the various products ( $\partial F_n/\partial h$ ) ( $\partial F_m/\partial h$ ).

The derivative  $\partial F_n/\partial h$  obtains through the path-line formula:

$$\frac{\partial F_n}{\partial h} = \frac{dF_n}{dh} - \frac{\partial F_n}{\partial t} \frac{dt}{dh}$$

The ratio dt/dh follows directly from the fitted times  $T_n(h,c_i^n)$ :

$$\frac{dt}{dh} = \frac{dT_n(h, c_i^n)}{dh} = tan (\psi_n)$$

Similarly, the total derivative  ${\rm dF}_n/{\rm dh}$  follows immediately from the fitted velocity  ${\rm F}_n$ . The time derivative is obtained by interpolating between key features.

$$\frac{\partial F}{\partial t} = \frac{F_{n+1}(h, a_i^{n+1}) - F_n(h, a_i^n)}{T_{n+1}(h, c_i^{n+1}) - T_n(h, c_i^n)}$$

In what follows the denominator is denoted by  $\Delta t_n$ .

We presume that the principal source of strain error results from  $F_n$ , rather than from  $T_n$ . In this case small changes in the parameters  $a_i^n$  lead to the following changes in the partial derivative:

$$\Delta \left( \frac{\partial F_{n}}{\partial h} \right) = \sum_{i} \left[ \frac{\partial}{\partial a_{i}^{n}} \left( \frac{dF_{n}}{dh} \right) \delta a_{i}^{n} + \left( \frac{\partial F_{n+1}}{\partial a_{i}^{n+1}} \frac{\delta a_{i}^{n+1}}{\Delta t_{n}} - \frac{\partial F_{n}}{\partial a_{i}^{n}} \frac{\delta a_{i}^{n}}{\Delta t_{n}} \right) \tan \left( \psi_{n} \right) \right]$$

The expectation of the cross partials is thus:

$$E\left[\frac{\partial F_{n}}{\partial h} \frac{\partial F_{m}}{\partial h}\right] = E\left[\sum_{i,j} \left\{ [n,i] [m,j] \right\} \right]$$

where the bracketed quantities abbreviate the bracketed quantities in the penultimate expression.

The variations  $\delta a_i^n$  and  $\delta a_j^m$  are statistically independent unless m=n . If n=m , the last expression becomes:

$$E\left[\frac{\partial F_{n}}{\partial h}\frac{\partial F_{n}}{\partial h}\right] = \sum_{i,j} \left\{ \left[\frac{\partial}{\partial a_{i}^{n}} \left(\frac{dF_{n}}{dh}\right) - \frac{\partial F_{n}}{\partial a_{i}^{n}}\frac{\tan\psi_{n}}{\Delta t_{n}}\right] \right\}$$

$$\left[\frac{\partial}{\partial a_{j}^{n}} \left(\frac{dF_{n}}{dh}\right) - \frac{\partial F_{n}}{\partial a_{n}^{n}}\frac{\tan\psi_{n}}{\Delta t_{n}}\right] A_{i,j}^{n} + \frac{\partial F_{n+1}}{\partial a_{i}^{n+1}}\frac{\partial F_{n+1}}{\partial a_{i}^{n+1}} \left(\frac{\tan\psi_{n}}{\Delta t_{n}}\right) A_{i,j}^{n+1} \right\}$$

when n = m + 1, then we have instead:

$$E\left[\frac{\partial F_{n}}{\partial h} \frac{\partial F_{n-1}}{\partial h}\right] = \sum_{i,j} \left[\frac{\partial}{\partial a_{i}^{n}} \left(\frac{dF_{n}}{dh}\right) - \frac{\partial F_{n}}{\partial a_{i}^{n}} \frac{\tan \psi_{n}}{\Delta t_{n}}\right]$$

$$\left[\frac{\partial F_{n}}{\partial a_{i}^{n}} \frac{\tan \psi_{n-1}}{\Delta t_{n-1}}\right] A_{i,j}^{n}$$

If n + 1 = m, we get a similar expression with n everywhere replaced by n + 1:

$$E\left[\frac{\partial F_{n+1}}{\partial h} \frac{\partial F_{n}}{\partial h}\right] = \sum_{i,j} \left[\frac{\partial}{\partial a_{i}^{n+1}} \left(\frac{dF_{n+1}}{dh}\right) - \frac{\partial F_{n+1}}{\partial a_{i}^{n+1}} \frac{\tan \psi_{n+1}}{\Delta t_{n+1}}\right]$$

$$\left[\frac{\partial F_{n+1}}{\partial a_{j}^{n+1}} \frac{\tan \psi_{n}}{\Delta t_{n}}\right] A_{i,j}^{n+1}$$

All other expectations are zero.

## Volumetric Strain

The volumetric strain, e  $_{\rm V}$ , depends quadratically on r and linearly on  $(\partial r/\partial h)$ . Accordingly, small changes in these quantities produce the following changes in the volumetric strain:

$$\Delta \epsilon_{\mathbf{v}} = -\left(\frac{\mathbf{r}}{\mathbf{h}}\right)^2 \Delta \left(\frac{\partial \mathbf{r}}{\partial \mathbf{h}}\right) + \left(\frac{2\mathbf{r}}{\mathbf{h}^2}\right) \left(\frac{\partial \mathbf{r}}{\partial \mathbf{h}}\right) \Delta \mathbf{r}$$

Since r represents an integrated quantity, the error in  $\partial r/\partial h$  is expected to dominate the error assignment for e v. In other words, the volumetric strain has the following variance:

$$V[e_{v}] = \left(\frac{\mathbf{r}}{h}\right)^{4} V\left[\frac{\partial \mathbf{r}}{\partial h}\right]$$

The right-side variance was obtained above.

## STRESS DIFFERENCES

The stress difference,  $\Phi$ , has the approximate form:

$$\Phi = \frac{h}{2} \left[ \frac{\partial \mathbf{v}}{\partial \mathbf{t}} + \frac{\partial \mathbf{s}}{\partial \mathbf{h}} \right]$$

The estimation procedures for the two derivatives are statistically independent. Accordingly, the variance in  $\Phi$  has the form:

$$V[\Phi] = \left(\frac{h}{2}\right)^2 \left[V\left[\frac{\partial v}{\partial t}\right] + V\left[\frac{\partial s}{\partial h}\right]\right]$$

Thus, we need the two variances on the right-side expression.

The time derivative is approximated in the usual way:

$$\frac{\partial \mathbf{v}}{\partial \mathbf{t}} = \frac{\mathbf{F}_{n+1} (\mathbf{h}, \mathbf{a}_{i}^{n+1}) - \mathbf{F}(\mathbf{h}, \mathbf{a}_{i}^{n})}{\Delta \mathbf{t}_{n}}$$

where n is selected so that T  $_{\rm n}$  < t < T  $_{\rm n+1}$ . Small changes in the parameter values then lead to the following changes in the time derivative:

$$\Delta \left( \frac{\partial \mathbf{v}}{\partial \mathbf{t}} \right) = \sum_{\mathbf{i}} \left[ \frac{\partial \mathbf{F}_{\mathbf{n}+\mathbf{1}}}{\partial \mathbf{a}_{\mathbf{i}}^{\mathbf{n}}} - \frac{\delta \mathbf{a}_{\mathbf{i}}^{\mathbf{n}+\mathbf{1}}}{\Delta \mathbf{t}_{\mathbf{n}}} - \frac{\partial \mathbf{F}_{\mathbf{n}}}{\partial \mathbf{a}_{\mathbf{i}}^{\mathbf{n}}} - \frac{\delta \mathbf{a}_{\mathbf{i}}^{\mathbf{n}}}{\Delta \mathbf{t}_{\mathbf{n}}} \right]$$

'Thus the variance has the form:

$$V\left[\frac{\partial v}{\partial t}\right] = \sum_{i,j} \left[ \left(\frac{\partial F}{\partial a_{i}^{n+1}} \frac{\partial F}{\partial a_{j}^{n+1}} \right) A_{i,j}^{n+1} \right]$$

$$+ \left( \frac{\partial F_{n}}{\partial a_{i}^{n}} \frac{\partial F}{\partial a_{j}^{n}} \right) A_{i,j}^{n}$$

since  $\delta a_i^{n+1}$  and  $\delta a_i^n$  are statistically independent.

The space derivative is estimated in the usual way as well:

$$\frac{\partial s}{\partial h} = \frac{ds}{dh} - \frac{\partial s}{\partial t} \frac{dt}{dh} = \frac{dG}{dh} - \left[ \frac{G_{n+1} - G_n}{\Delta t_n} \right] \tan \psi_n$$

Small changes in the fitted values then lead to the following change in the space derivative:

$$\Delta \left( \frac{\partial \mathbf{s}}{\partial \mathbf{h}} \right) = \sum_{\mathbf{i}} \left[ \frac{\partial}{\partial \mathbf{b}_{\mathbf{i}}^{\mathbf{n}}} \left( \frac{d\mathbf{G}_{\mathbf{n}}}{d\mathbf{h}} \right) \quad \delta \mathbf{b}_{\mathbf{i}}^{\mathbf{n}} \right]$$
$$- \left( \frac{\partial \mathbf{G}_{\mathbf{n+1}}}{\partial \mathbf{b}_{\mathbf{i}}^{\mathbf{n+1}}} \frac{\partial \mathbf{G}_{\mathbf{n}}}{\partial \mathbf{b}_{\mathbf{i}}^{\mathbf{n}}} - \frac{\partial \mathbf{G}_{\mathbf{n}}}{\partial \mathbf{b}_{\mathbf{i}}^{\mathbf{n}}} \frac{\delta \mathbf{b}_{\mathbf{n}}^{\mathbf{n}}}{\Delta \mathbf{t}_{\mathbf{n}}} \right) \tan \psi_{\mathbf{n}}$$

The variance of  $\partial s/\partial h$  then follows immediately:

$$V\left[\frac{\partial \mathbf{s}}{\partial \mathbf{h}}\right] = \sum_{\mathbf{i},\mathbf{j}} \left\{ \left[ \frac{\partial}{\partial \mathbf{b}_{\mathbf{i}}^{n}} \left( \frac{d\mathbf{G}_{\mathbf{n}}}{d\mathbf{h}} \right) + \frac{\partial \mathbf{G}_{\mathbf{n}}}{\partial \mathbf{b}_{\mathbf{i}}^{n}} \frac{\tan \psi_{\mathbf{n}}}{\Delta t_{\mathbf{n}}} \right] \right.$$

$$\left[ \frac{\partial}{\partial \mathbf{b}_{\mathbf{j}}^{n}} \left( \frac{d\mathbf{G}_{\mathbf{n}}}{d\mathbf{h}} \right) + \frac{\partial \mathbf{G}_{\mathbf{n}}}{\partial \mathbf{b}_{\mathbf{j}}^{n}} \frac{\tan \psi_{\mathbf{n}}}{\Delta t_{\mathbf{n}}} \right] \mathbf{B}_{\mathbf{i},\mathbf{j}}^{n}$$

$$+ \left[ \left( \frac{\partial \mathbf{G}_{\mathbf{n}+1}}{\partial \mathbf{b}_{\mathbf{i}}^{n+1}} \right) \left( \frac{\partial \mathbf{G}_{\mathbf{n}+1}}{\partial \mathbf{b}_{\mathbf{j}}^{n+1}} \right) \left( \frac{\tan \psi_{\mathbf{n}}}{\Delta t_{\mathbf{n}}} \right)^{2} \right] \mathbf{B}_{\mathbf{i},\mathbf{j}}^{n+1} \right\}$$

In practice, the indicated derivatives are evaluated numerically and the sum handled as matrix multiplications.

#### DISTRIBUTION LIST

#### DEPARTMENT OF DEFENSE

Assistant to the Secretary of Defense Atomic Energy ATTN: Executive Assistant

Defense Advanced Rsch. Proj. Agency ATTN: TIO

Defense Civil Preparedness Agency Assistant Director for Research ATTN: Admin. Officer

Defense Documentation Center Cameron Station 12 cy ATTN: DD

Defense Intelligence Agency ATTN: DB-4E ATTN: DB-4C, E. O'Farrell

Defense Nuclear Agency
ATTN: DDST
2 cy ATTN: SPSS
4 cy ATTN: TITL

Field Command
Defense Nuclear Agency
ATTN: FCPR
ATTN: FCTMOF

Interservice Nuclear Weapons School ATTN: TTV

Joint Strat. Tgt. Planning Staff ATTN: NRI-STINFO, Library

Livermore Division, Field Command, DNA Department of Defense Lawrence Livermore Laboratory ATTN: FCPRL

NATO School (SHAPE) ATTN: U.S. Documents Officer

Under Secretary of Defense for Rsch. & Engrg.
Department of Defense
ATTN: Strategic & Space Systems (OS)

WWMCCS System Engineering Organization ATTN: T. Neighbors

# DEPARTMENT OF THE ARMY

BMD Advanced Technology Center Huntsville Office Department of the Army ATTN: 1CRDABH-X ATTN: CRDABH-S

Chief of Engineers Department of the Army ATTN: DAEN-MCE-D ATTN: DAEN-RDM

#### DEPARTMENT OF THE ARMY (Continued)

Deputy Chief of Staff for Ops. & Plans Department of the Army ATTN: MOCA-ADL

Deputy Chief of Staff for Rsch. Dev. & Acq. Department of the Army ATTN: DAMA-AOA-M

Harry Diamond Laboratories Department of the Army ATTN: DELHD-TI ATTN: DELHD-NP

Redstone Scientific Information Ctr. U.S. Army R&D Command ATIN: Chief, Documents

U.S. Army Ballistic Research Labs ATTN: DRXBR-BLE, W. Taylor ATTN: DRXBR-X, J. Meszaros ATTN: DRDAR-BLE, J. Keefer ATTN: Technical Library

U.S. Army Engineer Center ATTN: ATSEN-SY-L

U.S. Army Engineer Div., Huntsville ATTN: HNDED-SR

U.S. Army Engineer Div., Ohio River ATTN: ORDAS-L

U.S. Army Engr. Waterways Exper. Station ATTN: G. Jackson ATTN: W. FVathau ATTN: J. Strange ATTN: L. Ingram ATTN: Library

U.S. Army Material & Mechanics Rsch. Ctr. ATTN: Technical Library

U.S. Army Materiel Dev. & Readiness Cmd. ATTN: DRXAM-TL

U.S. Army Nuclear & Chemical Agency
ATTN: Library

#### DEPARTMENT OF THE NAVY

Civil Engineering Laboratory Naval Construction Battalion Center ATTN: R. Odello ATTN: Code LOBA ATTN: S. Takahashi

Naval Electronic Systems Command ATTN: PME 117-21A

Naval Facilities Engineering Command ATTN: Code 03A ATTN: Code 09M22C ATTN: Code 04B

#### DEPARTMENT OF THE NAVY (Continued)

Naval Material Command ATTN: MAT08T-22

Naval Postgraduate School ATTN: Code 2124

Naval Research Laboratory ATTN: Code 2627

Naval Surface Weapons Center ATTN: Code F31

Naval Surface Weapons Center Dahlgren Laboratory ATTN: Technical Library & Info. Services Br.

Naval Underwater Systems Center ATTN: Code EM, J. Kalinowski

Naval War College ATTN: Code E11

Naval Weapons Evaluation Facility ATTN: Code 10

Office of Naval Research ATTN: Code 461, J. Warner ATTN: Code 715 ATTN: Code 474, N. Perrone

Office of the Chief of Naval Operations ATTN: OP 03EG ATTN: OP 981

Strategic Systems Project Office Department of the Navy ATTN: NSP-43

#### DEPARTMENT OF THE AIR FORCE

Air Force Geophysics Laboratory ATTN: LWW, K. Thompson

Air Force Institute of Technology, Air University ATTN: Library

Air Force Systems Command ATTN: DLCAM

Air Force Weapons Laboratory
ATTN: DE, M. Plamondon
ATTN: SUL
ATTN: DES, J. Thomas
ATTN: DES, J. Shinn

Assistant Chief of Staff Intelligence Department of the Air Force ATTN: INT

Deputy Chief of Staff Research, Development, & Acq. Department of the Air Force ATTN: AFRDQSM

Foreign Technology Division, AFSC ATTN: MICD, Library

## DEPARTMENT OF THE AIR FORCE (Continued)

Deputy Chief of Staff Programs & Resources Department of the Air Force ATTN: PRE

Rome Air Development Center, AFSC ATTN: Documents Library/TSLD

Space & Missile Systems Organization/MN Air Force Systems Command ATTN: MNN ATTN: MNNH, T. Edwards

Strategic Air Command/XPFS
Department of the Air Force
ATTN: NRI-STINFO, Library

#### DEPARTMENT OF ENERGY

Department of Energy Albuquerque Operations Office ATTN: Doc. Con. for Technical Library

Department of Energy Library Room G-042 ATTN: Doc. Con. for Classified Library

Department of Energy Nevada Operations Office ATTN: Doc. Con. for Technical Library

Lawrence Livermore Laboratory
ATTN: Doc. Con. for L-96, L. Woodruff
ATTN: Doc. Con. for Tech. Info. Dept. Library

Los Alamos Scientific Laboratory
ATTN: Doc. Con. for Reports Library
ATTN: Doc. Con. for R. Bridwell

Oak Ridge National Laboratory Union Carbide Corporation-Nuclear Division X-10 Laboratory Records Department ATTN: Civil Defense Res. Proj. ATTN: Doc. Con. for Technical Library

Sandia Laboratories Livermore Laboratory ATTN: Doc. Con. for Library & Sec. Class. Div.

Sandia Laboratories
ATTN: Doc. Con. for A. Chabai
ATTN: Doc. Con. for 3141
ATTN: Doc. Con. for L. Hill

#### OTHER GOVERNMENT AGENCIES

Central Intelligence Agency ATTN: RD/SI, Rm. 5648, Hq. Bldg. for J. Ingley

Department of the Interior Bureau of Mines ATTN:: Technical Library

# DEPARTMENT OF DEFENSE CONTRACTORS

Aerospace Corporation
ATTN: Technical Information Services

## DEPARTMENT OF DEFENSE CONTRACTORS (Continued)

Agbabian Associates ATTN: M. Agbabian

Applied Theory, Inc. 2 cy ATTN: J. Trulio

Avco Research & Systems Group ATTN: Library, A830

The BDM Corporation ATTN: Corporate Library

The Boeing Company ATTN: Aerospace Library

California Research & Technology, Inc. ATTN: S. Shuster ATTN: K. Kreyenhagen ATTN: Library

Calspan Corporation ATTN: Library

Civil/Nuclear Systesm Corporation ATTN: J. Bratton

University of Dayton Industrial Security Super., KL-505 ATTN: H. Swift

University of Denver Colorado Seminary Denver Research Institute ATTN: Sec. Officer for J. Wisotski

EG&G Washington Analytical Services Center, Inc. ATTN: Library

Eric H. Wang Civil Engineering Rsch. Fac. The University of New Mexico ATTN: N. Baum

Gard, Inc. ATTN: G. Neidhardt

General Electric Co.-TEMPO Center for Advanced Studies ATTN: DASIAC

IIT Research Institute ATTN: M. Johnson ATTN: R. Welch ATTN: Documents Library

University of Illinois Consulting Services B106A Civil Engineering Bldg. ATTN: N. Newmark

Institute for Defense Analyses ATTN: Classified Library

Kaman AviDyne Division of Kaman Sciences Corporation
ATTN: E. Criscione
ATTN: N. Hobbs
ATTN: Library

#### DEPARTMENT OF DEFENSE CONTRACTORS (Continued)

Kaman Sciences Corporation ATTN: Library

Lockheed Missiles and Space Co., Inc.

ATTN: T. Geers
ATTN: Technical Information Center D/Coll.

Lovelace Biomedical & Environmental Rsch. Inst., Inc. ATTN: R. Jones

McDonnell Douglas Corporation ATTN: R. Halprin

Merritt CASES, Inc. ATTN: J. Merritt ATTN: Library

Physics International Company ATTN: Technical Library ATTN: E. Moore ATTN: L. Behrmann ATTN: F. Sauer ATTN: J. Thomsen

**R&D** Associates

ATTN: A. Latter ATTN: Technical Information Center

ATTN: J. Lewis
ATTN: W. Wright, Jr.
ATTN: H. Brode
ATTN: J. Carpenter
ATTN: C. MacDonald
ATTN: R. Port

R&D Associates ATTN: H. Cooper

Science Applications, Inc. ATTN: Technical Library

Science Applications, Inc. ATTN: D. Bernstein ATTN: D. Maxwell

Southwest Research Institute ATTN: A. Wenzel ATTN: W. Baker

SRI International ATTN: B. Gasten ATTN: G. Abrahamson

ATTN: D. Keough
ATTN: D. Falconer
ATTN: P. DeCarli
10 cy ATTN: J. Rosenberg

Systems, Science & Software, Inc.

ATTN: D. Grine ATTN: T. Cherry ATTN: T. Riney ATTN: Library

Terra Tek, Inc. ATTN: Library ATTN: A. Abou-Sayed ATTN: S. Green

## DEPARTMENT OF DEFENSE CONTRACTORS (Continued)

Tetra Tech, Inc. ATTN: Library ATTN: L. Hwang

TRW Defense & Space Sys. Group
ATTN: Technical Information Center
ATTN: P. Bhutta
2 cy ATTN: P. Dai

TRW Defense & Space Sys. Group San Bernardino Operations ATTN: E. Wong

# DEPARTMENT OF DEFENSE CONTRACTORS (Continued)

Universal Analytics, Inc. ATTN: E. Field

Weidlinger Assoc., Consulting Engineers ATTN: M. Baron

Weidlinger Assoc., Consulting Engineers ATTN: J. Isenberg

Westinghouse Electric Corporation Marine Division ATTN: W. Volz